NASA CR- 6636

Job 8461

Copy ( ) of ( )

DIFFUSION CONTROLLED COMBUSTION FOR SCRAMJET APPLICATION

Part I

Analysis & Results of Calculations

Technical Report 569

by

R. Edelman

Prepared for

The Marquardt Corporation
16555 Saticoy Street
Van Nuys, California
under NASA Contract No. NAS1-5117

Prepared by

General Applied Science Laboratories, Inc.
Merrick and Stewart Avenues
Westbury, L. I., New York

Approved by: _____
Antonio Ferri
President

PRICES SUBJECT TO CHANGE

Distribution of this report is provided in the interest of information exchange. Responsibility for the contents resides in the author or organization that prepared it.

PRICES SUBJECT TO CHANGE

December 1965

Reproduced by
NATIONAL TECHNICAL
INFORMATION SERVICE
Springfield, Va. 22151

FACILITY FORM 602
N67-25999 (ACCESSION NUMBER)
115 (PAGES)
CR-6636 (NASA CR OR TMX OR AD NUMBER)
(THRU) 0
(CODE) 28
(CATEGORY)

N O T I C E

THIS DOCUMENT HAS BEEN REPRODUCED FROM THE BEST COPY FURNISHED US BY THE SPONSORING AGENCY. ALTHOUGH IT IS RECOGNIZED THAT CERTAIN PORTIONS ARE ILLEGIBLE, IT IS BEING RELEASED IN THE INTEREST OF MAKING AVAILABLE AS MUCH INFORMATION AS POSSIBLE.

ABSTRACT

A desription of the analysis, the method of solution and the results of calculations for diffusion controlled, equilibrium combustion of hydrogen are presented. Calculations include two-dimensional and axisymmetric turbulent flows with constant and variable axial pressure distributions. The investigation was conducted for ramjet combustion chamber inlet conditions associated with the NASA Ramjet Research Engine Project which includes the flight Mach number regime of 3 to 8 and the altitude range from 50,000 to 120,000 feet. The results are presented in terms of flow deflections, combustion lengths and detailed property profiles in the mixing and combustion region. Flow deflections in the vicinity of the fuel injection points from 9° to 30°, and combustion lengths from 15 to 40 fuel jet diameters are indicated. Flow reversal, shockless subsonic burning and pressure interaction due to flow deflection, are predicted and an example of a multiple injection system is presented.

A comparison of the theory with available combustion experiments is presented. The experiments indicate somewhat faster mixing with combustion compared with the corresponding cold flows. In general, excellent agreement of the theory with the experiments is shown.

TABLE OF CONTENTS

Section	Description	Page
	ABSTRACT	ii
	TABLE OF CONTENTS	iii
	LIST OF FIGURES	iv
	LIST OF SYMBOLS	x
I	INTRODUCTION	1
II	ANALYSIS	4
III	CALCULATION PROCEDURE	7
IV	CALCULATIONS AND RESULTS	12
	REFERENCES	20
	FIGURES	23-104

LIST OF TABLES

I	FLIGHT CONDITIONS	22

LIST OF FIGURES

Figure	Description	Page
1	TOTAL IGNITION DELAY - $\omega = 1$	23
2	(a) AXIAL DECAY OF THE HYDROGEN MASS FRACTION (b) LENGTH OF POTENTIAL CORE VERSUS MASS FLUX RATIO	24
3	SCHEMATIC OF FLOW FIELD SHOWING A TYPICAL STREAMLINE IN THE EXTERNAL FLOW	25
4	SCHEMATIC OF THE GRID NETWORK USED IN THE EXPLICIT FINITE DIFFERENCE TECHNIQUE. THE ARROWS INDICATE THE CALCULATION OF THE FLOW FIELD POINT n+1,M FROM DATA AT STATION n.	26
5	FLIGHT CORRIDOR SHOWING THE TRAJECTORY POINTS USED IN THE PRESENT CALCULATIONS	27
6a	MIXING AND COMBUSTION REGION TWO DIMENSIONAL, CONSTANT PRESSURE M_∞=3., M_b=1., ALTITUDE=90,000 FEET	28
6a'	RADIAL PROFILES OF VELOCITY, TEMPERATURE, AND SOUND SPEED AT $\frac{X}{D}$=20. TWO DIMENSIONAL, CONSTANT PRESSURE M_∞=3, M_B=1, ALTITUDE=50,000 FEET	29
6a"	RADIAL PROFILES OF VELOCITY, TEMPERATURE AND SOUND SPEED AT $\frac{X}{D}$=40. TWO DIMENSIONAL, CONSTANT PRESSURE M_∞=3, M_B=1, ALTITUDE = 50,000 FEET	30
6b	MIXING AND COMBUSTION REGION TWO DIMENSIONAL, CONSTANT PRESSURE M_∞=3, M_B=1, ALTITUDE = 65,000 FEET	31
6b'	RADIAL PROFILES OF VELOCITY, TEMPERATURE AND SOUND SPEED AT $\frac{X}{D}$=20. TWO DIMENSIONAL, CONSTANT PRESSURE M_∞=3, M_B=1, ALTITUDE = 65,000 FEET	32
6c	MIXING AND COMBUSTION REGION TWO DIMENSIONAL, CONSTANT PRESSURE M_∞=3, M_b=1, ALTITUDE = 85,000 FEET	33
6c'	RADIAL PROFILES OF VELOCITY, TEMPERATURE, AND SOUND SPEED AT X/D=20. TWO DIMENSIONAL, CONSTANT PRESSURE M_∞=3, M_B=1, ALTITUDE = 85,000 FEET	34
6c"	RADIAL PROFILES OF VELOCITY, TEMPERATURE, AND SOUND SPEED AT X/D=40. TWO DIMENSIONAL, CONSTANT PRESSURE M_∞=3, M_B=1, ALTITUDE = 85,000 FEET	35

Figure	Description	Page
6d	MIXING AND COMBUSTION REGION TWO DIMENSIONAL, CONSTANT PRESSURE M_∞=6, M_b=2, ALTITUDE = 75,000 FEET	36
6d'	RADIAL PROFILES OF VELOCITY, TEMPERATURE AND SOUND SPEED AT X/D=20. TWO DIMENSIONAL, CONSTANT PRESSURE M_∞=6, M_b=2, ALTITUDE = 75,000 FEET	37
6d"	RADIAL PROFILES OF VELOCITY, TEMPERATURE AND SOUND SPEED AT X/D=40. TWO DIMENSIONAL, CONSTANT PRESSURE M_∞=6, M_b=2, ALTITUDE = 75,000 FEET	38
6e	MIXING AND COMBUSTION REGION TWO DIMENSIONAL, CONSTANT PRESSURE M_∞=6, M_b=2, ALTITUDE = 90,000 FEET	39
6e'	RADIAL PROFILES OF VELOCITY, TEMPERATURE AND SOUND SPEED AT X/D=20. TWO DIMENSIONAL, CONSTANT PRESSURE M_∞=6, M_B=2, ALTITUDE = 90,000 FEET	40
6e"	RADIAL PROFILES OF VELOCITY, TEMPERATURE AND SOUND SPEED AT X/D=40. TWO DIMENSIONAL, CONSTANT PRESSURE M_∞=6, M_B=2, ALTITUDE = 90,000 FEET	41
6f	MIXING AND COMBUSTION REGION TWO DIMENSIONAL, CONSTANT PRESSURE M_∞=6, M_B=2, ALTITUDE = 110,000 FEET	42
6f'	RADIAL PROFILES OF VELOCITY, TEMPERATURE, AND SOUND SPEED AT X/D=20 TWO DIMENSIONAL, CONSTANT PRESSURE M_∞=6, M_B=2, ALTITUDE = 110,000 FEET	43
6f"	RADIAL PROFILES OF VELOCITY, TEMPERATURE AND SOUND SPEED AT X/D=40 TWO DIMENSIONAL, CONSTANT PRESSURE M_∞=6, M_B=2, ALTITUDE = 110,000 FEET	44
6g	MIXING AND COMBUSTION REGION TWO DIMENSIONAL, CONSTANT PRESSURE M_∞=8, M_B=3.26 ALTITUDE = 25,000 FEET	45
6g'	RADIAL PROFILES OF VELOCITY, TEMPERATURE AND SOUND SPEED AT X/D=20 TWO DIMENSIONAL, CONSTANT PRESSURE M_∞=8, M_B=3.26, ALTITUDE = 85,000 FEET	46
6g"	RADIAL PROFILES OF VELOCITY, TEMPERATURE AND SOUND SPEED AT X/D=40. TWO DIMENSIONAL, CONSTANT PRESSURE M_∞=8, M_B=3.26, ALTITUDE = 85,000 FEET	47
6h	MIXING AND COMBUSTION REGION TWO DIMENSIONAL, CONSTANT PRESSURE M_∞=8, M_B=3.26, ALTITUDE = 100,000 FEET	48

Figure	Description	Page
6h'	RADIAL PROFILES OF VELOCITY, TEMPERATURE, AND SOUND SPEED AT X/D=20. TWO DIMENSIONAL, CONSTANT PRESSURE M_∞=8, M_B=3.26, ALTITUDE = 100,000 FEET	49
6h"	RADIAL PROFILES OF VELOCITY, TEMPERATURE, AND SOUND SPEED AT X/D=40. TWO DIMENSIONAL, CONSTANT PRESSURE M_∞=8, M_B=3.26, ALTITUDE = 100,000 FEET	50
6i	MIXING AND COMBUSTION REGION TWO DIMENSIONAL, CONSTANT PRESSURE M_∞=8, M_B=3.26, ALTITUDE 120,000 FEET	51
6i'	RADIAL PROFILES OF VELOCITY, TEMPERATURE AND SOUND SPEED AT X/D=20. TWO DIMENSIONAL, CONSTANT PRESSURE M_∞=8, M_B=3.26, ALTITUDE = 120,000	52
6i"	RADIAL PROFILES OF VELOCITY, TEMPERATURE AND SOUND SPEED AT X/D=40. TWO DIMENSIONAL, CONSTANT PRESSURE M_∞=8, M_B=3.26, ALTITUDE = 120,000 FEET	53
7	FLOW DEFLECTION ANGLE FOR TWO DIMENSIONAL, CONSTANT PRESSURE MIXING AND COMBUSTION	54
8	THERMAL COMPRESSION IN TWO DIMENSIONAL DIFFUSION CONTROLLED COMBUSTION FOR AN ALTITUDE OF 85,000 FEET	55
9a	MIXING AND COMBUSTION REGION TWO DIMENSIONAL, PRESSURE DROP, P/Pb=1-0.0125 X/D M_∞=6, M_B=2, ALTITUDE=90,000 FEET	56
9a'	RADIAL PROFILE OF VELOCITY, TEMPERATURE, AND SOUND SPEED AT X/D=20. TWO DIMENSIONAL, PRESSURE DROP M_∞=6, M_B=2, ALTITUDE = 90,000 FEET	57
9a"	RADIAL PROFILES OF VELOCITY, TEMPERATURE AND SOUND SPEED AT X/D=40. TWO DIMENSIONAL, PRESSURE DROP M_∞=6, M_B=2, ALTITUDE = 90,000 FEET	58
10a	MIXING AND COMBUSTION REGION TWO DIMENSIONAL, PRESSURE RISE P/Pb=1+0.1 X/D M_∞=6, M_B=2, ALTITUDE = 90,000 FEET	59
10a'	RADIAL PROFILES OF VELOCITY, TEMPERATURE, AND SOUND SPEED AT X/D=7 TWO DIMENSIONAL, PRESSURE RISE M_∞=6, M_B=2, ALTITUDE = 90,000 FEET	60
10a"	RADIAL PROFILES OF VELOCITY, TEMPERATURE, AND SOUND SPEED AT X/D=15 TWO DIMENSIONAL, PRESSURE RISE M_∞=6 M_B=2, ALTITUDE = 90,000 FEET	61

Figure	Description	Page
11a	MIXING AND COMBUSTION REGION AXISYMMETRIC, CONSTANT PRESSURE M_∞=3, M_B=1, ALTITUDE = 50,000 FEET	62
11a'	RADIAL PROFILES OF VELOCITY, TEMPERATURE AND SOUND SPEED AT X/D=20. AXISYMMETRIC, CONSTANT PRESSURE M_∞=3, M_B=1, ALTITUDE = 50,000 FEET	63
11a"	RADIAL PROFILES OF VELOCITY, TEMPERATURE, AND SOUND SPEED AT X/D=40. AXISYMMETRIC, CONSTANT PRESSURE M_∞=3, M_B=1, ALTITUDE = 50,000 FEET	64
11b	MIXING AND COMBUSTION REGION AXISYMMETRIC, CONSTANT PRESSURE M_∞=3, M_B=1, ALTITUDE = 65,000 FEET	65
11b'	RADIAL PROFILES OF VELOCITY, TEMPERATURE, AND SOUND SPEED AT X/D=20. AXISYMMETRIC, CONSTANT PRESSURE M_∞=3, M_B=1, ALTITUDE = 65,000 FEET	66
11b"	RADIAL PROFILES OF VELOCITY, TEMPERATURE AND SOUND SPEED AT X/D=40. AXISYMMETRIC, CONSTANT PRESSURE M_∞=3, M_B=1, ALTITUDE = 65,000 FEET	67
11c	MIXING AND COMBUSTION REGION AXISYMMETRIC, CONSTANT PRESSURE M_∞=3, M_B=1, ALTITUDE = 85,000 FEET	68
11c'	RADIAL PROFILES OF VELOCITY, TEMPERATURE AND SOUND SPEED AT X/D=10. AXISYMMETRIC, CONSTANT PRESSURE M_∞=3, M_B=1, ALTITUDE = 85,000 FEET	69
11c"	RADIAL PROFILES OF VELOCITY, TEMPERATURE AND SOUND SPEED AT X/D=20. AXISYMMETRIC, CONSTANT PRESSURE M_∞=3, M_B=1, ALTITUDE = 85,000 FEET	70
11d	MIXING AND COMBUSTION REGION AXISYMMETRIC, CONSTANT PRESSURE M_∞=6, M_B=2, ALTITUDE = 75,000 FEET	71
11d'	RADIAL PROFILES OF VELOCITY TEMPERATURE AND SOUND SPEED AT X/D=20. AXISYMMETRIC, CONSTANT PRESSURE M_∞=6, M_B=2, ALTITUDE = 75,000 FEET	72
11d"	RADIAL PROFILES OF VELOCITY, TEMPERATURE AND SOUND SPEED AT X/D = 10. AXISYMMETRIC, CONSTANT PRESSURE M_∞=6, M_B=2, ALTITUDE = 75,000 FEET	73
11e	MIXING AND COMBUSTION REGION AXISYMMETRIC, CONSTANT PRESSURE M_∞=6, M_B=2, ALTITUDE = 90,000 FEET	74

Figure	Description	Page
11e'	RADIAL PROFILES OF VELOCITY, TEMPERATURE AND SOUND SPEED AT X/D=10. AXISYMMETRIC, CONSTANT PRESSURE M_∞=6, M_B=2, ALTITUDE = 90,000 FEET	75
11e"	RADIAL PROFILES OF VELOCITY, TEMPERATURE AND SOUND SPEED AT X/D = 20. AXISYMMETRIC, CONSTANT PRESSURE M_∞=6, M_B=2, ALTITUDE = 90,000 FEET	76
11f	MIXING AND COMBUSTION REGION AXISYMMETRIC, CONSTANT PRESSURE M_∞=6, M_B=2, ALTITUDE = 110,000 FEET	77
11f'	RADIAL PROFILES OF VELOCITY, TEMPERATURE AND SOUND SPEED AT X/D=10. AXISYMMETRIC, CONSTANT PRESSURE M_∞=6, M_B=2, ALTITUDE = 110,000 FEET	78
11f"	RADIAL PROFILES OF VELOCITY, TEMPERATURE AND SOUND SPEED AT X/D=20. AXISYMMETRIC, CONSTANT PRESSURE M_∞=6, M_B=2, ALTITUDE = 110,000 FEET	79
11g	MIXING AND COMBUSTION REGION AXISYMMETRIC, CONSTANT PRESSURE M_∞=8, M_B=3.26, ALTITUDE = 85,000 FEET	80
11g'	RADIAL PROFILES OF VELOCITY, TEMPERATURE AND SOUND SPEED AT X/D=10. AXISYMMETRIC, CONSTANT PRESSURE M_∞=8, M_B=3.26, ALTITUDE = 85,000 FEET	81
11g"	RADIAL PROFILES OF VELOCITY, TEMPERATURE AND SOUND SPEED AT X/D=20 AXISYMMETRIC, CONSTANT PRESSURE M_∞=8, M_B=3.26, ALTITUDE = 85,000 FEET	82
11h	MIXING AND COMBUSTION REGION AXISYMMETRIC, CONSTANT PRESSURE M_∞=8, M_B=3.26, ALTITUDE = 100,000 FEET	83
11h'	RADIAL PROFILES OF VELOCITY, TEMPERATURE AND SOUND SPEED AT X/D=10. AXISYMMETRIC, CONSTANT PRESSURE M_∞=8, M_B=3.26, ALTITUDE = 100,000 FEET	84
11h"	RADIAL PROFILES OF VELOCITY, TEMPERATURE AND SOUND SPEED AT X/D=20. AXISYMMETRIC, CONSTANT PRESSURE M_∞=8, M_B=2.36, ALTITUDE=100,000 FEET	85
11i	MIXING AND COMBUSTION REGION AXISYMMETRIC, CONSTANT PRESSURE M_∞=8, M_B=3.26, ALTITUDE = 120,000 FEET	86
11i'	RADIAL PROFILES OF VELOCITY, TEMPERATURE, AND SOUND SPEED AT X/D=10. AXISYMMETRIC, CONSTANT PRESSURE M_∞=8, M_B=3.26, ALTITUDE = 120,000 FEET	87

Figure	Description	Page
11i"	RADIAL PROFILES OF VELOCITY, TEMPERATURE, AND SOUND SPEED AT X/D=20. AXISYMMETRIC, CONSTANT PRESSURE M_∞=8, M_B=3.26, ALTITUDE = 120,000 FEET	88
11j	MIXING AND COMBUSTION REGION AXISYMMETRIC, PRESSURE DROP, P/Pb=1-0.0125 X/D M_∞=6, M_B=2, ALTITUDE=90,000 FEET	89
11j'	RADIAL PROFILES OF VELOCITY, TEMPERATURE AND SOUND SPEED AT X/D=10. AXISYMMETRIC, PRESSURE DROP M_∞=6, M_B=2, ALTITUDE = 90,000 FEET	90
11j"	RADIAL PROFILES OF VELOCITY, TEMPERATURE AND SOUND SPEED AT X/D=20. AXISYMMETRIC, PRESSURE DROP M_∞=6, M_B=2, ALTITUDE = 90,000 FEET	91
11k	MIXING AND COMBUSTION REGION AXISYMMETRIC, PRESSURE RISE, P/Pb=1+0.1 X/D M_∞=6, M_B=2, ALTITUDE=90,000 FEET	92
11k'	RADIAL PROFILES OF VELOCITY, TEMPERATURE AND SOUND SPEED AT X/D=10. AXISYMMETRIC, PRESSURE RISE M_∞=6, M_B=2, ALTITUDE = 90,000 FEET	93
11k"	RADIAL PROFILES OF VELOCITY, TEMPERATURE AND SOUND SPEED AT X/D=17.2. AXISYMMETRIC, PRESSURE RISE M_∞=6, M_B=2, ALTITUDE = 90,000 FEET	94
12	NORMALIZED MASS FRACTION OF WATER AT THE CENTERLINE FOR AXISYMMETRIC FLOW AT CONSTANT PRESSURE	95
13	BURNER LENGTH FOR COMPLETE COMBUSTION, AXISYMMETRIC HYDROGEN--AIR SYSTEM, CONSTANT PRESSURE	96
14	MIXING AND COMBUSTION REGION	97
15	MACH NUMBER PROFILES THROUGH COMBUSTOR	98
16	SCHEMATIC OF MULTIPLE INJECTION SYSTEM FOR TWO-DIMENSIONAL CONSTANT PRESSURE COMBUSTION	99
17	AXIAL PROPERTY PROFILES FOR TWO-DIMENSIONAL JET MIXING - TWO SLOTS IN SERIES	100
18	AXIAL MASS FRACTION PROFILES	101
19	AXISYMMETRIC, ZAKKAY EXPERIMENT #1	102
20	AXISYMMETRIC, ZAKKAY EXPERIMENT #2	103
21	ZAKKAY EXPERIMENT #3	104

LIST OF SYMBOLS

A = flow area $(ft)^2$

a = jet radius - ft

b = coefficient in the finite difference formulation defined by Eq. (22)

C_p = constant pressure specific heat BTU/lb-^oK

D = jet diameter - ft.

D_t = turbulent binary diffusion coefficient

H = mixture stagnation enthalpy - BTU/lb-mixture

h = mixture static enthalpy - BTU/lb-mixture

h_i = static enthalpy of the i^{th} species - BTU/lb-species i

k = constant in Eq. (9)

k_t = turbulent thermal conductivity

L = combustion length - ft

$r_{\frac{1}{2}}$ = jet "half-radius" based on the mean velocity-ft

T = temperature - ^oK

u = streamwise component of velocity-fps

v = transverse component of velocity-fps

$\dot{w}_i$ = chemical production of the i^{th} species - slugs/ft^3-sec.

x = streamwise coordinate - ft

y = transverse coordinate - ft

α_i = species mass fraction - lb-species i/lb mixture

$\tilde{\alpha}_j$ = element mass fraction - lb-element j/lb-mixture

μ_t = turbulent viscosity - lb-sec/ft^2

ρ = density - slugs/ft^3

ϕ = equivalence ratio - $\dfrac{\tilde{\alpha}_{H_L}}{\tilde{\alpha}_{O_2} + \tilde{\alpha}_{N_L}} / .029$

Ψ = stream function defined by Eq. (10)

Le = Lewis number - $D_t C_p / k_t$

Pr = Prandtl number - $C_p \mu_t / k_t$

Subscripts

∞ = free stream

e = conditions external to the mixing region

i = i^{th} species, i = O_2, N_2, H_2O, H, O, and OH

j = j^{th} element, j = O_2, N_2, and H_2

(n,M)= generic point in the finite difference grid.

DIFFUSION CONTROLLED COMBUSTION FOR SCRAMJET APPLICATION

Part I - Analysis and Results of Calculations

I. INTRODUCTION

The development of supersonic transports has renewed interest in airbreathing propulsion systems capable of supersonic and hypersonic flight speeds with possible future applications including hypersonic aircraft, ballistic missiles and upper stage launch vehicles.

In the flight Mach number regime from 3 to at least 12 the ramjet system appears attractive since the structural requirements are less critical in comparison to turbojet engines involving rotating parts. Moreover, the attractiveness is enhanced by the apparent feasibility of designing a ramjet with fixed geometry applicable over a wide range of Mach number (c.f. Ref. 1 and 2).

The present work performed for the NASA Ramjet Research Engine Project provides analytical design data for the combustion chamber of the proposed engine. It permits locating the fuel injectors to provide the desired thermal compression. The calculations cover the range of conditions corresponding to the X-15A-2 flight corridor shown in Figure 5, page 27. The corresponding combustion chamber inlet condition are given in Table I, page 22.

A requirement of an engine of this type is that the combustion process be such that it provides the required heat release in a short chamber over a wide range of flight conditions. The combustion process which has been proposed for this application is one which is controlled by mixing, (Ref. 2). A mixing controlled combustion process has several attractive features. The heat release is distributed over a finite length in contrast to a premixed configuration wherein the heat is released abruptly through a detonation

process. The inherent distribution of the heat release in the mixing controlled system provides a mechanism for obtaining a controlled pressure variation enhancing the possibility of a fixed geometry system. Furthermore, the mixing controlled combustion process can take place in supersonic flow eliminating flow losses and critical structural design problems required for subsonic burning.

The basic requirements of the diffusion controlled combustion process are fast reaction kinetics and sufficiently fast mixing to provide combustion lengths that are practical for engine application. Recent investigations of the reaction kinetics of the hydrogen-air system are summarized in Figure 1, which based on the work reported in Ref. 3, 4, 5. The combustion chamber will operate under pressures between 1 and 5 atmospheres with characteristic chamber velocities of the order of 10,000 FPS based on hydrogen injection velocities. For the chamber inlet temperatures shown in Figure 1, the length required to establish equilibrium ranges from 0.1 inch at 5 atm. and 2000^{o}K to about 18 inches at 1 atm. and 1000^{o}K. The latter condition might be typical of combustion chamber inlet conditions at the low end of the flight Mach number spectrum. To reduce the total ignition length an ignition source can be used to increase the effective initial temperature to at least 2000^{o}K. This will reduce the total ignition length to the order of 1 to 2 inches and insure that the process is not dependent on finite rate chemical kinetics.

Turbulent mixing of hydrogen and other gases in air has been extensively investigated over wide ranges of frozen flow conditions in the supersonic and subsonic domains, (Ref. 6,7,8,9,10). The mass of experimental data accumulated during these investigations indicates that the mixing rates are sufficiently fast to make the

diffusion controlled process applicable to supersonic combustion engines. Figures 2a and 2b summarize these data in a correlation of axial concentration decay of the injected gas. For hydrogen-air systems the mass flux ratios generally satisfy the condition $\lambda \leq 1$. Therefore, for a typical 1/8 inch diameter fuel tube the concentration of hydrogen on the axis decays to stoichiometric ($Y_{H_2} \cong 0.03$) in approximately 8 inches. In addition to demonstrating fast mixing rates the correlation of these experimental results has provided a basis for an analytical model for the eddy viscosity and the capability for analyzing new flows, (Ref. 1).

In addition to providing details of the mixing and combustion region, the calculations give the local deflection of the air external to the combustion region. This flow deflection due to combustion is the basis for thermal compression and the computed deflection angles together with the undisturbed burner air Mach numbers are used to give the associated pressure rises. These data are then used as a guide to schedule the location of fuel injectors to obtain the desired compression at various locations in the engine over the entire range of flight conditions.

The combustion chamber inlet conditions are such that dissociation effects are not significant and the heat release may be regarded as concentrated along the surface where stoichiometric conditions exist. Therefore, a combustion efficiency is defined in terms of the length required for the surface of stoichiometric conditions to form a closed surface. For the symmetric flows considered the stoichiometric surface closes on the axis of the jet and at this point essentially all the available hydrogen has reacted to form water. Combustion efficiencies defined in this way are presented, for all flight conditions, as a relation between the combustion length-to-jet radius vs. flight Mach number for each altitude in the trajectory.

II. ANALYSIS

The model of the flow field is shown in Figure 3. The mixing process is assumed to be governed by diffusion normal to the main flow direction and is described by a parabolic system system of the boundary layer type. The describing equations for this process are given by:

Conservation of Mass:

Global

$$\frac{\partial \rho u y^N}{\partial x} + \frac{\partial \rho v y^N}{\partial y} = 0 \tag{1}$$

Species

$$\rho u \frac{\partial \alpha_i}{\partial x} + \rho v \frac{\partial \alpha_i}{\partial y} = \frac{1}{y^N} \frac{\partial}{\partial y} \left[\frac{Le}{Pr} \mu_t y^N \frac{\partial \alpha_i}{\partial y} \right] + \dot{w}_i \tag{2}$$

$i = O_2$, N_2, H_2, O, H, H_2O and OH

Elements

$$\rho u \frac{\partial \tilde{\alpha}_j}{\partial x} + \rho v \frac{\partial \tilde{\alpha}_j}{\partial y} = \frac{1}{y^N} \frac{\partial}{\partial y} \left[\frac{Le}{Pr} \mu_t y^N \frac{\partial \tilde{\alpha}_j}{\partial y} \right] \tag{3}$$

$j = O_2$, N_2, and H_2

Momentum:

$$\rho u \frac{\partial u}{\partial x} + \rho v \frac{\partial u}{\partial y} = \frac{1}{y^N} \frac{\partial}{\partial y} \left[\mu_t y^N \frac{\partial u}{\partial y} \right] - \frac{dp}{dx} \tag{4}$$

Energy:

$$\rho u \frac{\partial H}{\partial x} + \rho v \frac{\partial H}{\partial y} = \frac{1}{y^N} \frac{\partial}{\partial y} \left[\mu y^N \left(\frac{1}{Pr} \frac{\partial H}{\partial y} + \left(\frac{1}{Pr} - \frac{1}{Sc} \right) \sum_i h_i \frac{\partial \alpha_i}{\partial y} \right) \right] \tag{5}$$

where N = 1 for axisymmetric flows
0 for two-dimensional flows

Equation 3 is for the conservation of the elements of the chemical system which are defined according to the relation:

$$\tilde{\alpha}_j = \sum_i \mu_{ij} \frac{w_j}{w_i} \alpha_i \tag{6}$$

where μ_{ij} is the amount of element j in the i^{th} species. The stagnation enthalpy, H, is given by:

$$H = h + \frac{U^2}{2} = \sum_i \alpha_i h_i + \frac{U^2}{2} \tag{7}$$

where he is the mixture static enthalpy and $h_i(T)$ is the static enthalpy of the i^{th} specie.

Chemical System

It was previously shown that at the pressure levels of interest (between 1 and 5 atmospheres) the total length required for equilibrium is small although ignition sources will be required at the low end of the flight Mach number spectrum. The chemical system used here is assumed in equilibrium and is comprised of the seven species, H_2, O_2, N_2, H_2O, O, H and OH with nitrogen considered an inert diluent. The equilibrium computation is based on the data given in the JANAF Tables (Ref. 13) which provide six equations of the form:

$$\alpha_i, \rho, T = \Sigma (\tilde{\alpha}_j, h, p) \tag{8}$$

Equation 8 is the equilibrium equation of state and replaces Eq. 2 for the conservation of species. The indeterminateness of the production term, $\dot{w}_i$, is thereby removed and the flow is completely described by Eq.'s 1, 3, 4, 5, 6, 7, and 8 for the unknowns: u, v, $\tilde{\alpha}_j$, α_i, H, h, ρ and T.

Transport Coefficients

The correlation of data presented in Figure 2 is the basis for a semi-empirical model for the eddy viscosity given by

$$\mu_t = K r_{\frac{1}{2}} (\rho u)_{\ell} \tag{9}$$

where k is taken as a constant, $r_{\frac{1}{2}}$ is the "half-radius" based on the mean velocity in the mixing region, and $(\rho u)_{\ell}$ is the centerline mass flux. This model predicts the $1/x^{\frac{1}{2}}$ decay shown in Figure 2a where k is chosen to fit the data. It is shown in Reference 10 that the Schmidt No. may be taken equal to unity without introducing significant error provided the constant, K, is chosen appropriately to match the experimental data. The value of k used here, in conjunction with unity Lewis and Prandtl No's. (unity Schmidt No.) is .04.

III. CALCULATION PROCEDURE

The solution of the above system of equations provides the details of the flow field including the velocity, temperature, and species fields. Gross characteristics including combustion lengths and flow deflections are also obtained.

The global continuity equation, Eq. 1, can be eliminated from the system of differential equations by introducing the von Mises coordinates as the independent variables. The transformation x, y $\rightarrow$ x, Ψ is defined according to the relations:

$$\rho u y^N = \Psi^N \Psi_y \tag{10a}$$

$$\rho v y^N = \Psi^N \Psi_x \tag{10b}$$

Introduction of 10a and 10b into the differential equations results in:

Element Conservation

$$\frac{\partial \tilde{\alpha}_i}{\partial x} = \frac{1}{\Psi^N} \frac{\partial}{\partial \Psi} \left[\frac{Le_t}{Pr_t} \frac{\mu_t \rho u}{\Psi^N} y^{2N} \frac{\partial \tilde{\alpha}_j}{\partial \Psi} \right] \tag{11}$$

Momentum

$$\frac{\partial u}{\partial x} = \frac{1}{\Psi^N} \frac{\partial}{\partial \Psi} \left[\frac{\mu_t \rho u}{\Psi^N} y^{2N} \frac{\partial u}{\partial \Psi} \right] - \frac{1}{\rho u} \frac{dp}{dx} \tag{12}$$

Energy

$$\frac{\partial H}{\partial x} = \frac{1}{\Psi^N} \frac{\partial}{\partial \Psi} \left[\frac{\mu_t \rho u}{\Psi^N} y^{2N} \frac{1}{Pr} \left\{ \frac{\partial H}{\partial \Psi} + (Pr_t - 1) \frac{\partial U^2/2}{\partial \Psi} + \sum_i h_i (Le_t - 1) \frac{\partial \alpha_i}{\partial \Psi} \right\} \right] \tag{13}$$

The physical y coordinate is obtained by the inverse transformation:

$$y^{N+1} = (N+1) \int_o^{\Psi} \frac{\Psi^N}{\rho u} \, d\Psi \tag{14}$$

and the transverse component of velocity, v, is given by:

$$v = - \frac{\Psi^N \Psi_x}{\rho y^N} \tag{15}$$

Boundary Conditions:

The governing equations are parabolic and require initial conditions at x=o and boundary conditions at $\Psi = \infty$ and $\Psi = 0$. The initial and boundary conditions are:

at x=o ; $o \leq \Psi \leq \Psi_J$

$u=u_J$, $H = H_J$, $(\tilde{\alpha}_j)_J = \alpha_{H_2} = 1$

x=o ; $\Psi \geq \Psi_J$

$u=u_e(o)$, $H = H_e$, $(\tilde{\alpha}_j)_e = \tilde{\alpha}_{o_2}$, $\tilde{\alpha}_{H_2} = 0.232, 0.768$ (16)

at

$x \geq o$; $\Psi \to \infty$

$u = u_e(x)$, $H = H_e$, $(\tilde{\alpha}_j)_e = \tilde{\alpha}_{o_2}$, $\tilde{\alpha}_{H_2} = 0.232, 0.768$

where,

$$\rho_e u_e \frac{du_e}{dx} = - \frac{dp}{dx} \tag{17}$$

and

$$H_e = \text{constant} \tag{18}$$

The conditions expressed by 16, 17 and 18 with symmetry at Ψ=o completes the specification of initial and boundary conditions.

The solution of the governing system has been obtained employing an explicit finite difference technique, (Ref. 14). Figure 4 shows a generic point, (n+1,M), in the x-Ψ grid network. The finite difference formulation for the calculation of the flow at the point (n+1, M) is obtained by using the following explicit difference relations where P is anyone of the three pertinent variables u, $\tilde{\alpha}$; or H:

$$\frac{\partial P}{\partial x} = \frac{P_{n+1,M} - P_{n,M}}{\Delta x} \tag{19}$$

$$\frac{\partial P}{\partial \Psi} = \tfrac{1}{2} \frac{P_{n,M+1} - P_{n,M-1}}{\Delta \Psi} \tag{20}$$

$$\frac{\partial}{\partial \Psi}\left[b \frac{\partial P}{\partial \Psi}\right] = \frac{b_{n,M+\frac{1}{2}}\left[P_{n,M+1} - P_{n,M}\right] - b_{n,M-\frac{1}{2}}\left[P_{n,M-1}\right]}{\Delta \Psi^2} \tag{21}$$

where

$$b = \frac{\rho u y^{2N} \mu_t}{\Psi^N} \tag{22}$$

$$b_{n,M\pm\frac{1}{2}} = \tfrac{1}{2}\left[b_{n,M} + b_{n,M\pm1}\right] \tag{23}$$

and

$$\Psi = M\ (\Delta \Psi) \tag{24}$$

The conservation equations in difference form are:

Elements:

M=0:

$$(\tilde{\alpha}_j)_{n+1,o} = (\tilde{\alpha}_j)_{n,o} + \frac{(1+N)\,2\,\Delta x}{(\Delta \Psi)^2}\left[\frac{(\rho u)^{1-N} Le_t \mu_t}{Pr_t}\right]_{n,o}\left[(\tilde{\alpha}_j)_{n,1} - (\tilde{\alpha}_j)_{n,o}\right] \tag{25a}$$

$M \neq 0$:

$$(\tilde{\alpha}_j)_{n+1,M} = (\tilde{\alpha}_j)_{n,M} + \frac{\Delta X}{M^N (\Delta\Psi)^{2+N}} \left\{ \left(\frac{Le_t b}{Pr}\right)_{n,M+\frac{1}{2}} (\tilde{\alpha}_j)_{n,M+1} - \right.$$

$$- \left[\left(\frac{Le_t b}{Pr_t}\right)_{n,M+\frac{1}{2}} + \left(\frac{Le_t b}{Pr_t}\right)_{n,M-\frac{1}{2}} \right] (\tilde{\alpha}_j)_{n,M} + \qquad (25b)$$

$$\left. + \left(\frac{Le_t b}{Pr_t}\right)_{n,M-\frac{1}{2}} (\tilde{\alpha}_j)_{n,M-1} \right\}$$

$j = O_2,\ N_2,\ H_2$

$$U_{n+1,o} = U_{n,o} + \frac{(1+N)\,2\,\Delta X}{(\Delta\Psi)^2} \left[(\rho u)^{1-N} \mu_t\right]_{n,o} \left[U_{n,1} - U_{n,o}\right] - \qquad (26a)$$

$$- \frac{\Delta X}{(\rho u)_{n,o}} \left(\frac{dP}{dx}\right)_{n+1}$$

$M \neq 0$:

$$U_{n+1,M} = U_{n,M} + \frac{\Delta X}{M^N (\Delta\Psi)^{2+N}} \left\{ (b)_{n,M+\frac{1}{2}} U_{n,M+1} - \right.$$

$$\left. - \left[b_{n,M+\frac{1}{2}} + b_{n,M-\frac{1}{2}}\right] U_{n,M} + b_{n,M-\frac{1}{2}} U_{n,M-1} \right\} -$$

$$- \frac{\Delta X}{(\rho u)_{n,M}} \left(\frac{dP}{dx}\right)_{n+1} \qquad (26b)$$

Energy:

$M = 0$:

$$H_{n+1,o} = H_{n,o} + \frac{(1+N)\,2\Delta X}{(\Delta\Psi)^2} \left[(\rho u)^{1-N} U\right]_{n,o} \left\{ \left(\frac{1}{Pr_t}\right)_{n,o} \left[H_{n,1} - H_{n,o}\right] + \right.$$

$$+ \left(1 - \frac{1}{Pr_t}\right)_{n,o} \frac{1}{2} \left[U^2_{n,1} - U^2_{n,o}\right] +$$

$$\left. + \sum_i \left(h_i \frac{Le_t - 1}{Pr_t}\right)_{n,o} \left[(\alpha_i)_{n,1} - (\alpha_i)_{n,o}\right] \right\} \qquad (27a)$$

M=Ø:

$$H_{n+1,M} = H_{n,M} + \frac{\Delta X}{M^N (\Delta\Psi)^{2+N}} \left\{ \left(\frac{b}{Pr_t}\right)_{n,M+\frac{1}{2}} H_{n,M+1} - \left[\left(\frac{b}{Pr_t}\right)_{n,M+\frac{1}{2}} + \right.\right.$$

$$\left. + \left(\frac{b}{Pr_t}\right)_{n,M-\frac{1}{2}} \right] H_{n,M} + \left(\frac{b}{Pr_t}\right)_{n,M-\frac{1}{2}} H_{n,M-1} + \left(b\left[1-\frac{1}{Pr_t}\right]\right)_{n,M+\frac{1}{2}} \frac{U^2_{n,m+1}}{2} -$$

$$- \left[\left(b\left[1-\frac{1}{Pr_t}\right]\right)_{n,M+\frac{1}{2}} + \left(b\left[1-\frac{1}{Pr_t}\right]\right)_{n,M-\frac{1}{2}} \right] \frac{U^2_{n,M}}{2} + \left(b\left[1-\frac{1}{Pr_t}\right]\right)_{n,M-\frac{1}{2}}$$

$$\frac{U^2_{n,M-1}}{2} + \sum_i \left[bh_i \left(\frac{Le_t - 1}{Pr_t}\right) \right]_{n,M+\frac{1}{2}} (\alpha_i)_{n,M+1} -$$

$$- \sum_i \left[\left(bh_i \frac{Le_t - 1}{Pr_t}\right)_{n,M+\frac{1}{2}} + \left(bh_i \frac{Le_t - 1}{Pr_t}\right)_{n,M-\frac{1}{2}} \right] (\alpha_i)_{n,M} +$$

$$\left. + \sum_i \left[bh_i \frac{Le_t - 1}{Pr_t} \right]_{n,M-\frac{1}{2}} (\alpha_i)_{n,M-1} \right\} \qquad (27b)$$

Step Size Control

The step size in the explicit finite difference scheme is controlled by a stability criterion and from studies of linear parabolic partial differential equations there results the following condition, Ref. 15:

$$\frac{\Delta Y^2}{(1+N)6} \left[\frac{Pr_t}{Le_t \mu_t (\rho u)^{1-N}} \right]_{n,o} \geq \Delta X \leq \frac{1}{3} \frac{M^N (\Delta\Psi)^{2+N}}{\left(\frac{Le_t}{Pr_t} b\right)_{n,M+\frac{1}{2}} + \left(\frac{Le_t}{Pr_t} b\right)_{n,M-\frac{1}{2}}} \qquad (28)$$

Although the partial differential equations are non-linear, the present explicit difference formulation results in a locally linear system and Equation 28 provides an estimate of the stable step size. The computer program has as an input an arbitrary fraction which can be chosen to cut the above step size in the event a stability problem arises.

IV. CALCULATIONS AND RESULTS

Calculations for the characteristics of the diffusion controlled combustion process have been made for the combustion chamber inlet conditions given in Table I. The flight Mach numbers were M_∞ = 3, 6 and 8 and the altitude range was from 50,000 to 120,000 feet. The flight "corridor" is shown in Figure 5 where the circle points represent the flight configurations used in the calculations. In all cases the hydrogen was injected at the stagnation state corresponding to a pressure of 200 psia and a temperature of 2000°R. Furthermore, the hydrogen is injected parallel to the air flow direction with the assumption that it is fully expanded to the local air pressure.

The results of the calculations are presented in Figures 6 through 21. Figure 6a through 6i show the mixing regions for two-dimensional configurations with constant pressure combustion. The streamlines in the flow external to the mixing region are shown and illustrate the local flow deflections due to combustion. Each streamline is characterized by an equivalence ratio, Ø, associated with the total air flow in the particular streamtube. The flow deflection can be characterized by the turning in three regions, i.e. at $\frac{X}{D} = 0$, a near region (at $\frac{X}{D} \sim 4$) and a far region ($\frac{X}{D} \sim 24$). Figure 7 shows the flow deflection in these regions for the entire flight envelope and figure 8 shows the corresponding isentropic compressions in the three regions for the altitude of 85,000 feet. This compression assumes that the deflection due to viscous mixing and combustion is effected to higher order by the pressure rise, which is the foundation of the interaction theory described in Reference 16. The results indicate that substantial thermal compression is obtained particularly in the vicinity of the point of injection. The effect of the total

ignition delay will tend to shift somewhat downstream the indicated pressure rises, but as described earlier the use of ignition sources at the lower flight Mach number will diminish this effect.

The effect of an arbitrary variation in the axial pressure is shown in Figures 9 and 10. Figure 9 shows the results for a combustion chamber with an axial pressure drop at a flight Mach number of 6 and an altitude of 90,000 feet. In comparison with the corresponding constant pressure case, Figure 6e, there is an additional divergence of the streamline due to the acceleration of the flow field. Figure 10 shows the mixing and combustion region for the same flight Mach number and altitude but with an axial pressure rise imposed on the combustion chamber flow field. The entire flow field is compressed and the streamlines are initially flatter in comparison to the constant pressure and pressure drop cases. There are two significant features which arise in conjunction with the pressure rise configuration. The velocity and Mach number develop non-monotonic profiles across the mixing region with the result that a flow reversal occurs at an $\frac{X}{D} \sim 20$. The parabolic equations cannot describe the flow field in the reversed flow region and the calculation fails when the local velocity approaches zero. However, the present analysis predicts the onset of flow reversal and indicates that the region of reversed flow is between the centerline and the edge of the mixing region. This behavior of the Mach number profile is a consequence of the deceleration of the high velocity hydrogen by viscous shear and the high sound speed (low density) due to combustion, both of which combine to reduce the Mach number. The imposed pressure rise has the greatest effect in the low Mach number region and consequently the velocity decreases fastest in this region of the flow until reversal occurs. As the flow field approaches reversal there is a corresponding divergence of the

mixing region. There results a large deflection of the external air flow which could lead to a significant induced pressure rise and shocks. This phenomenon could result in loss in control of the combustion process and indicates a need to avoid large pressure rises in the combustion chamber.

Figures 11a through 11k show the mixing and combustion regions for axisymmetric configurations with the same combustion chamber inlet conditions used in the above two-dimensional calculations. Faster decay of non-uniformities and smaller flow deflections are found in comparison with the two-dimensional results and are a consequence of the transverse curvature effect.

Combustion Efficiency

In the diffusion controlled process the principal combustion and heat release occurs on the surface where stoichiometric concentrations exist. In the region of flow outside of this surface all of the hydrogen has combined to form water except for the effect due to dissociation. This is the basis for the "flame sheet" model discussed by Libby, Ref. 17, where the flow field was analyzed by applying a linearization technique and assuming negligible dissociation. Combustion is complete at the point of closure of the flame sheet. A combustion efficiency can be defined in terms of the ratio of the local concentration of water to the concentration of water resulting from stoichiometric combustion and for the flow discussed here the efficiency is given simply in terms of the axial value of this water concentration ratio. In Fig. 12, a correlation of the combustion efficiency for all flight configurations is given. A value of ξ=6 is representative of complete combustion for all flight conditions where the effect of Mach number and altitude is reflected in the local Reynolds

number defined by $Re(x) = \frac{\rho_j u_j a}{\mu_t}$. Figure 13 shows the physical combustion lengths as a function of the flight Mach number for altitudes ranging for 50,000 to 120,000 feet and indicates that short combustion lengths are possible over the entire flight corridor.

Subsonic Combustion

The combined effects of a rapid deceleration of the hydrogen by the shear forces and the low density due to combustion can result in a local subsonic domain in the mixing region. A comparison of the local sound speed and velocity profiles in Figures 6 through 11 illustrate this characteristic particularly for combustion chamber conditions corresponding to the low flight Mach number range. This phenomena occurs in the constant pressure configurations and indicates the inherent ability of the mixing process to provide a smooth dissipation mechanism for a transition from supersonic to subsonic flow without shocks. The transition can be substantially augmented by applying a small axial pressure rise. Figures 14 and 15 show the results of a calculation to determine the feasibility of obtaining subsonic combustion with a slight pressure rise followed by a zone of subsonic combustion at constant pressure and finally an acceleration to supersonic flow. The configuration is two-dimensional and the combustion chamber inlet conditions correspond approximately to a flight Mach number of 4 at an altitude of 75,000 feet. The air Mach number at the point of hydrogen injection is 1.3. The hydrogen is expanded from a stagnation pressure of 200 psia and a stagnation temperature of 2000°R yielding a jet velocity of 12,250 f.p.s.. Figure 14 shows the mixing and combustion region for the three-stage combustion process in a duct with a global $\phi = 1$. In the

first zone, the mixing combined with a pressure rise results in the Mach number profile shown by the broken line in Fig. 15. The air external to the mixing region has decelerated to a Mach number of one whereas the Mach number in the region of combustion is less than .4. The pressure ratio is 1.5 and the resulting average Mach number across the mixing region is about .72. The second zone proceeds at constant pressure and maintains the average Mach number of .72 although the mixing changes the Mach number distribution as shown by the solid line is Fig. 15. In the third zone the pressure drops to .9 of the chamber inlet pressure and practically the entire flow field is supersonic with an average Mach number of about 1.17. The wall shape required for the pressure distribution is shown in Fig. 14. The calculations are based on a parabolic system of equations which cannot predict the formation of shocks. However, the results indicate that with a mild pressure rise combustion can be made to occur at low subsonic Mach numbers and then the flow can be accelerated to supersonic speeds with a mild pressure drop. The entire process covers a short distance and requires no shocks for its operation.

Multiple Injection

Control of the combustion process requires scheduling of the amount of fuel injected and the location of injection points in the combustion chamber. To establish the characteristics of a flow with multiple injection, two jets in series were considered. A two-dimensional configuration was used and the model of the flow field is shown in Fig. 16. The second jet was located at the point where the temperature due to combustion from the first jet reached its maximum. The air was initially at a temperature of $1000^{o}K$ and a pressure of 1.4 atm. and flowing at a velocity of

6750 f.p.s. The hydrogen was injected from both jets at a velocity at 13,200 f.p.s. and a static temperature of 273°K and the width of the jets was 1/16 inch. The flow field for constant pressure combustion is characterized by the axial property profiles shown in Figures 17 and 18. This curve shows that the first jet mixes rapidly into the pure air and the maximum temperature is attained at about one-tenth of a foot downstream of the point of injection corresponding to an $\frac{X}{D} \sim 40$. The second jet mixes into this region of hot reacting flow and spreads at a slower rate due to the lower density level. The overall length for the calculation was less than 4 inches where the temperature has decreased to about 55 percent of maximum temperature in the first jet, and indicates that the slower mixing rate and the lower oxygen level will require a substantially longer length to reach complete combustion of the total fuel injected. One consequence of this is that for a constant combustion chamber area the primary thermal compression will be derived from the upstream injectors which provide the largest part of the flow deflection.

Experimental Comparison

The inherent difficulty of obtaining measurements in high temperature reacting flows has severely limited the availability of complete diagnostic data on combustion processes. Although complete data including species, velocity, and static temperature fields is lacking, certain of the experiments have provided measurements which permit indirect comparison with the theoretical model. In particular, Zakkay, Ref. 7, measured the stagnation temperature in a series of diffusion controlled combustion experiments involving the hydrogen-air system. The stagnation temperature depends on the species, velocity and static temperature and

consequently agreement of the computed stagnation temperatures with the measured values is an indirect confirmation of the theoretically predicted values of the fundamental properties of the flow. The three experiments reported in Reference 7 were conducted in an axisymmetric configuration with a jet radius of .025 feet. All tests were performed at a discharge pressure of 1 atm. and an air Mach number of approximately 1.55 and the hydrogen was injected subsonically at a stagnation temperature of approximately 1000°K. The air stagnation temperature, the mass flux ratio $\frac{\rho_j \rho_j}{\rho_e u_e}$, and the velocity ratio, u_j/u_e, were the parameters varied for each test. The stagnation temperature was measured along the centerline using two techniques. In the regions of flow at temperature below 2000°K a combination of chromel alumel and platinum platinum-rhodium thermocouples were used, whereas for the higher temperatures a 3/16 inch diameter stainless steel hemisphere cylinder was used as a heat transfer gage using the thin skin technique to obtain the heat flux.

The comparison of the measured stagnation temperatures with the calculated values are shown in Figures 19, 20, and 21. The triangles represent the measured points and the solid lines represent the results of the present theory using a value of k=0.065 in Eq. 9 for the eddy viscosity. Note that this value of k is somewhat larger than the value obtained from frozen flow experiments (k=.04). In Figures 19 and 20 the calculated rise in stagnation temperature is somewhat more gradual then the measured rise and is apparently due to the assumption of equilibrium. The visual observations of the flame corresponding to Fig. 19 indicated that combustion initiated on the axis and apparently at the point where stoichiometric conditons prevailed, Ref. 7.

The result is a rapid rise to equilibrium. The comparison presented in Fig. 20 indicates the same behavior for this case which is apparently a non-equilibrium effect. The results presented in Figure 21 are based on conditions which were chosen to minimize non-equilibrium effects and the air stagnation temperature was increased to approximately 1460^{o}K. The comparison with the theory for this case is excellent.

In general, the calculations for the three cases using an adjusted value of k show remarkable agreement with the experiments. This indicates that the assumptions, including the representation for the eddy viscosity, are reasonable and can be applied to combusting flows.

REFERENCES

1. Ferri, A., Review Problems in Application of Supersonic Combustion. Seventh Lanchester Memorial Lecture, May 14, 1964; also Journal R.A.S. 68, No. 645, September 1964.
2. Ferri, A., Possible Directions of Future Research in Air-Breathing Engines. AGARD Combustion and Propulsion Colloquium, pp 3-15, Pergamon Press Ltd., 1960.
3. Nicholls, J.A., Stabilization of Gaseous Detonation Waves with Emphasis on the Ignition Delay Zone. Thesis for Ph.D., University of Michigan, 1960. Available from University Microfilms, Inc., Ann Arbor, Michigan.
4. Momtchiloff, I.N., Taback, E.D. and Buswell, R.F. An Analytical Method of Computing Reaction Rates for Hydrogen-Air Mixtures. Paper presented at the Ninth International Meeting of the Combustion Institute, Cornell University, August 1962.
5. Pergament, H.S., A Theoretical Analysis of Non-Equilibrium Hydrogen-Air Reactions in Flow Systems. Paper No. 63-113, AIAA-ASME Hypersonic Ramjet Conference, 23rd-25th April 1963.
6. Ferri, A., Libby, P.A. and Zakkay, V. Theoretical and Experimental Investigation of Supersonic Combustion. Aeronautical Research Laboratories, ARL 62-467, September 1962; also Paper presented at Third ICAS Congress, Stockholm, Sweden, 27th-31st August 1962; also PIBAL Report No. 713, ARL 62-467, AD 291712, September 1962.
7. Zakkay, V. and Krause, E. Mixing Problems with Chemical Reactions. PIBAL Report No. 776, March 1963.
8. Ferri, A. Axially Symmetric Heterogeneous Mixing. Paper presented at the IUTAM International Symposium on Applications of the Theory of Functions in Continuum Mechanics, Thilisi, Russia, 18th-24th September 1963; also PIBAL Report No. 787, AFOSR 5326, Sept. 1963.

9. Alpinieri, L.J. An Experimental Investigation of the Turbulent Mixing of Non-Homogeneous Coaxial Jets. PIBAL Report No. 789, August 1963.

10. Zakkay, V., Krause, E. and Woo, S.D.L. Turbulent Transport Properties for Axisymmetric Heterogeneous Mixing. AIAA Conference, Paper presented at 20th-22nd January 1964 Meeting; also PIBAL Report No. 813, March 1964.

11. Kleinstein, G. An Approximate Solution for the Axisymmetric Jet of a Laminar Compressible Fluid. Quart.Appl.Math., Vol. 20, 1, pp. 49-54, April 1962.

12. Kleinstein, G. On the Mixing of Laminar and Turbulent Axially-Symmetric Compressible Flows. PIBAL Report No. 756, February 1963.

13. Thermal Laboratory, Dow Chemical Co., JANAF Interim Thermochemical Tables, December 1960, ET SEQ.

14. Zeiberg, S. and Bleich, G.D. Finite Difference Calculation of Hypersonic Wakes. Paper presented at AIAA Conference on Physics of Entry into Planetary Atmospheres, MIT, 26th-28th August 1963, Preprint 63-449; also GASL Technical Report 338, February 1963.

15. Richtmyer, R.D. Difference Methods for Initial Valve Problems, Interscience Publishers, N.Y., 57.

16. Hayes, W.D., and Probstein, R.F. Hypersonic Flow Theory. Academic Press, New York, 1959, pp. 333-353.

17. Libby, P.A. Theoretical Analysis of Turbulent Mixing of Reactive Gases with Application to Supersonic Combustion of Hydrogen. ARS Journal, Vol. 32, pp. 388-396, March 1962.

TABLE I - FLIGHT CONDITIONS

Fuel Stagnation State
P_j^o = 200 psia
T_j^o = 2000°R

b = air at burner inlet
j = hydrogen at jet exit plane

M_∞	Altitude - ft	T_∞ - °K	P_∞ - #/ft^2	M_b	P_b - #/ft^2	T_b - °K	U_b - FPS	M_j	T_j - °K	U_j - FPS	a - ft
3	50,000	217.	244.	1.	3773.	506.	1478.	1.98	623.	12369.	.025
3	65,000	217.	119.	1.	1843.	506.	1478.	2.44	507.	13754.	.025
3	85,000	222.	46.	1.	716.	517.	1495.	3.06	387.	15067.	.025
6	75,000	219.	74.	2.	9980.	997.	4152.	1.33	821.	9539.	.025
6	90,000	224.	37.	2.	4982.	1020.	4200.	1.8	674.	11696.	.025
6	110,000	232.	15.	2.	2002.	1057.	4274.	2.38	521.	13597.	.025
8	85,000	222.	46.	3.26	4925.	984.	6722.	1.81	671.	11736.	.025
8	100,000	227.	23.	3.26	2477.	1006.	6797.	2.25	552.	13232.	.025
8	120,000	241.	9.6	3.26	1022.	1070.	7000.	2.86	421.	14689.	.025

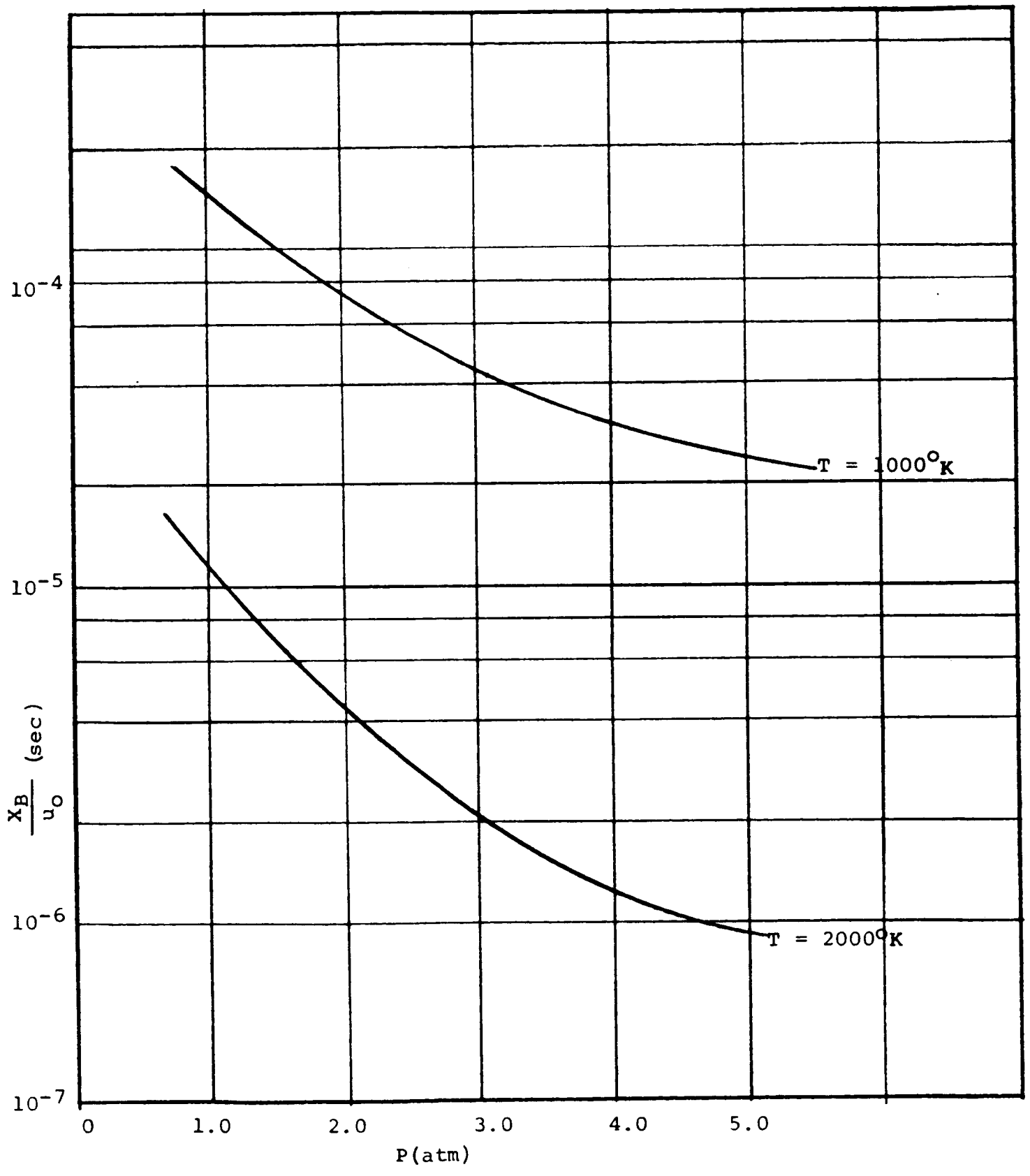

FIGURE 1 - TOTAL IGNITION DELAY - $\omega = 1$

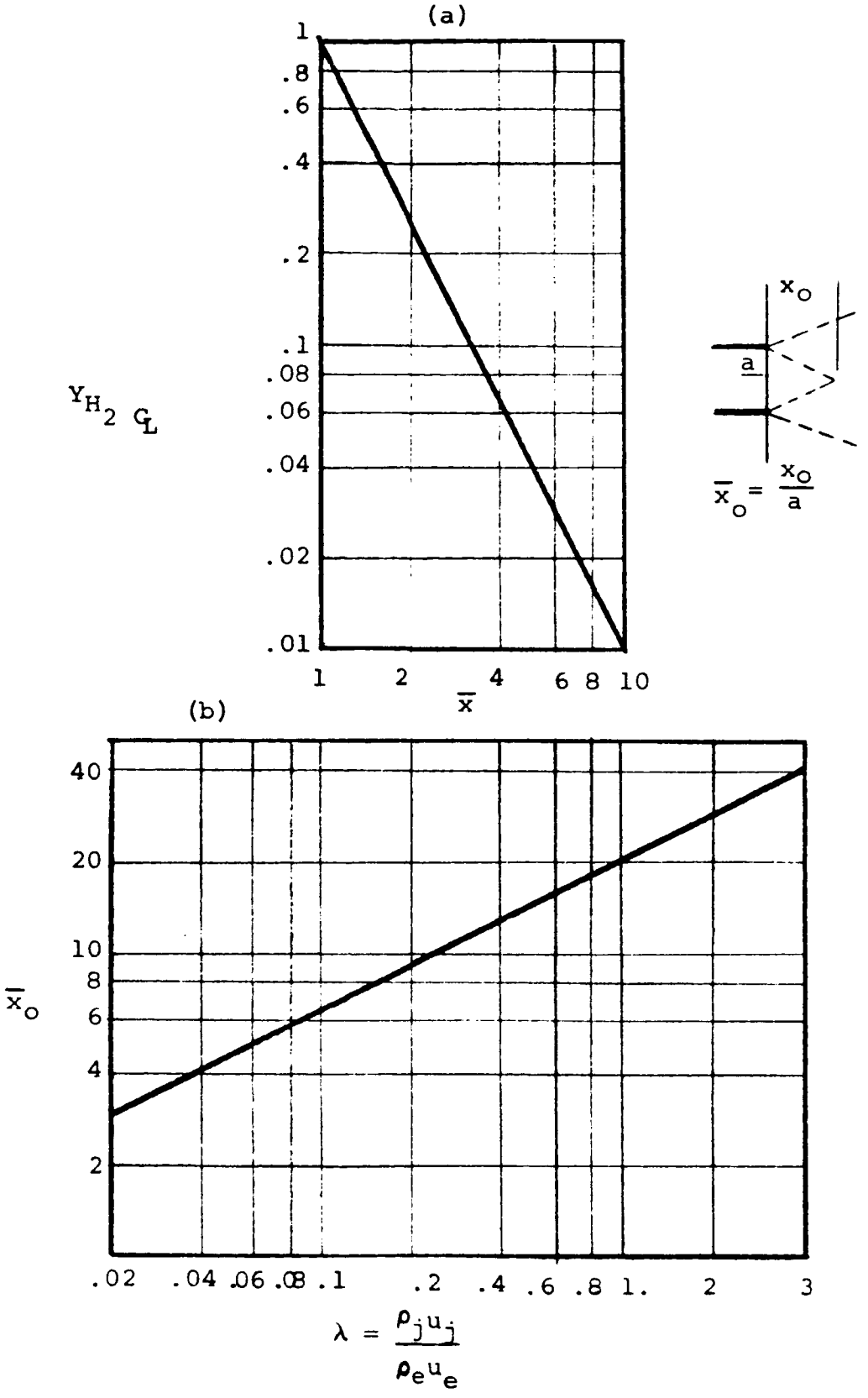

FIGURE 2 (a) Axial Decay of the Hydrogen Mass Fraction

(b) Length of Potential Core versus Mass Flux Ratio

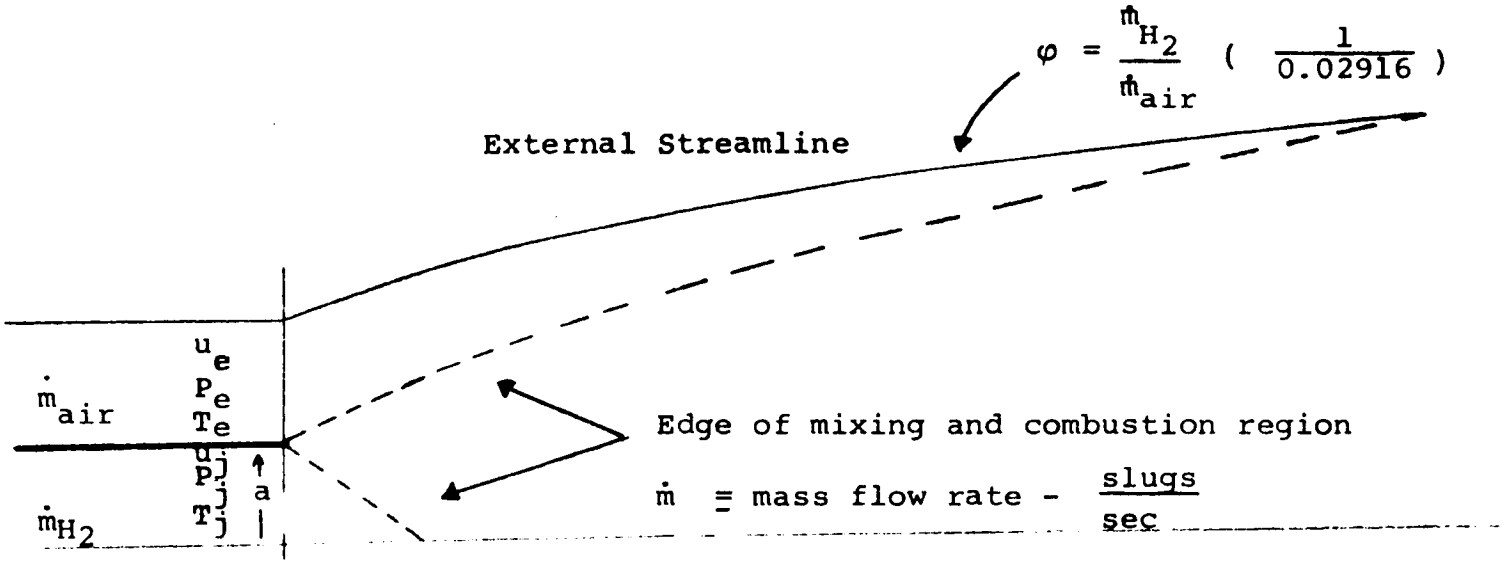

FIGURE 3 - SCHEMATIC OF FLOW FIELD SHOWING A TYPICAL STREAMLINE IN THE EXTERNAL FLOW

TP 5769
Page 25

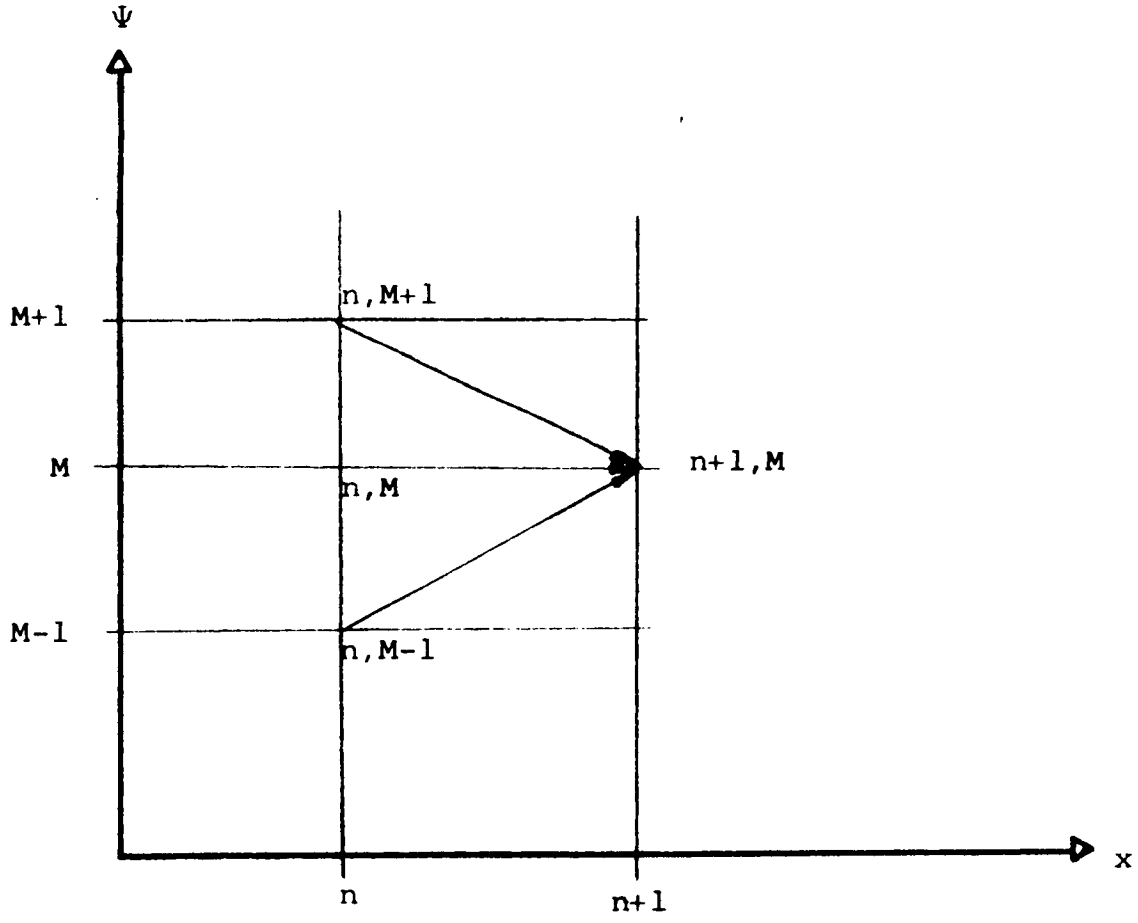

FIGURE 4 - SCHEMATIC OF THE GRID NETWORK USED IN THE EXPLICIT FINITE DIFFERENCE TECHNIQUE. THE ARROWS INDICATE THE CALCULATION OF THE FLOW FIELD POINT n+1,M FROM DATA AT STATION n.

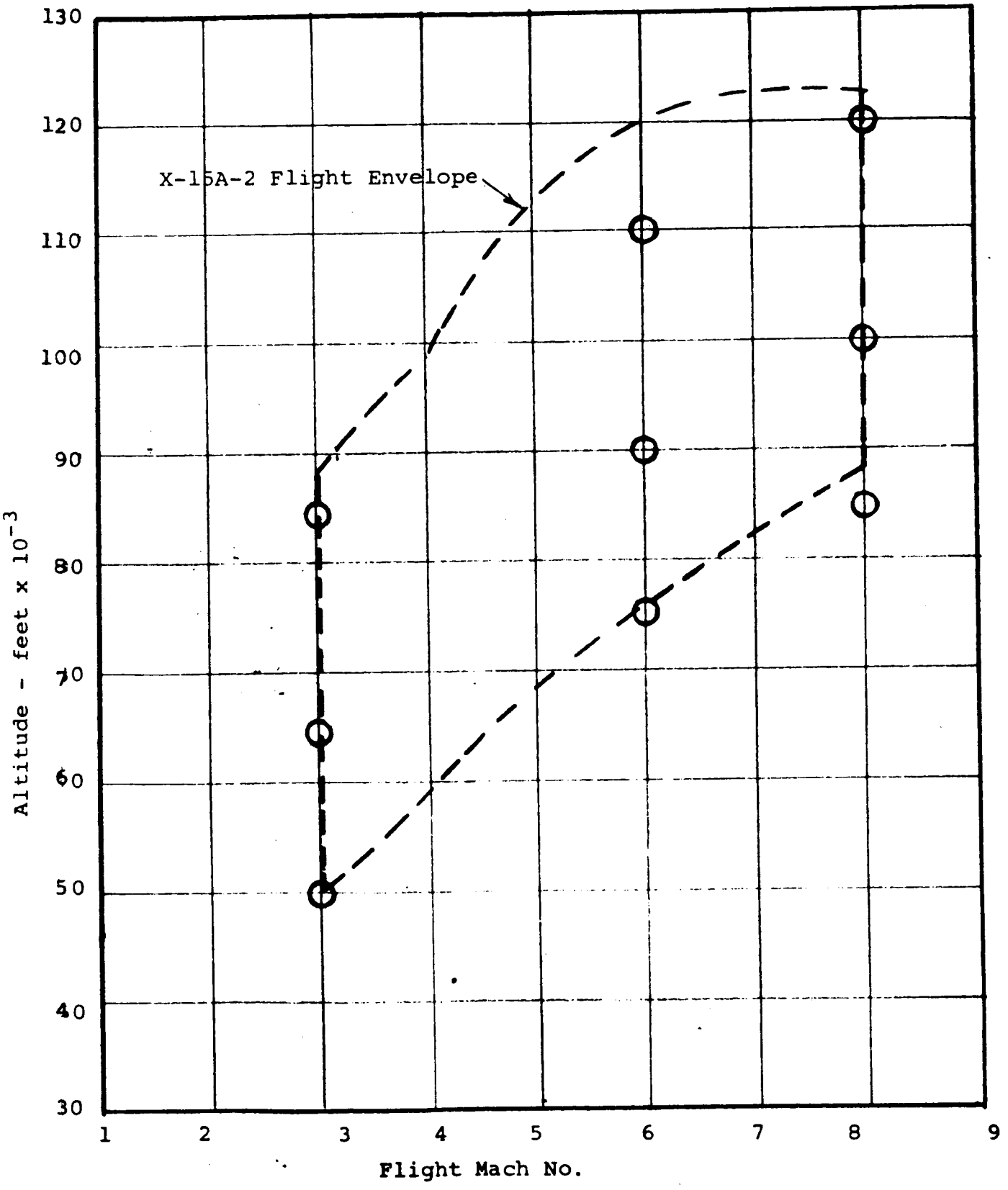

FIGURE 5 - FLIGHT CORRIDOR SHOWING THE TRAJECTORY POINTS USED IN THE PRESENT CALCULATIONS

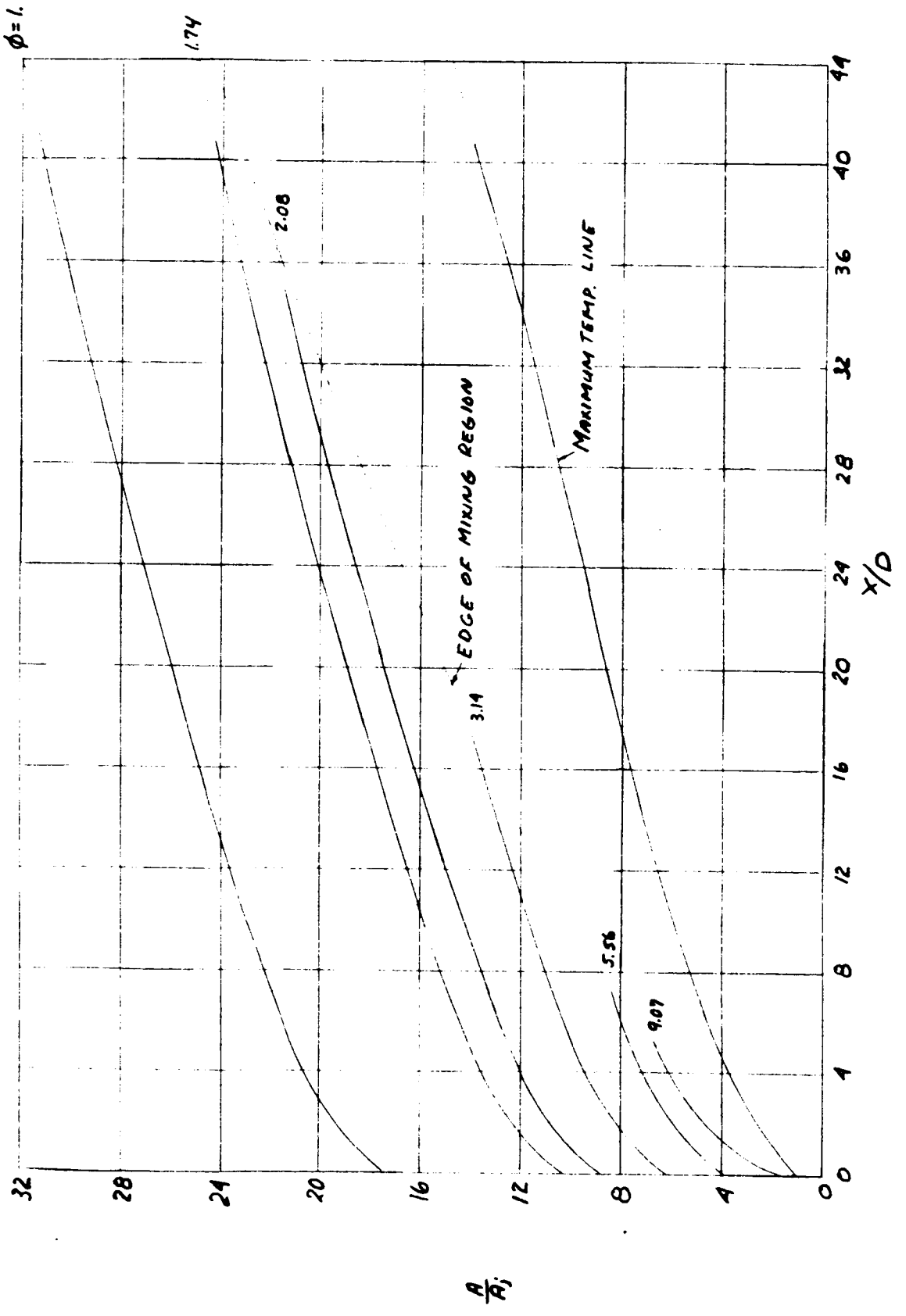

Fig 6a Mixing and Combustion Region
Two Dimensional, Constant Pressure
$M_\infty = 3.$, $M_b = 1.$, Altitude = 80,000 feet

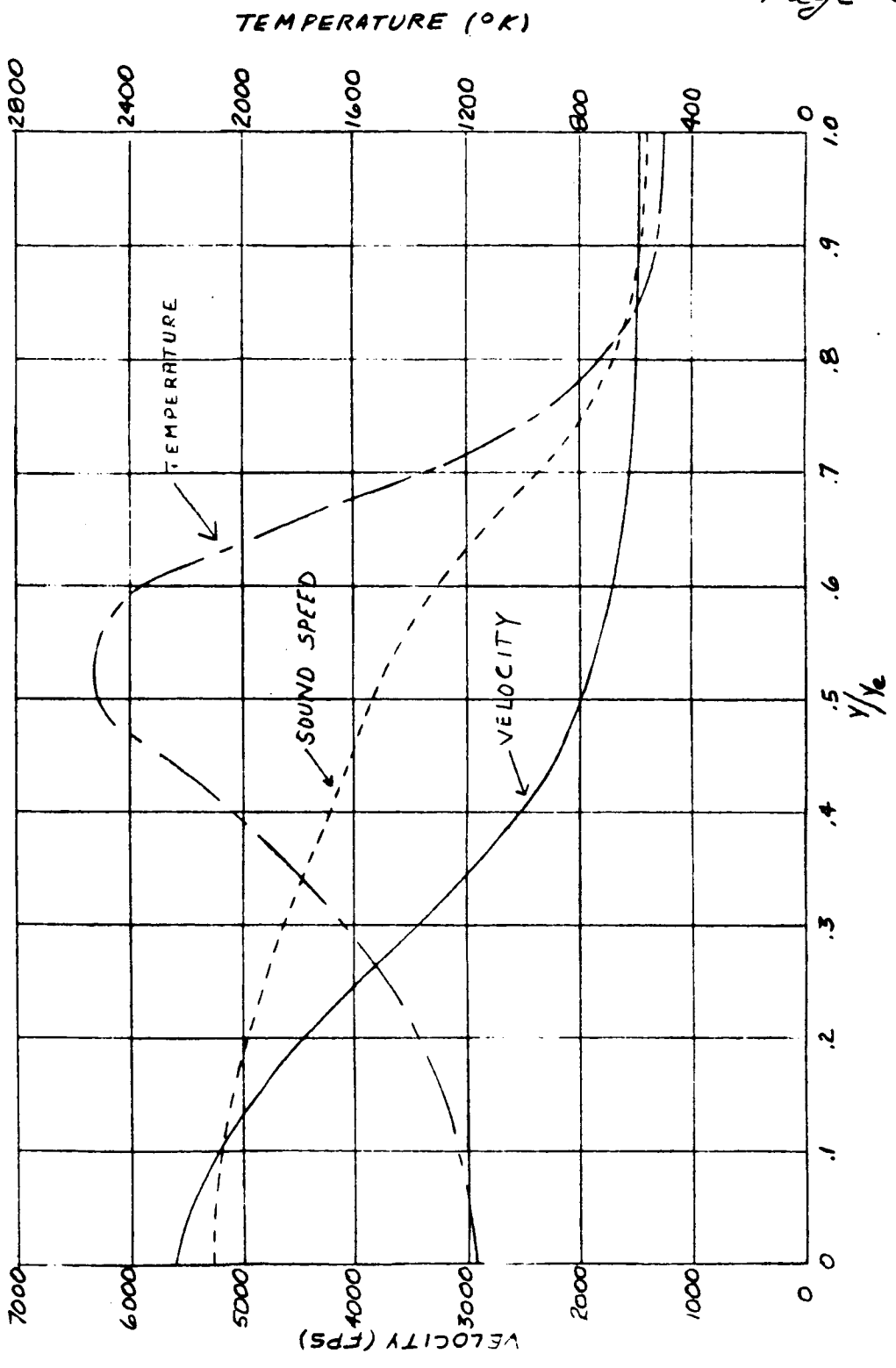

FIG. 6a' RADIAL PROFILES OF VELOCITY, TEMPERATURE, AND SOUND SPEED AT $\frac{x}{D} = 20$.
TWO DIMENSIONAL, CONSTANT PRESSURE
$M_\infty = 3$, $M_\delta = 1$, ALTITUDE = 50,000 FEET

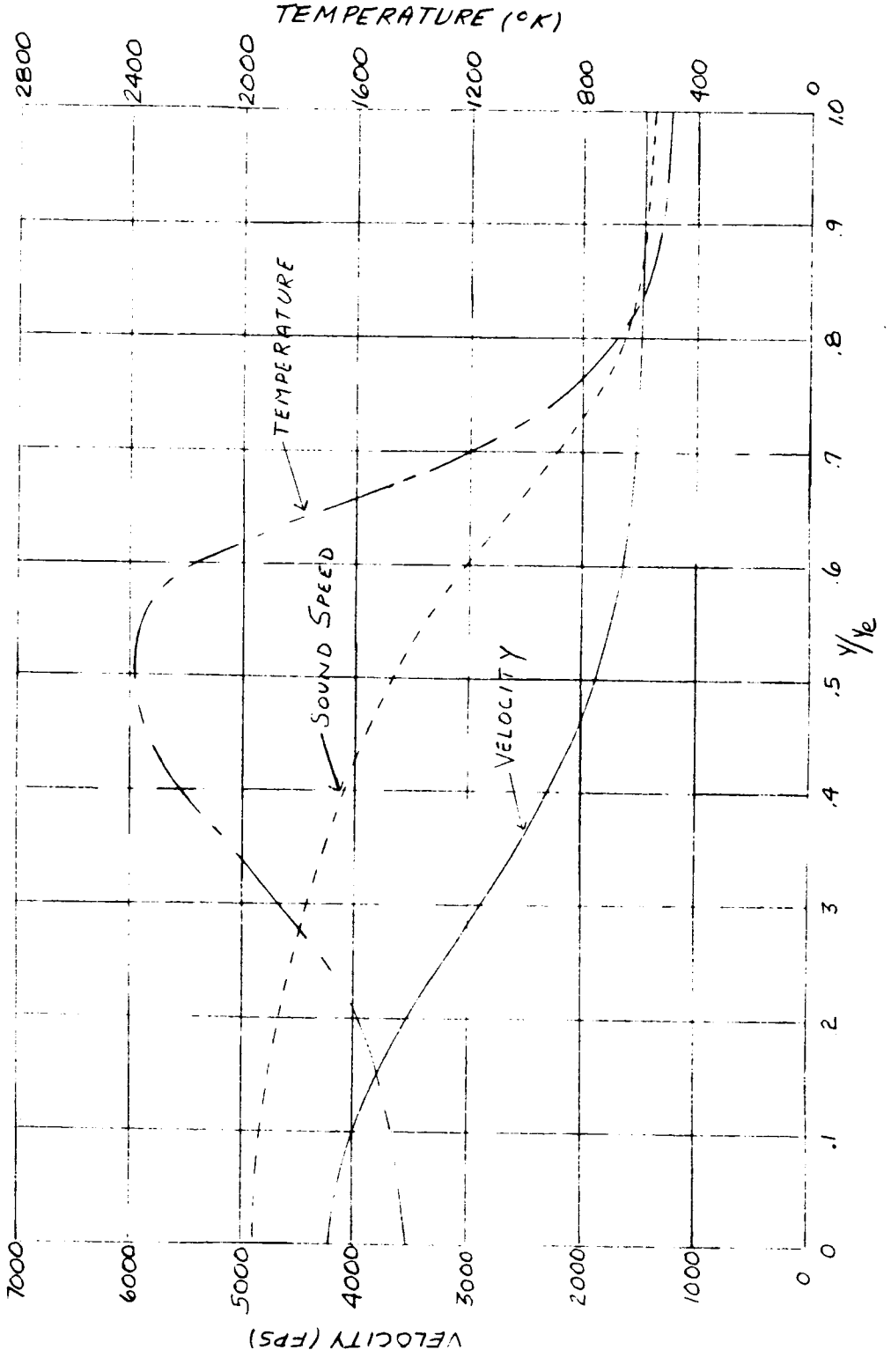

FIG. 6a" RADIAL PROFILES OF VELOCITY, TEMPERATURE AND SOUND SPEED AT $\frac{X}{D} = 40$
TWO DIMENSIONAL, CONSTANT PRESSURE
$M_\infty = 3$, $M_B = 1$, ALTITUDE = 50,000 FEET

FIG. 6b MIXING AND COMBUSTION REGION
TWO DIMENSIONAL, CONSTANT PRESSURE
$M_\infty = 3$, $M_B = 1$, ALTITUDE = 65,000 FEET

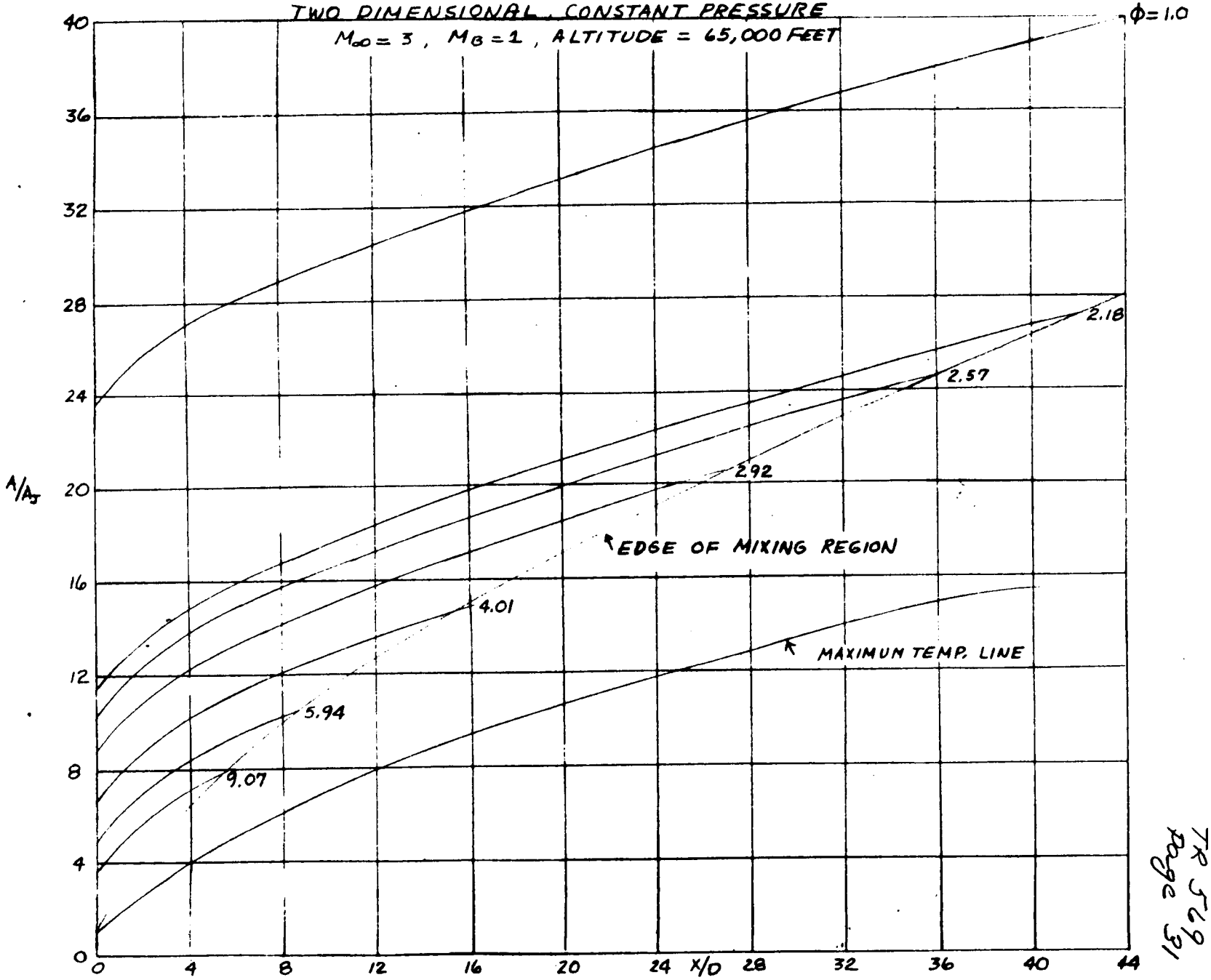

TR 569
Page 31

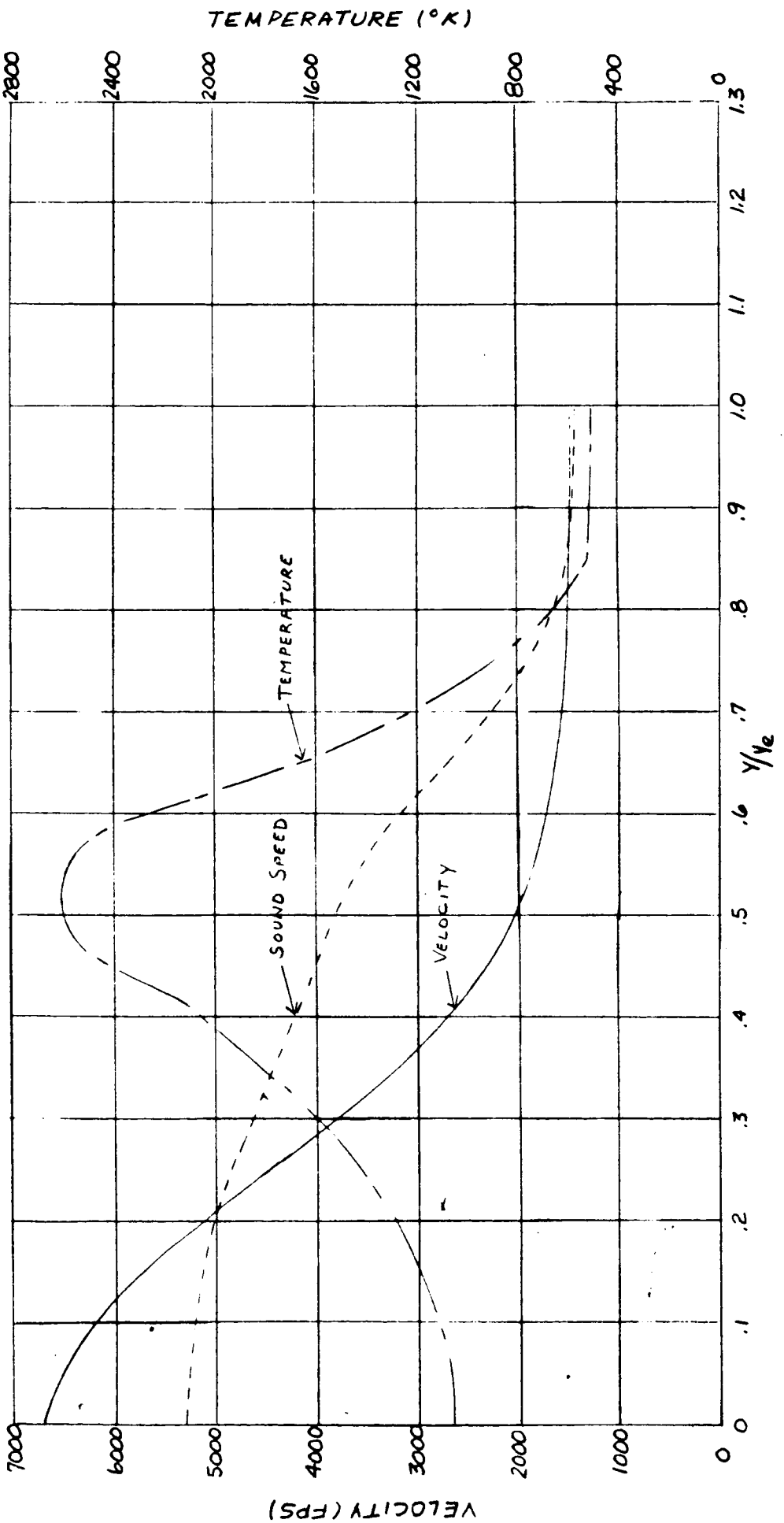

FIG. 66' RADIAL PROFILES OF VELOCITY, TEMPERATURE, AND SOUND SPEED AT $\frac{X}{D} = 20$
TWO DIMENSIONAL, CONSTANT PRESSURE
$M_\infty = 3$, $M_B = 1$, ALTITUDE = 65,000 FEET

FIG. 6c MIXING AND COMBUSTION REGION
TWO DIMENSIONAL, CONSTANT PRESSURE
$M_\infty = 3$, $M_b = 1$, ALTITUDE = 85,000 FEET

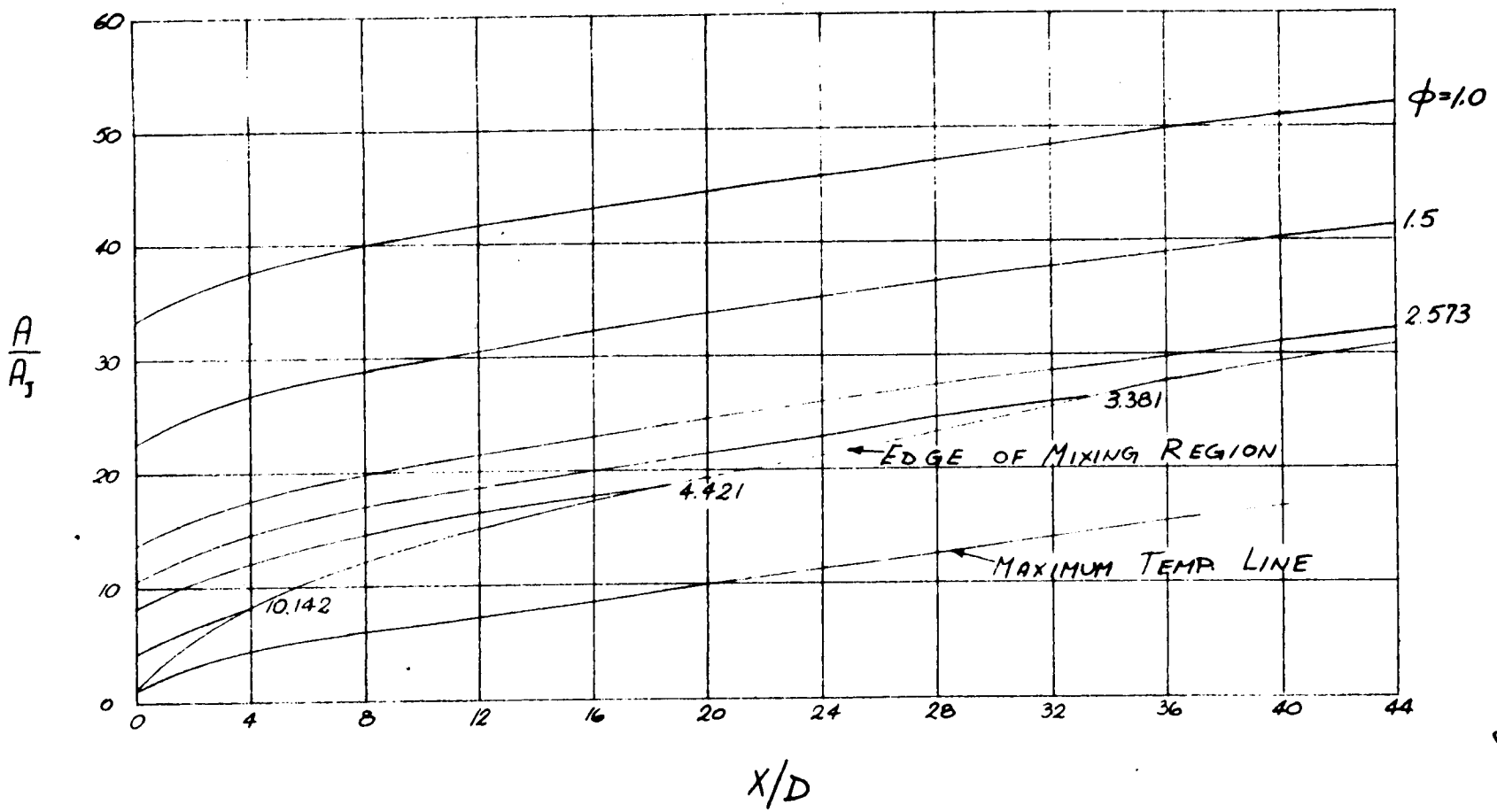

FIG. 6c' RADIAL PROFILES OF VELOCITY, TEMPERATURE, AND SOUND SPEED AT x/D = 20. TWO DIMENSIONAL, CONSTANT PRESSURE $M_\infty = 5$, $M_{\delta} = 1$, ALTITUDE = 85,000 FEET

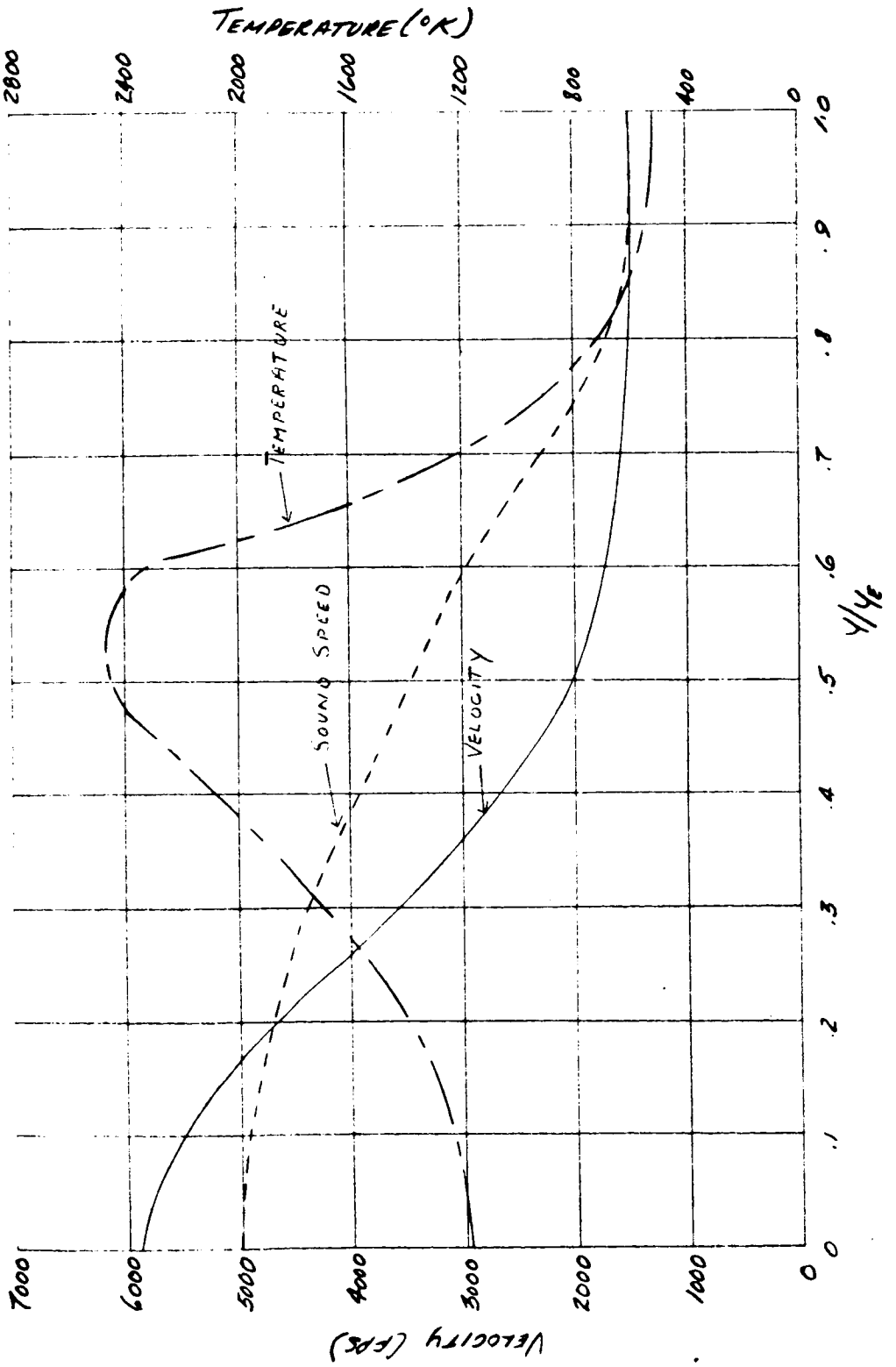

FIG. 6c" RADIAL PROFILES OF VELOCITY, TEMPERATURE, AND SOUND SPEED AT X/D=40.
TWO DIMENSIONAL, CONSTANT PRESSURE
$M_\infty = 3.$, $M_B = 1$, ALTITUDE = 85,000 FEET

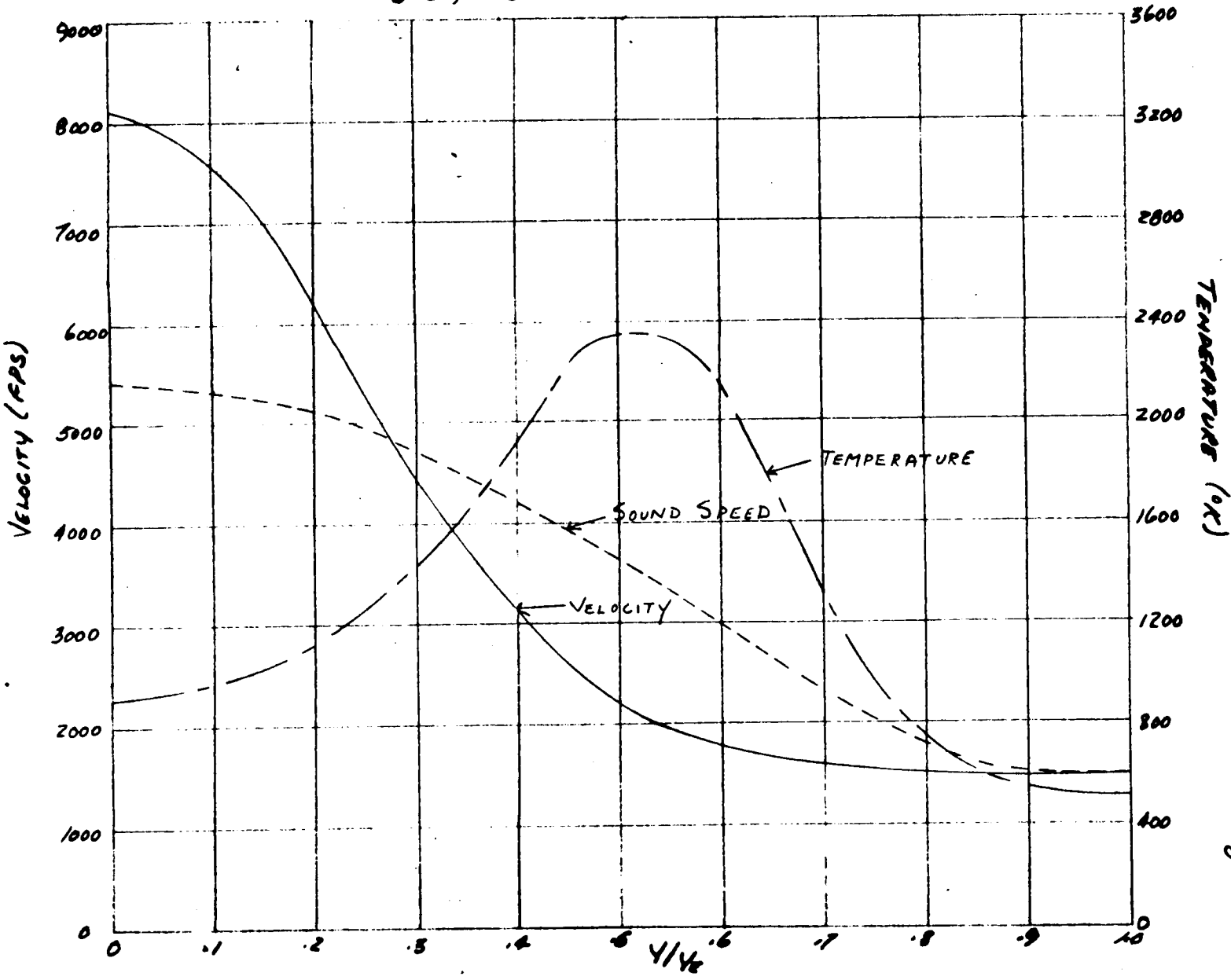

TR 569
Page 35

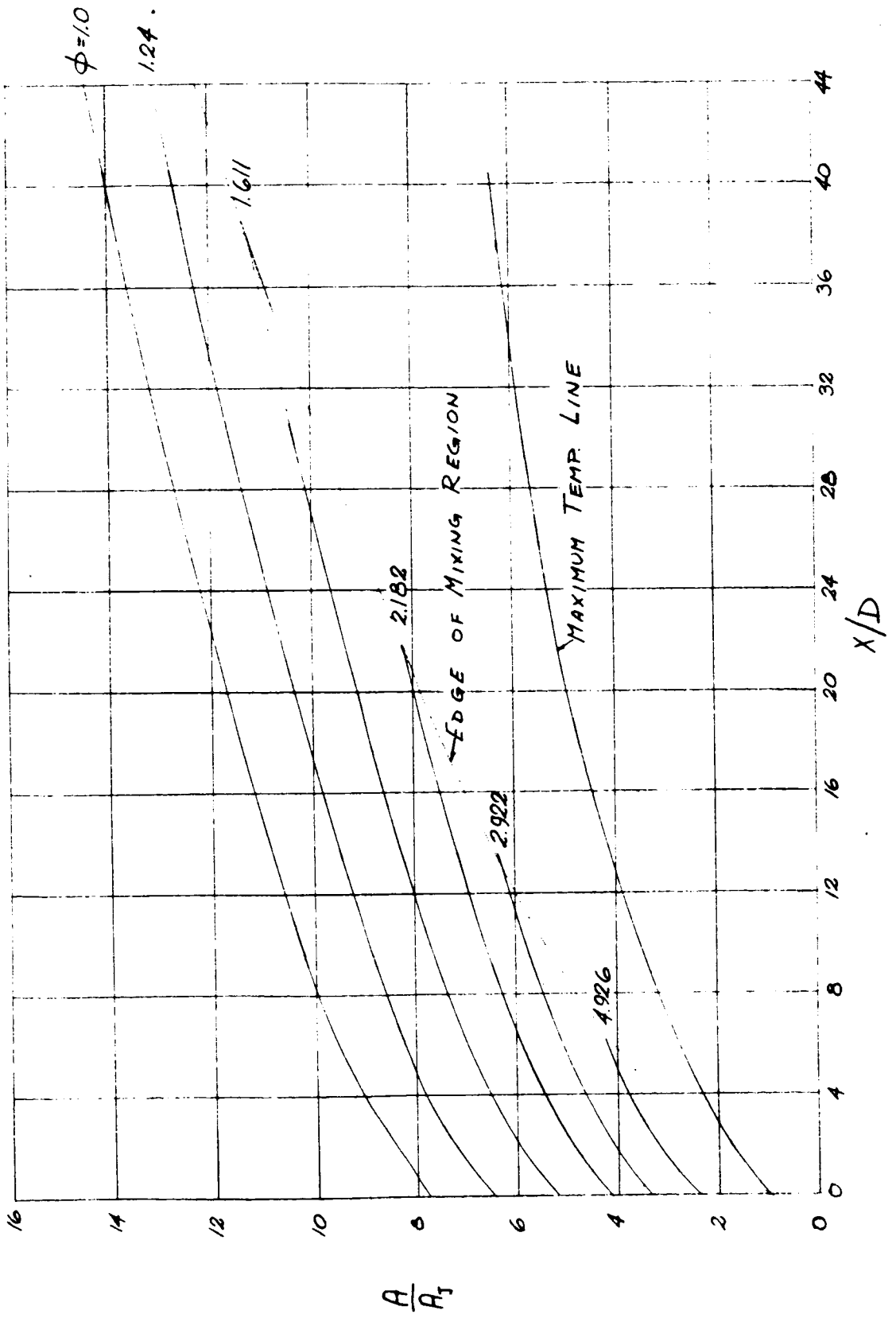

FIG. 6d MIXING AND COMBUSTION REGION
TWO DIMENSIONAL, CONSTANT PRESSURE
$M_o = 6$, $M_b = 2$, ALTITUDE = 75,000 FEET

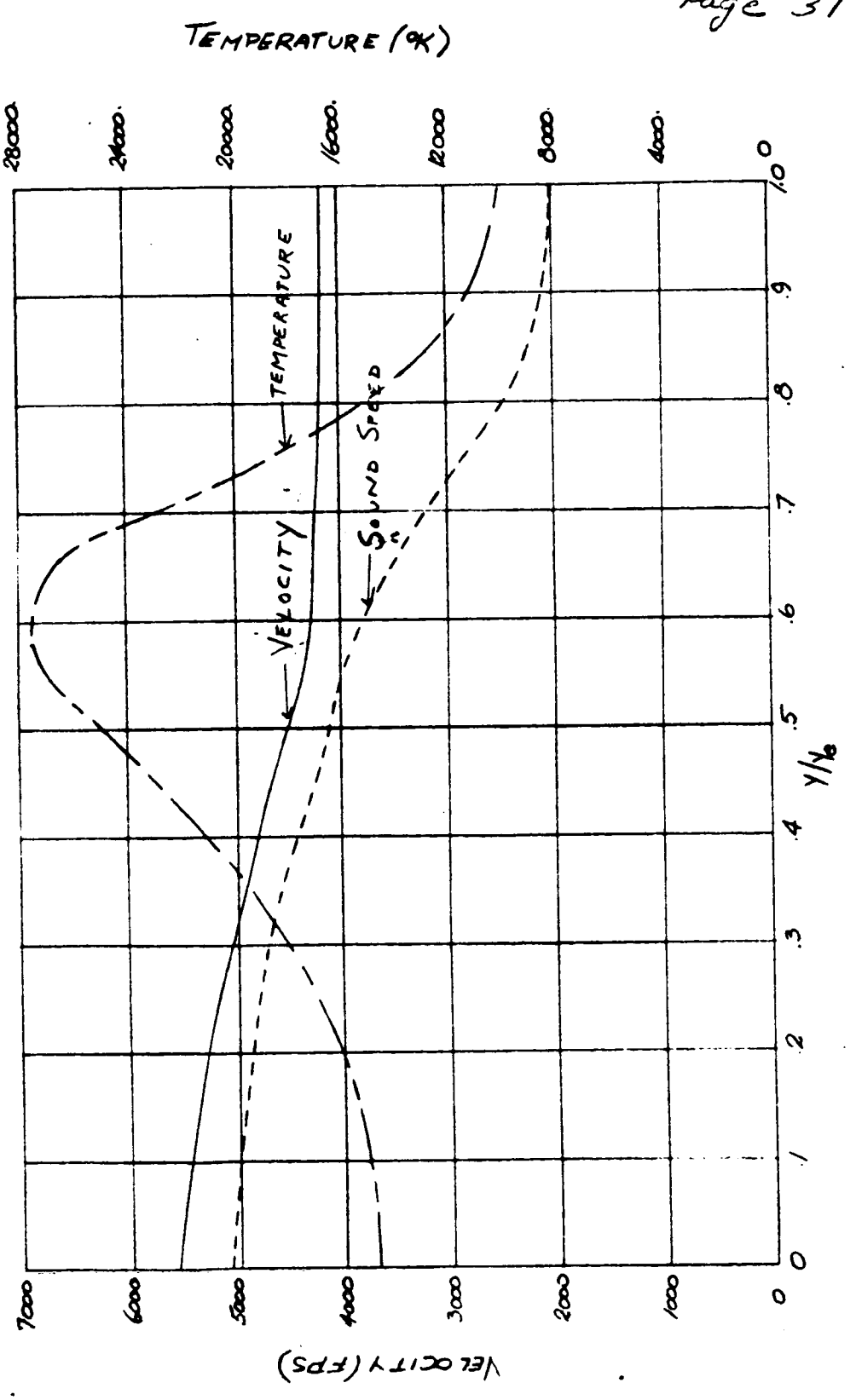

FIG. 6 d' RADIAL PROFILES OF VELOCITY, TEMPERATURE, AND SOUND SPEED AT $\frac{X}{D}=20$
TWO DIMENSIONAL, CONSTANT PRESSURE
$M_\infty=6$, $M_b=2$, ALTITUDE = 75,000 FEET

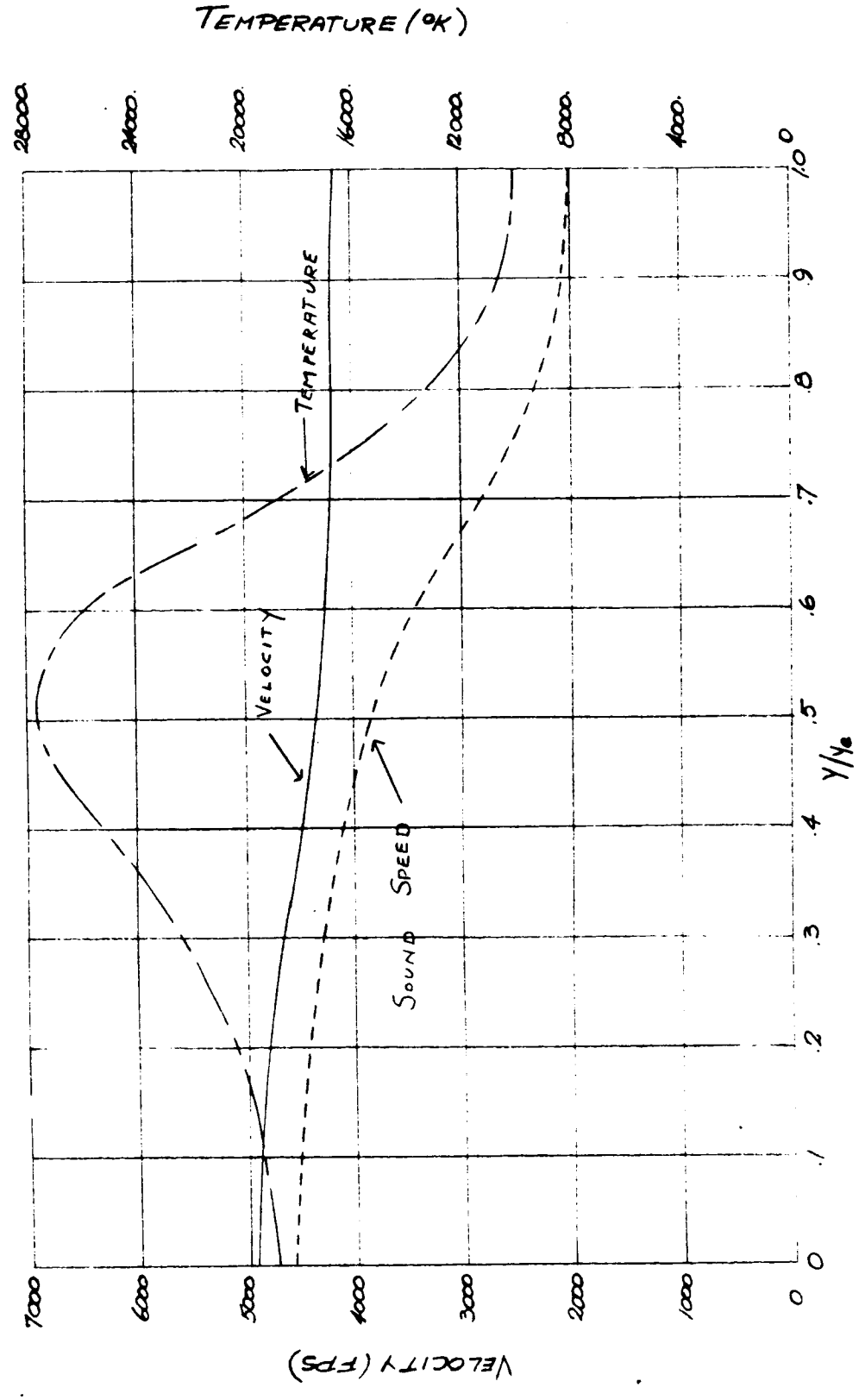

FIG. 6d' RADIAL PROFILES OF VELOCITY, TEMPERATURE, AND SOUND SPEED AT $\frac{X}{D}$ = 40
TWO DIMENSIONAL, CONSTANT PRESSURE
M_o = 6 , M_b = 2 , ALTITUDE = 75,000 FEET

Fig. 6e MIXING and COMBUSTION REGION
TWO DIMENSIONAL, CONSTANT PRESSURE
$M_\infty = 6.$, $M_b = 2.$, ALTITUDE = 90,000 FEET

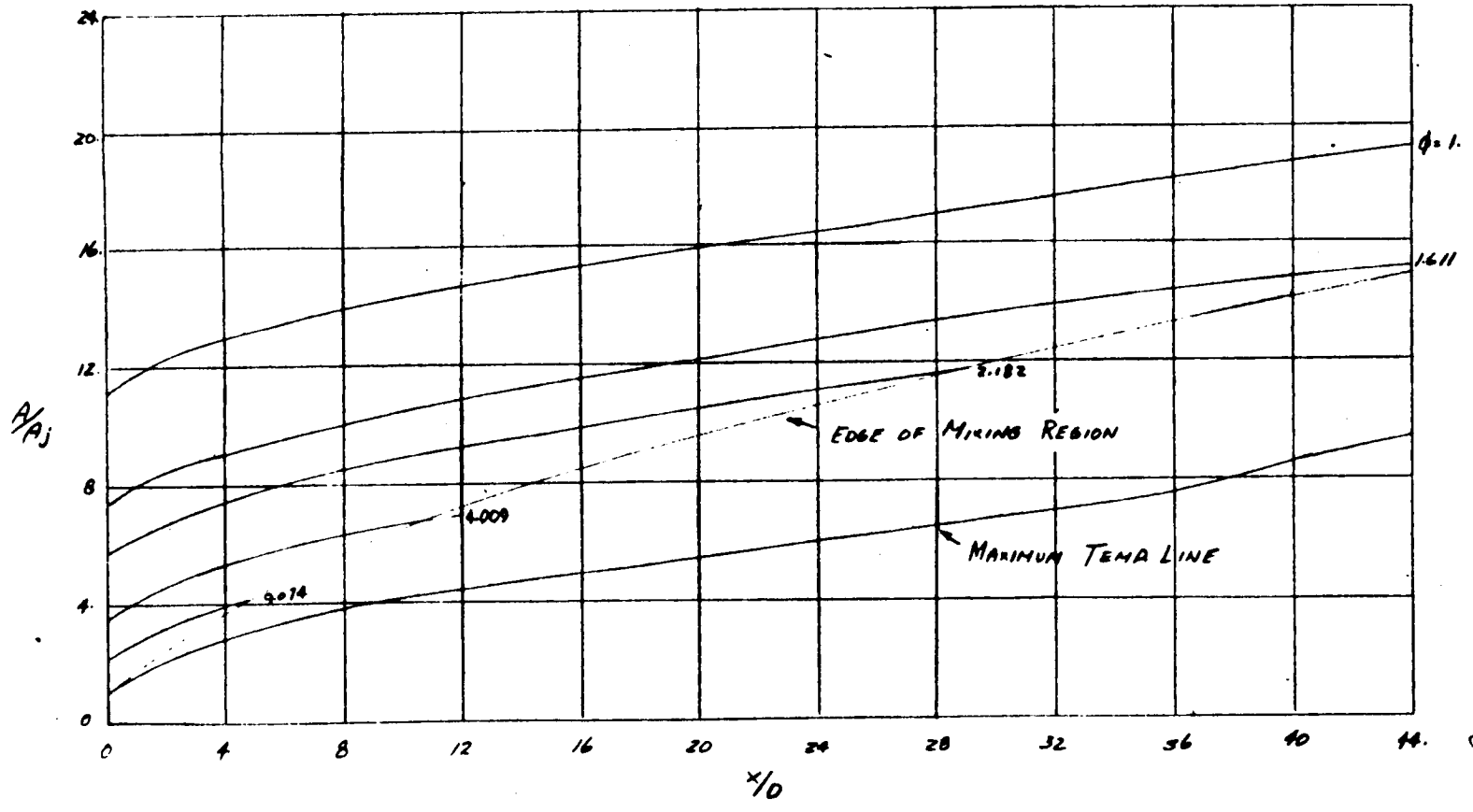

FIG. 6e' RADIAL PROFILES OF VELOCITY, TEMPERATURE, AND SOUND SPEED AT X/D = 20. TWO DIMENSIONAL, CONSTANT PRESSURE $M_0 = 6.$, $M_0 = 2.$, ALTITUDE = 90,000 FEET

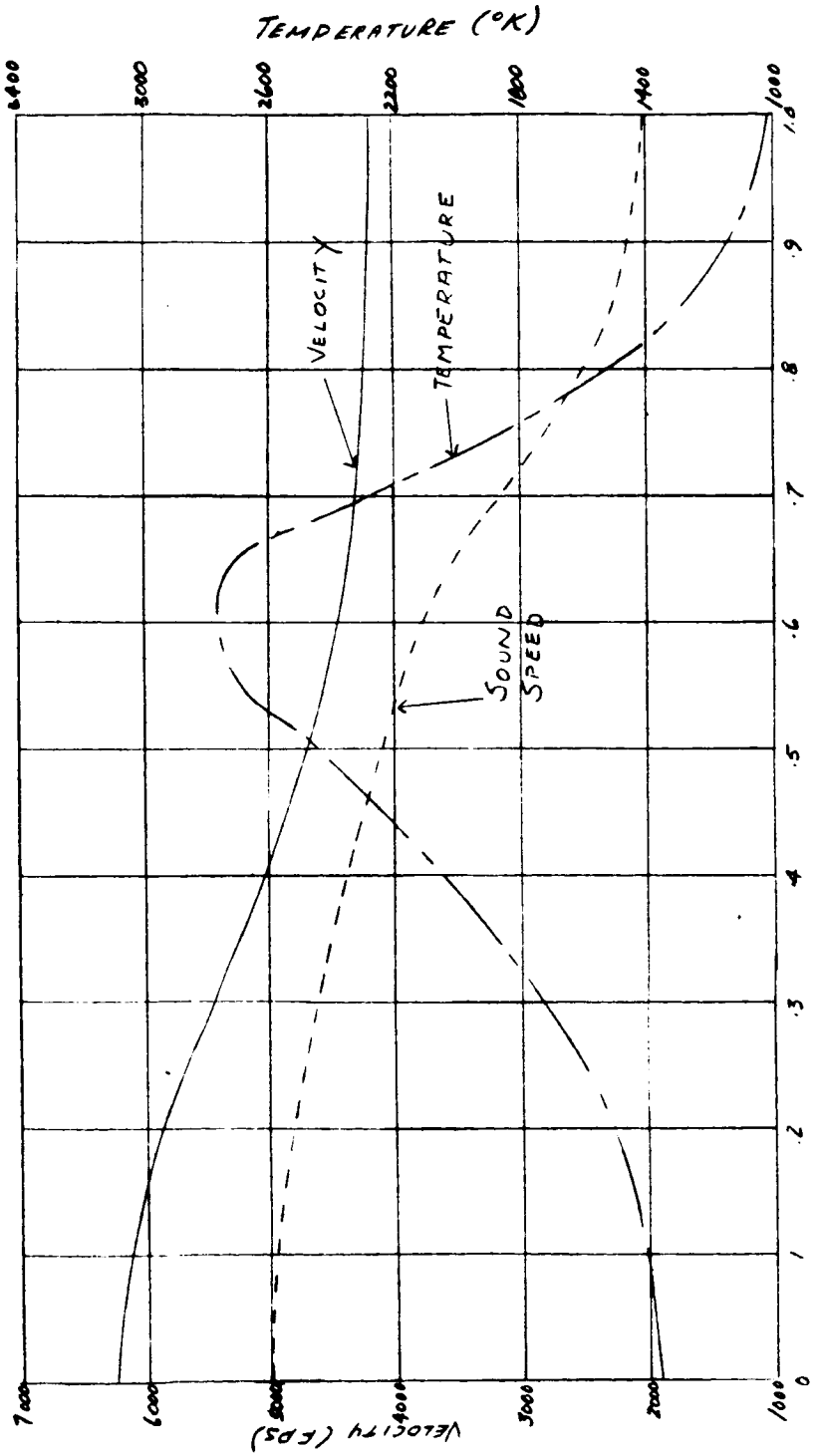

FIG. 6e" RADIAL PROFILES OF VELOCITY, TEMPERATURE AND SOUND SPEED AT X/D. 40.
TWO DIMENSIONAL, CONSTANT PRESSURE
$M_0 = 6.$, $M_0 = 2.$ ALTITUDE. 90000 FEET

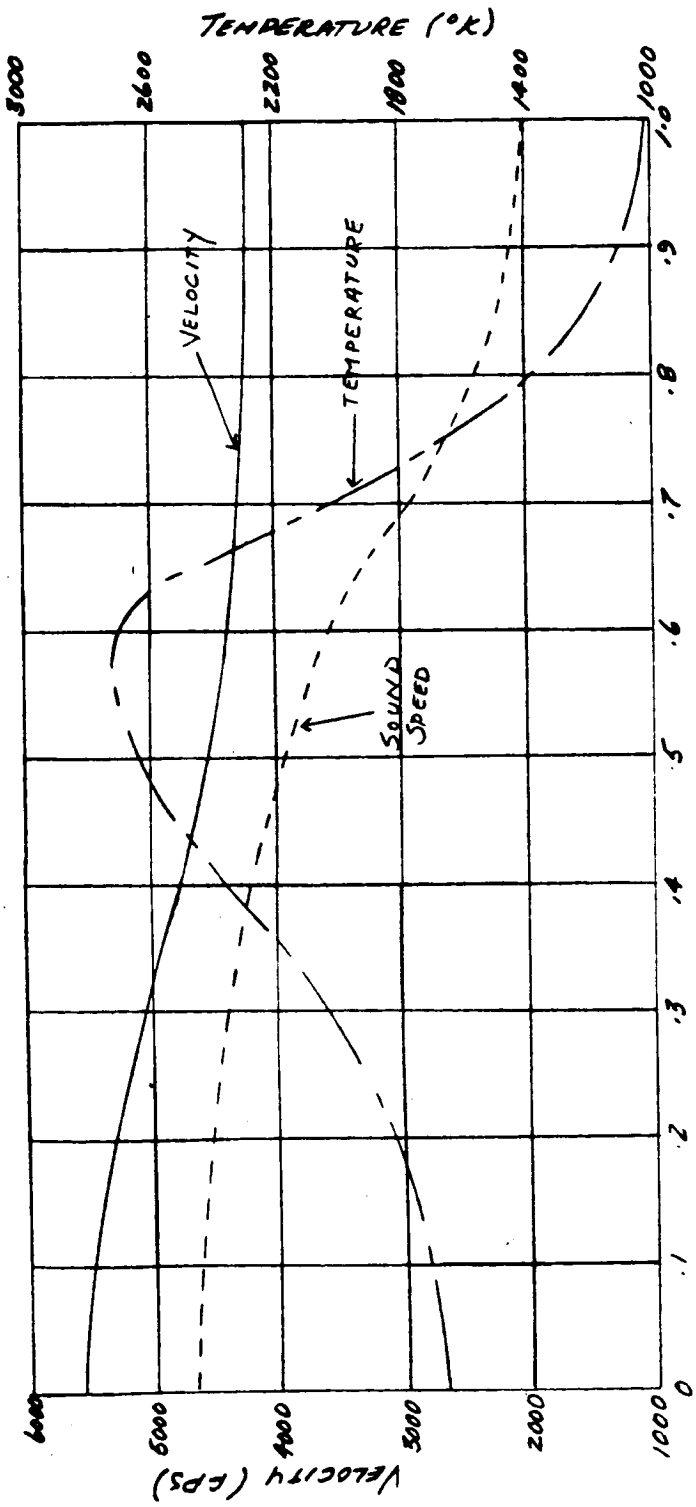

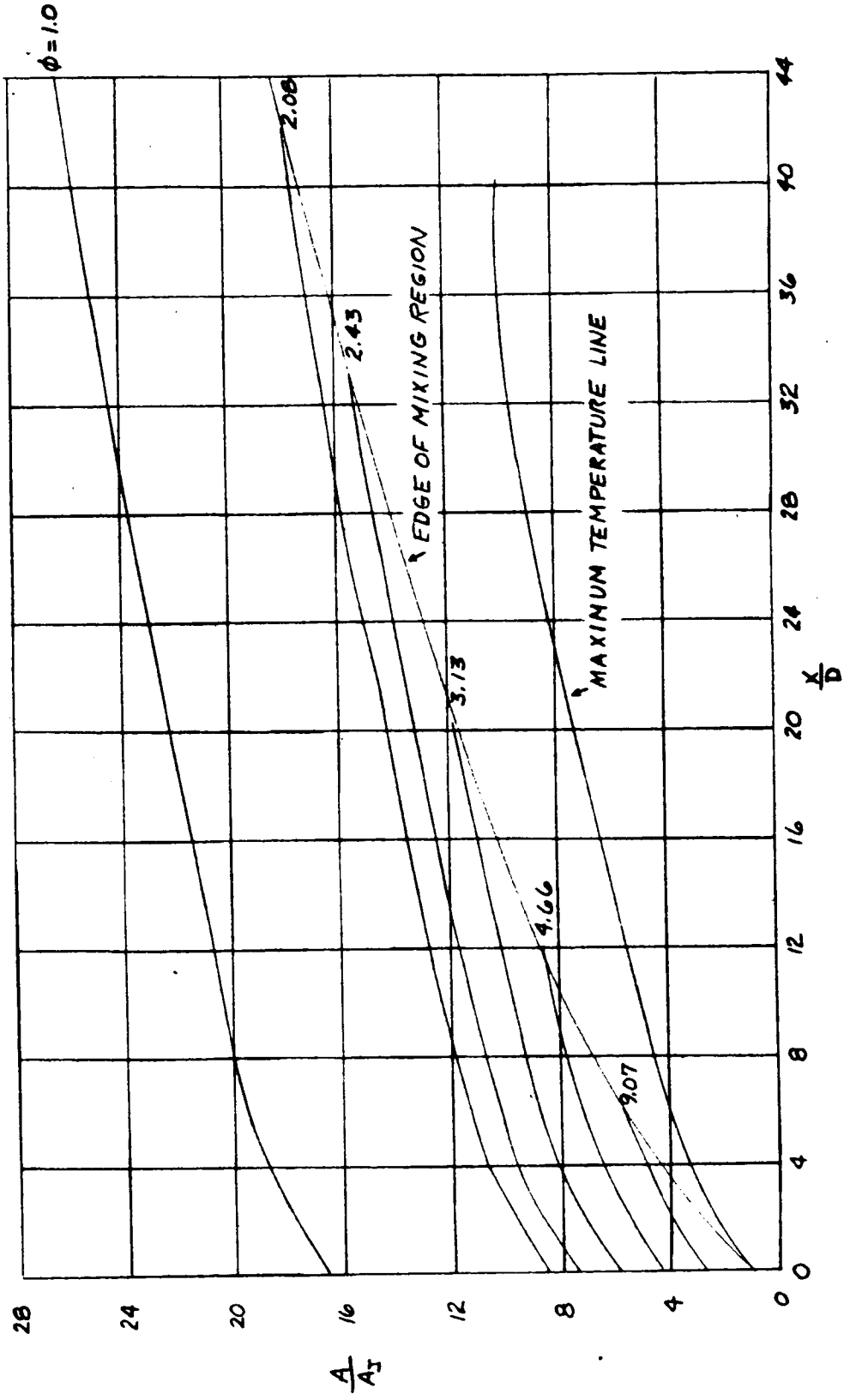

FIG. 6P MIXING AND COMBUSTION REGION
TWO DIMENSIONAL, CONSTANT PRESSURE
$M_\infty = 6$. $M_0 = 2$, ALTITUDE = 110,000 FEET

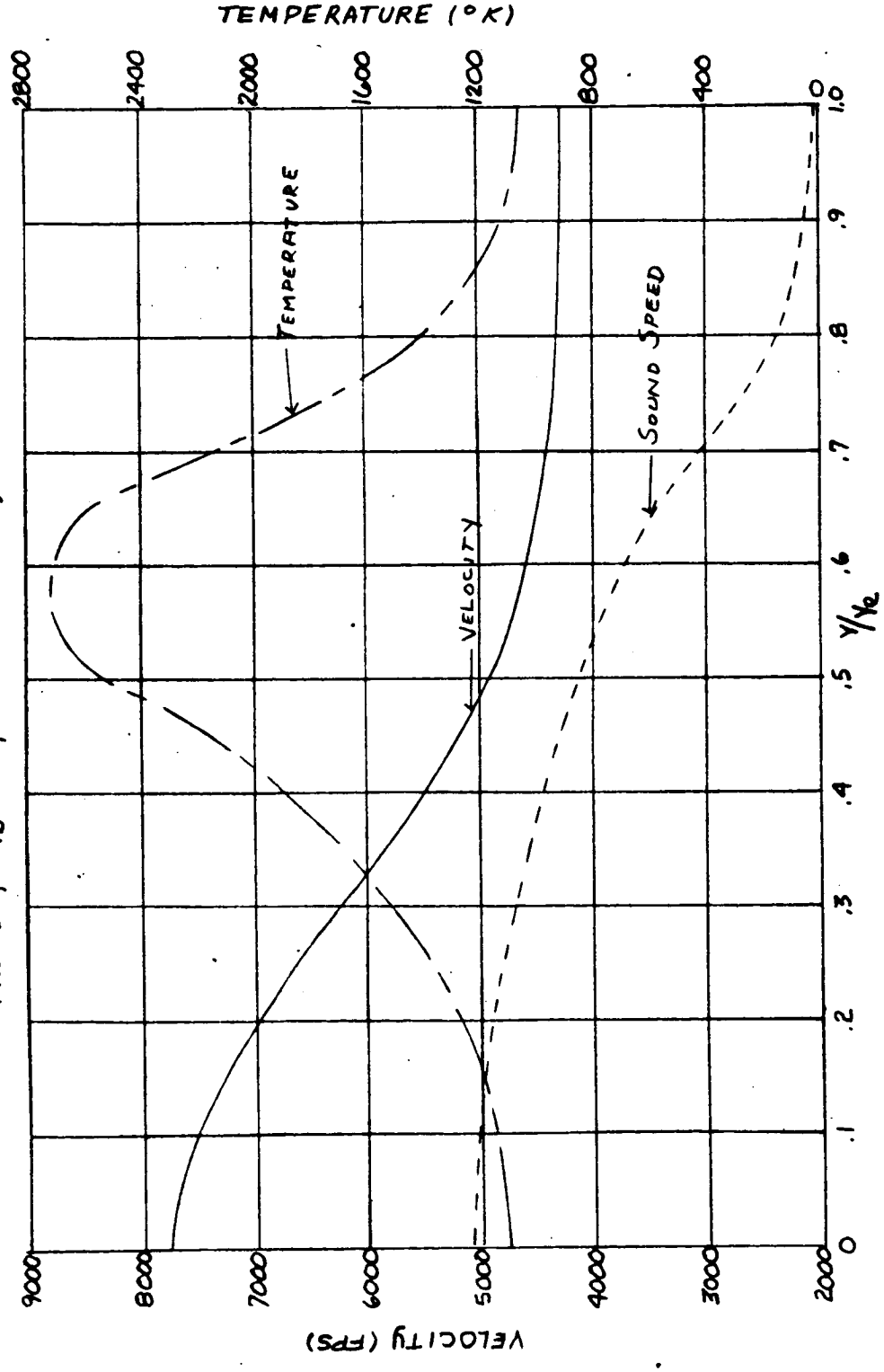

FIG. 6 RADIAL PROFILES OF VELOCITY, TEMPERATURE, AND SOUND SPEED AT $\frac{X}{D} = 20$
TWO DIMENSIONAL, CONSTANT PRESSURE
$M_{\infty}=6$, $M_B=2$, ALTITUDE = 110,000 FEET

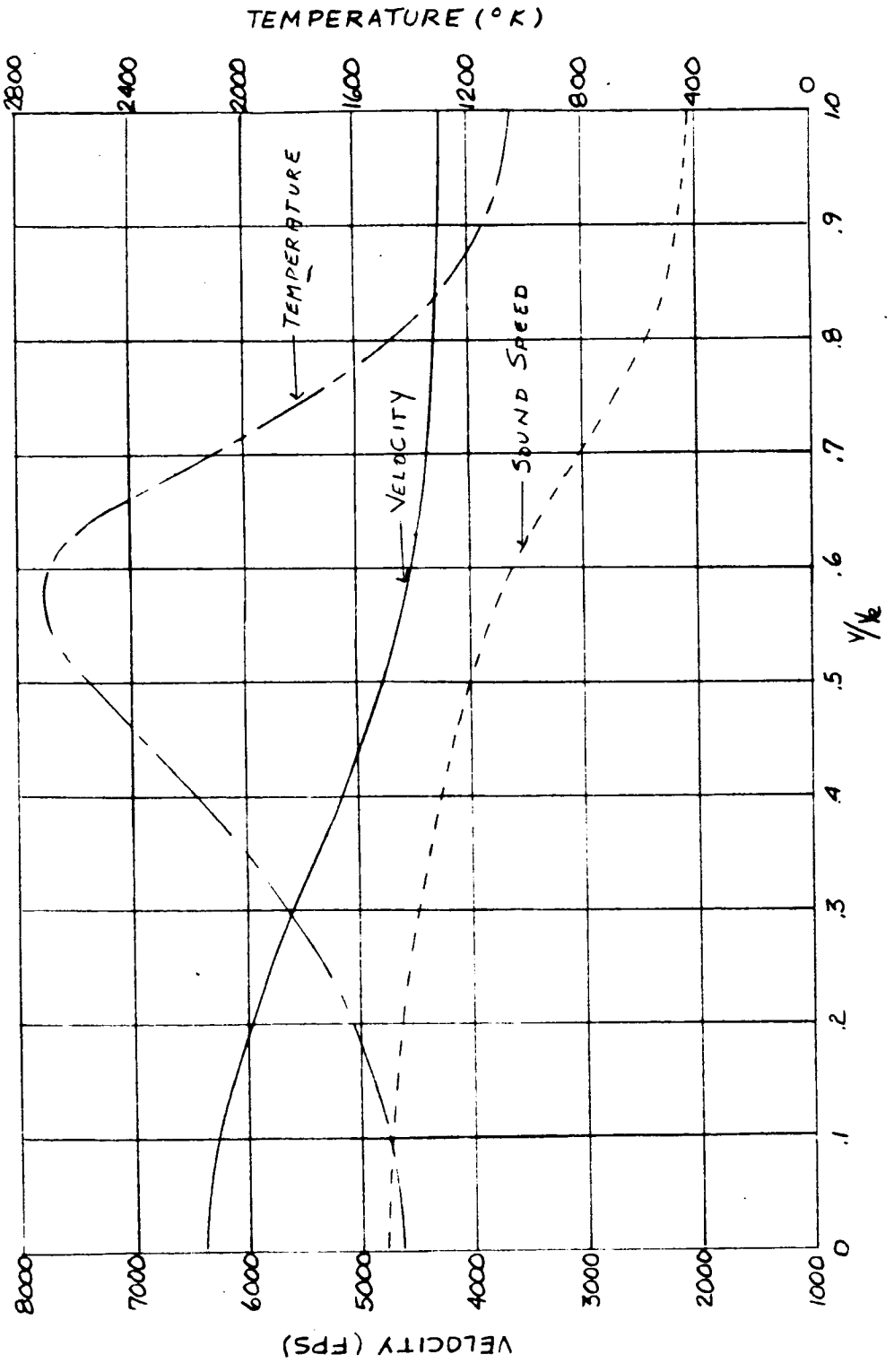

FIG. 64" RADIAL PROFILES OF VELOCITY, TEMPERATURE, AND SOUND SPEED AT $\frac{X}{D} = 40$
TWO DIMENSIONAL, CONSTANT PRESSURE
$M_\infty = 6$, $M_B = 2$, ALTITUDE = 110,000 FEET

FIG. 69 MIXING AND COMBUSTION REGION

TWO DIMENSIONAL, CONSTANT PRESSURE

$M_0 = 8.$, $M_B = 3.26$ ALTITUDE = 85,000 FEET

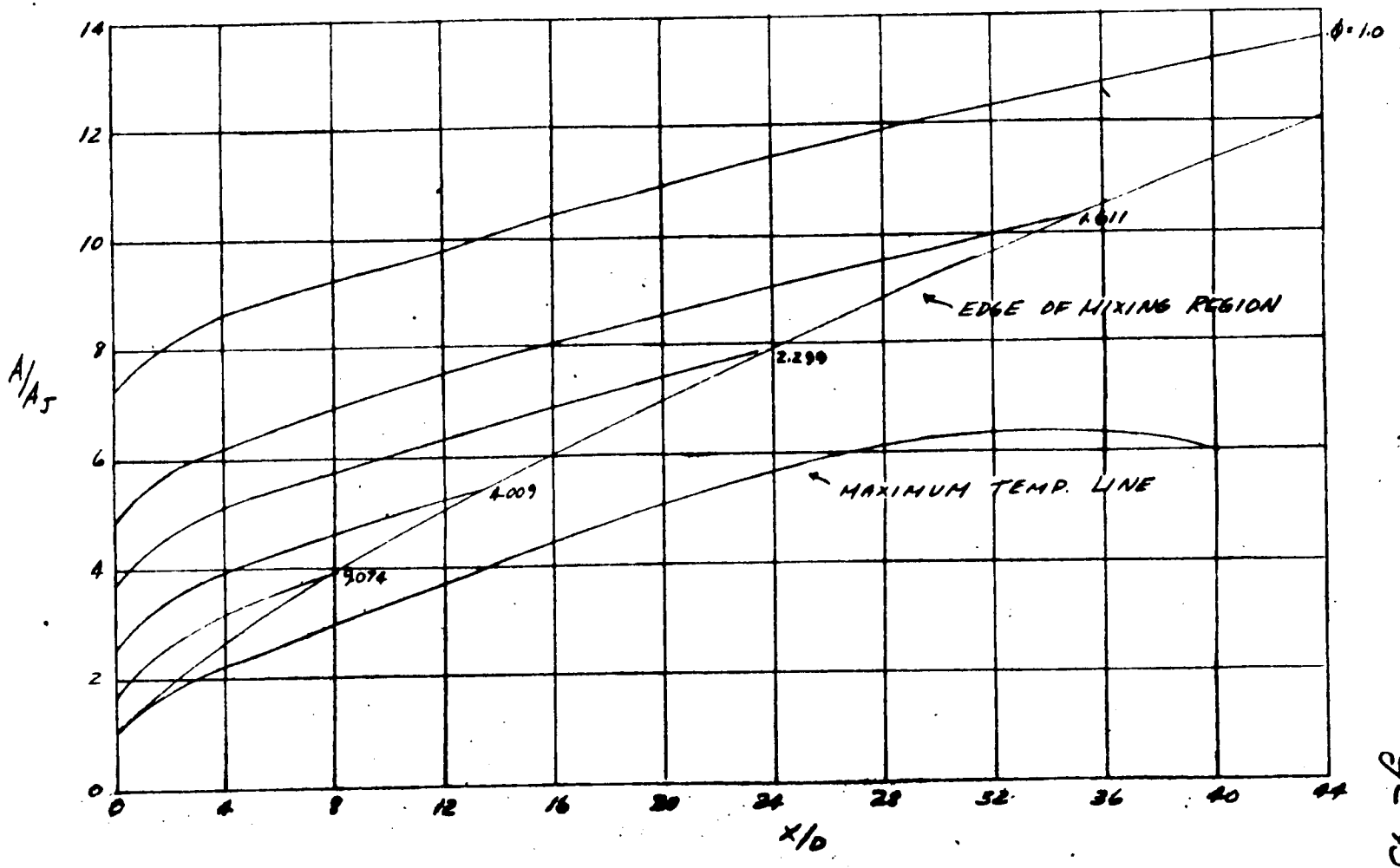

TR 58-9
Page 115

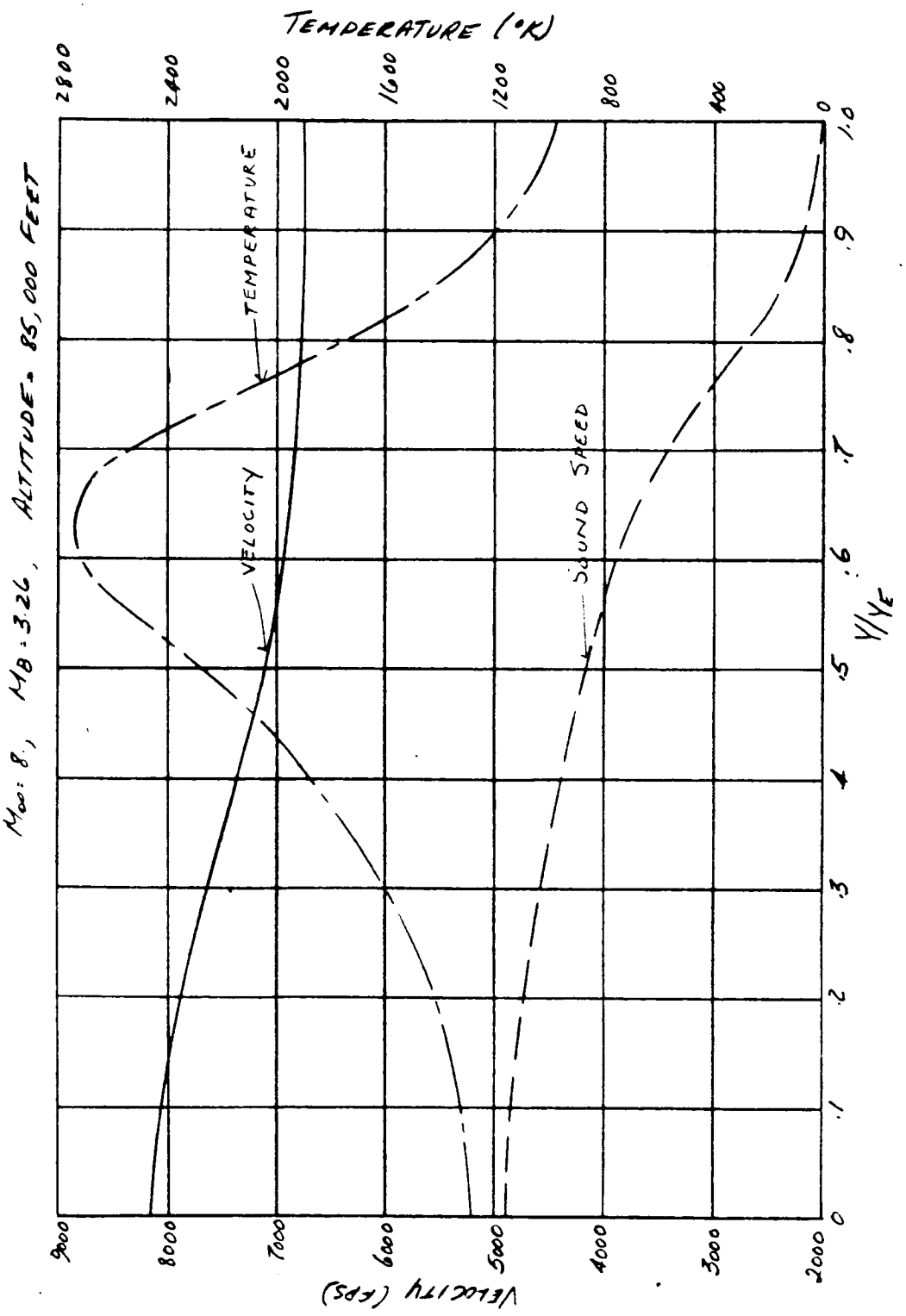

FIG 69' RADIAL PROFILES OF VELOCITY, TEMPERATURE, AND SOUND SPEED AT X/D = 20.
TWO DIMENSIONAL, CONSTANT PRESSURE
$M_\infty = 8$, $M_B = 3.26$, ALTITUDE = 85,000 FEET

Fig. 6g" Radial Profiles of Velocity, Temperature, and Sound Speed at $x/D = 40$.
Two Dimensional, Constant Pressure
$M_\infty = 8.$, $M_B = .326$, Altitude = 85,000 feet

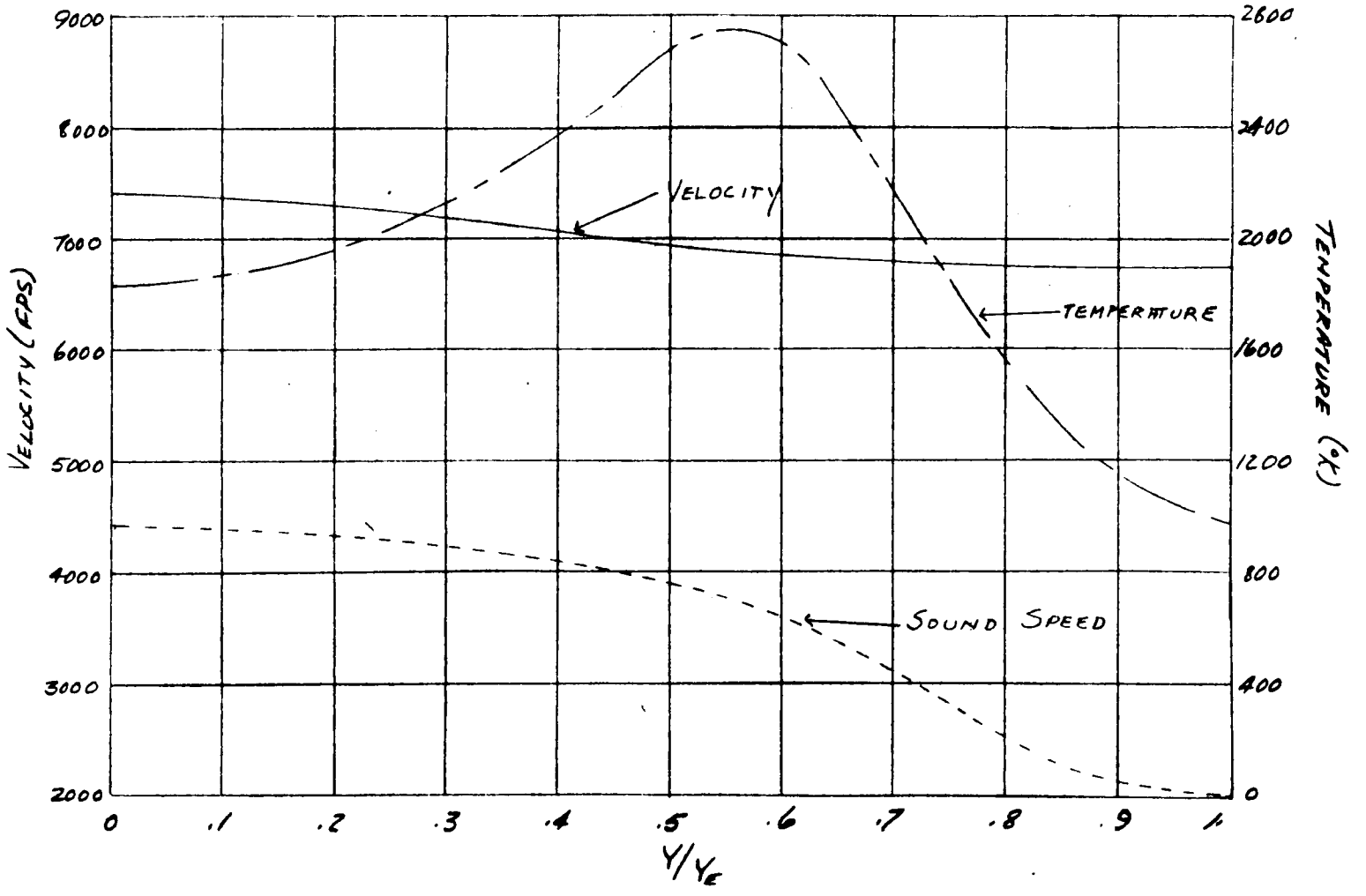

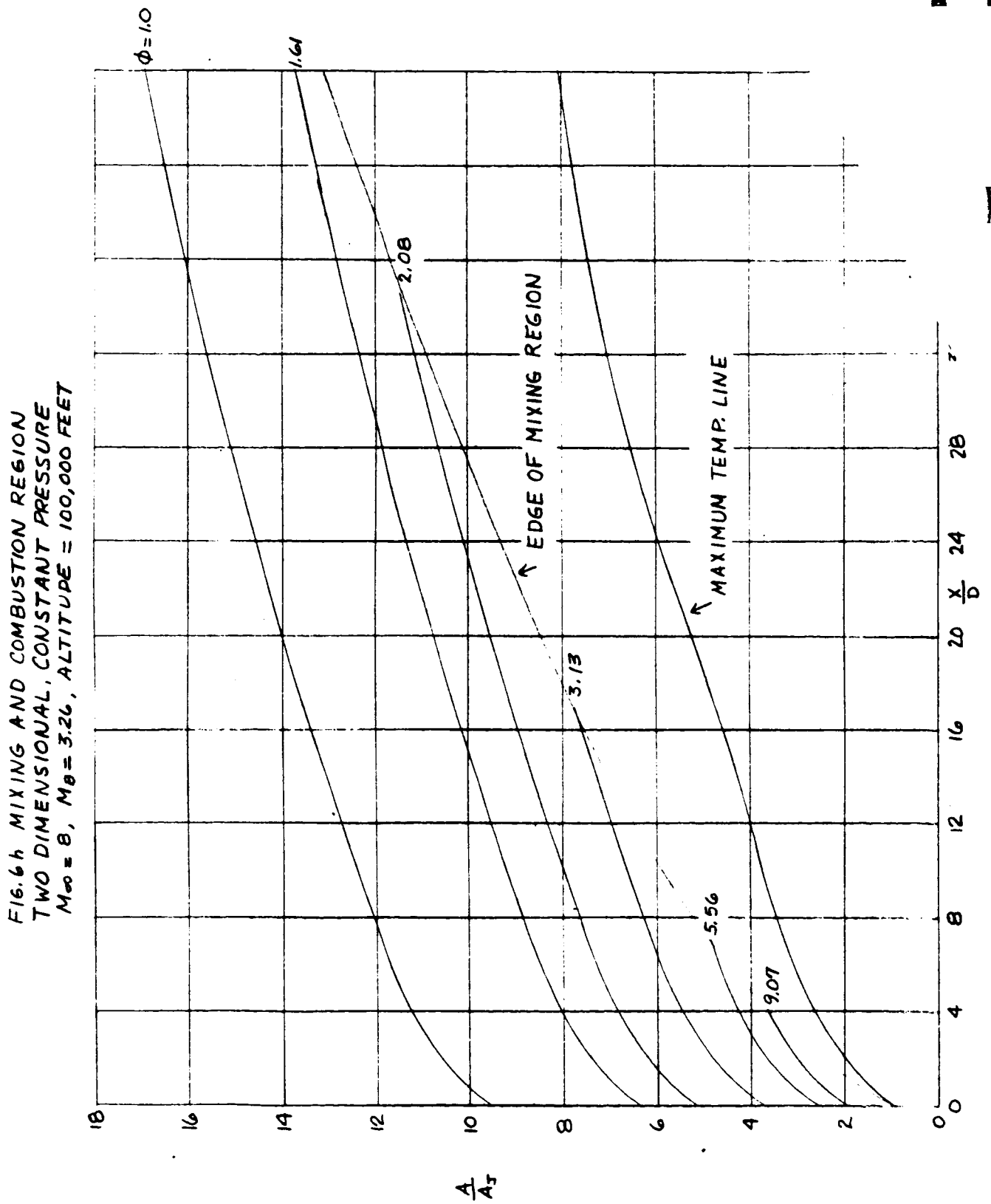

FIG. 6h MIXING AND COMBUSTION REGION
TWO DIMENSIONAL, CONSTANT PRESSURE
$M_\infty = 8$, $M_B = 3.26$, ALTITUDE = 100,000 FEET

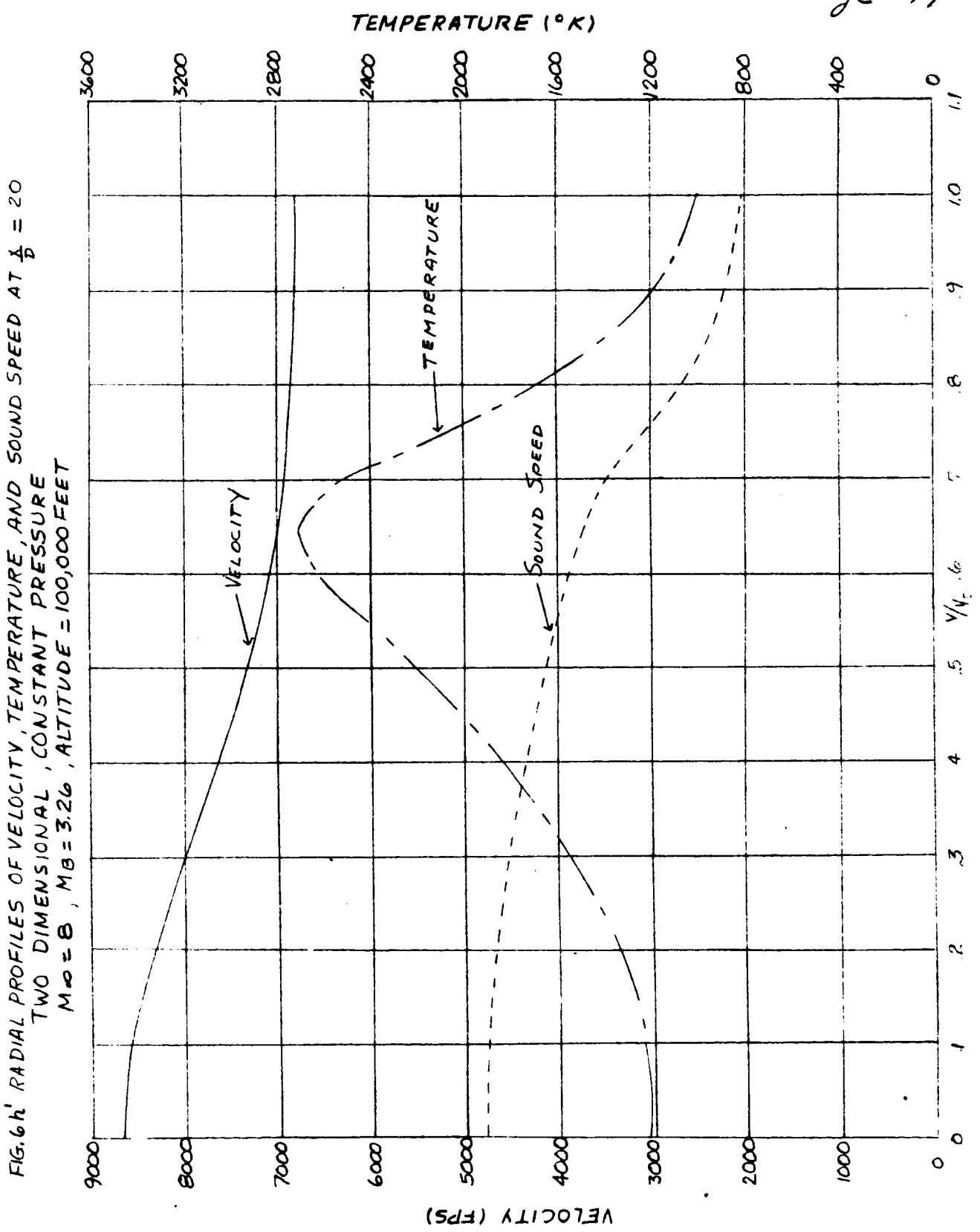

FIG. 6h' RADIAL PROFILES OF VELOCITY, TEMPERATURE, AND SOUND SPEED AT $\frac{A}{D} = 20$
TWO DIMENSIONAL, CONSTANT PRESSURE
$M_\infty = 8$, $M_B = 3.26$, ALTITUDE = 100,000 FEET

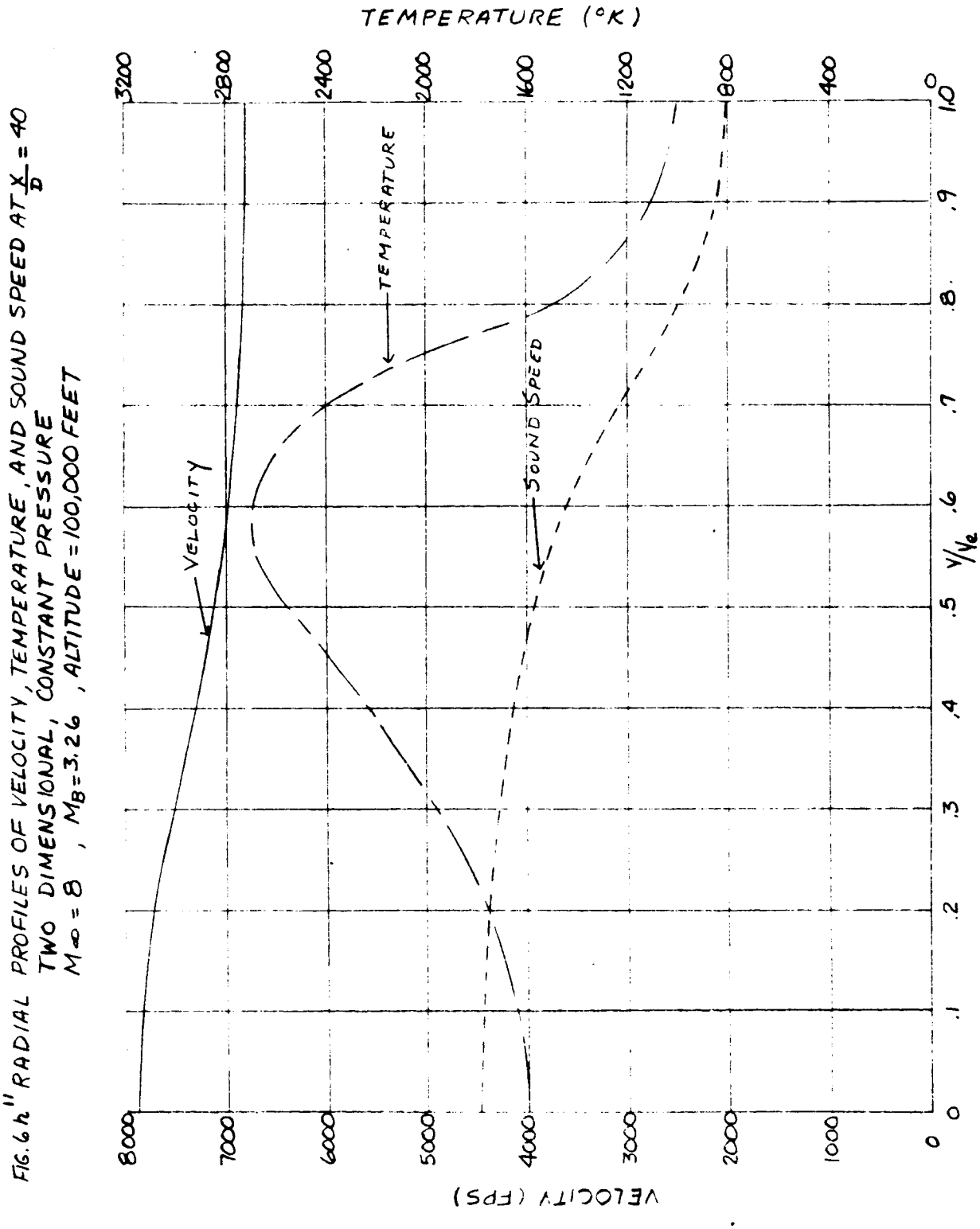

FIG. 6 h" RADIAL PROFILES OF VELOCITY, TEMPERATURE, AND SOUND SPEED AT $\frac{X}{D} = 40$
TWO DIMENSIONAL, CONSTANT PRESSURE
$M_\infty = 8$, $M_B = 3.26$, ALTITUDE = 100,000 FEET

FIG 6i MIXING AND COMBUSTION REGION
TWO DIMENSIONAL, CONSTANT PRESSURE
$M_0 = 8$, $M_B = 3.26$, ALTITUDE 120,000 FEET

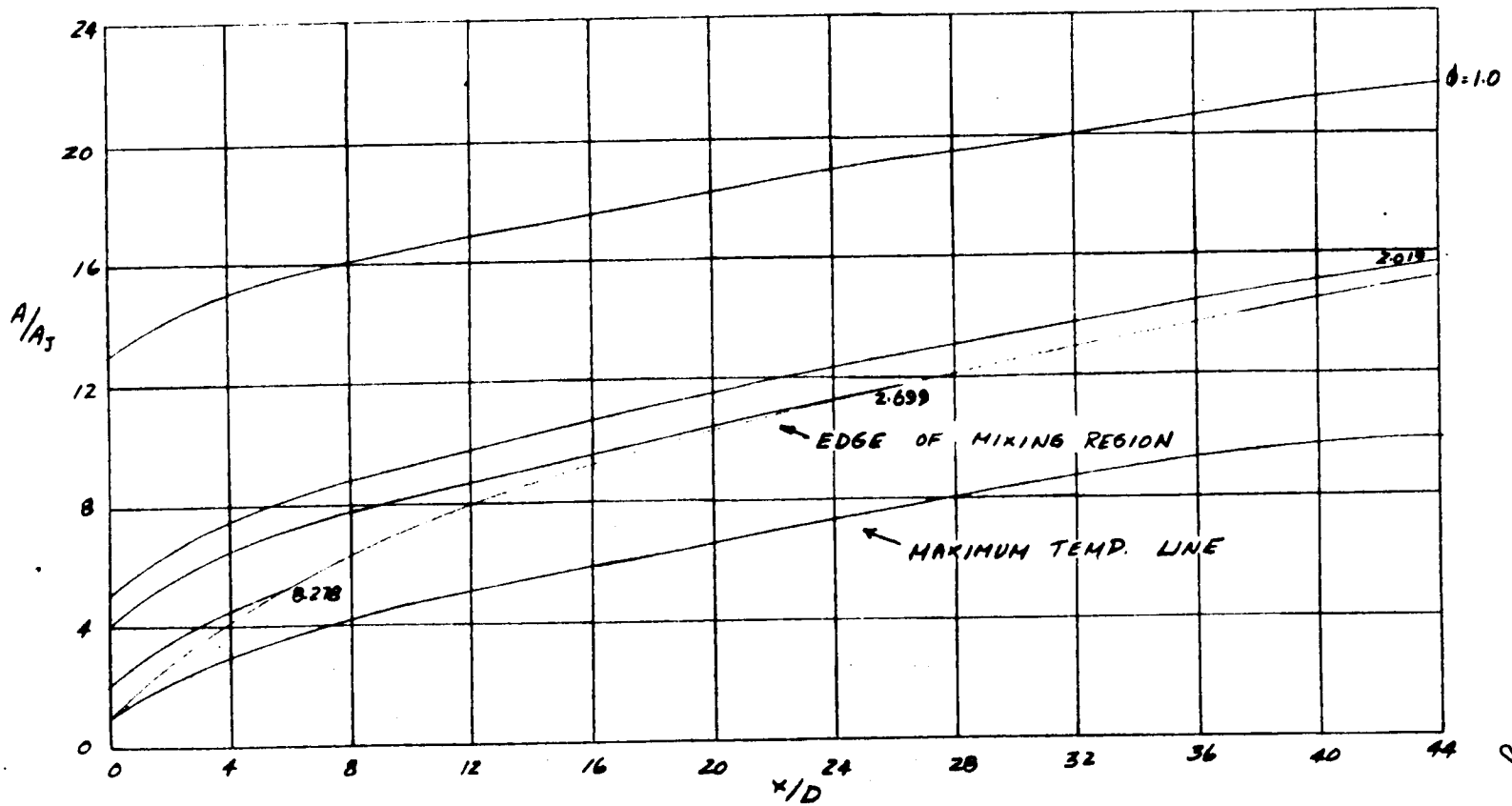

FIG. 6: RADIAL PROFILES OF VELOCITY, TEMPERATURE, AND SOUND SPEED AT
TWO DIMENSIONAL, CONSTANT PRESSURE
$M_\infty = 8.$, $M_B = 3.26$, ALTITUDE = 120,000

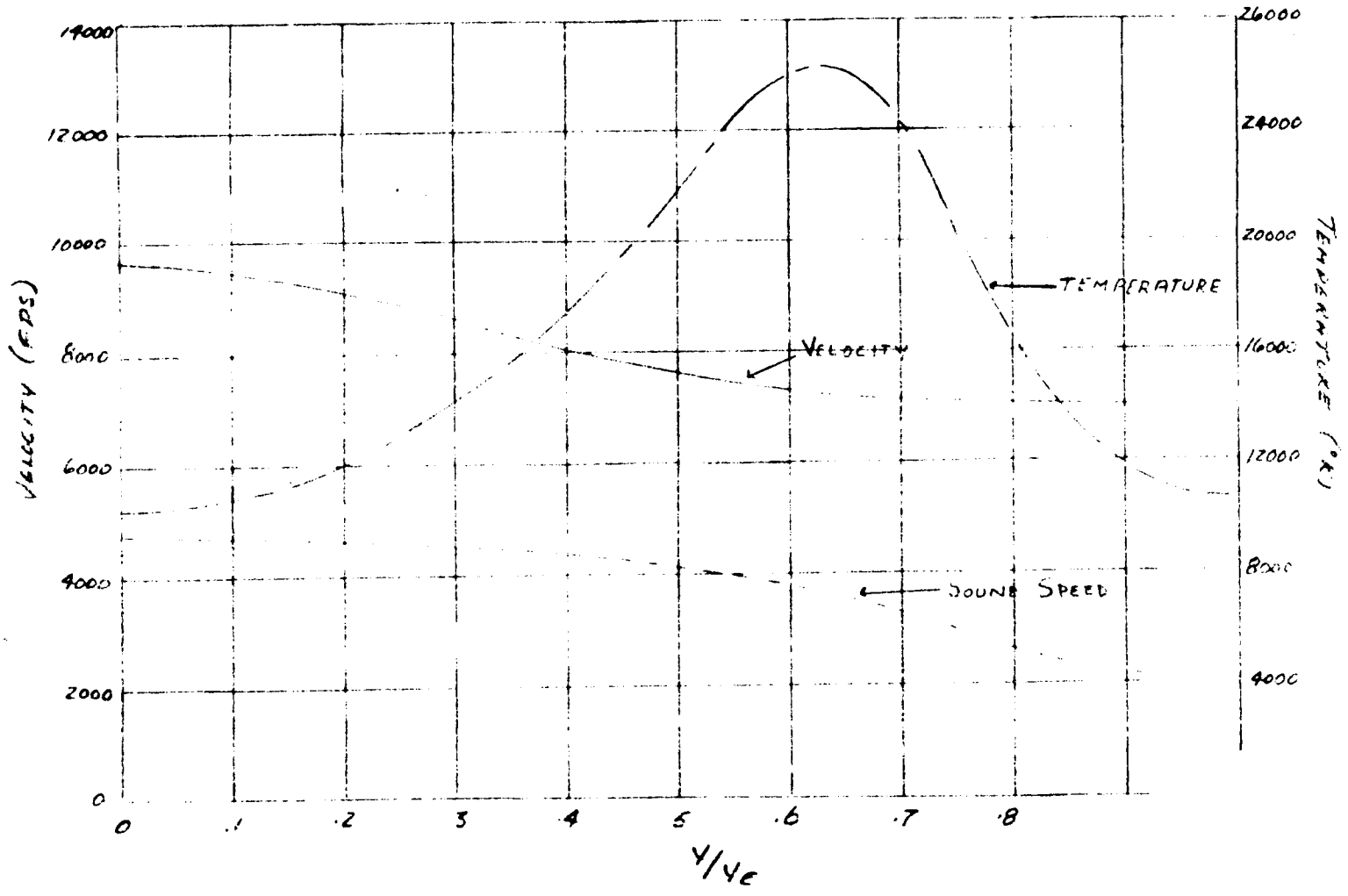

FIG. 61 RADIAL PROFILES OF VELOCITY, TEMPERATURE AND SOUND SPEED AT $X/D = 40$.
TWO DIMENSIONAL, CONSTANT PRESSURE
$M_0 = 8$., $M_B = 3.26$, ALTITUDE = 120,000 FEET

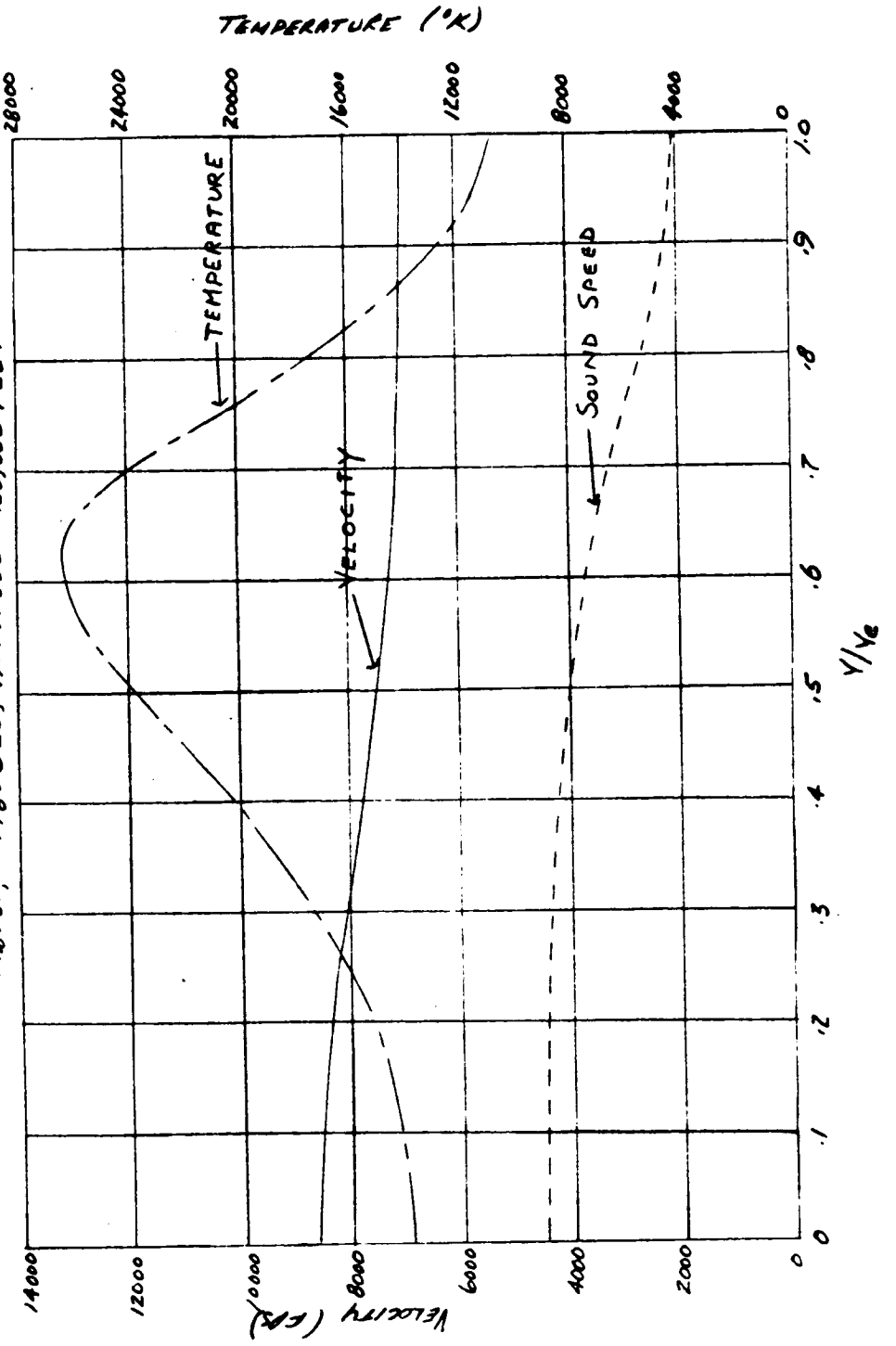

FIGURE 7: FLOW DEFLECTION ANGLE FOR TWO-DIMENSIONAL, CONSTANT PRESSURE MIXING AND COMBUSTION

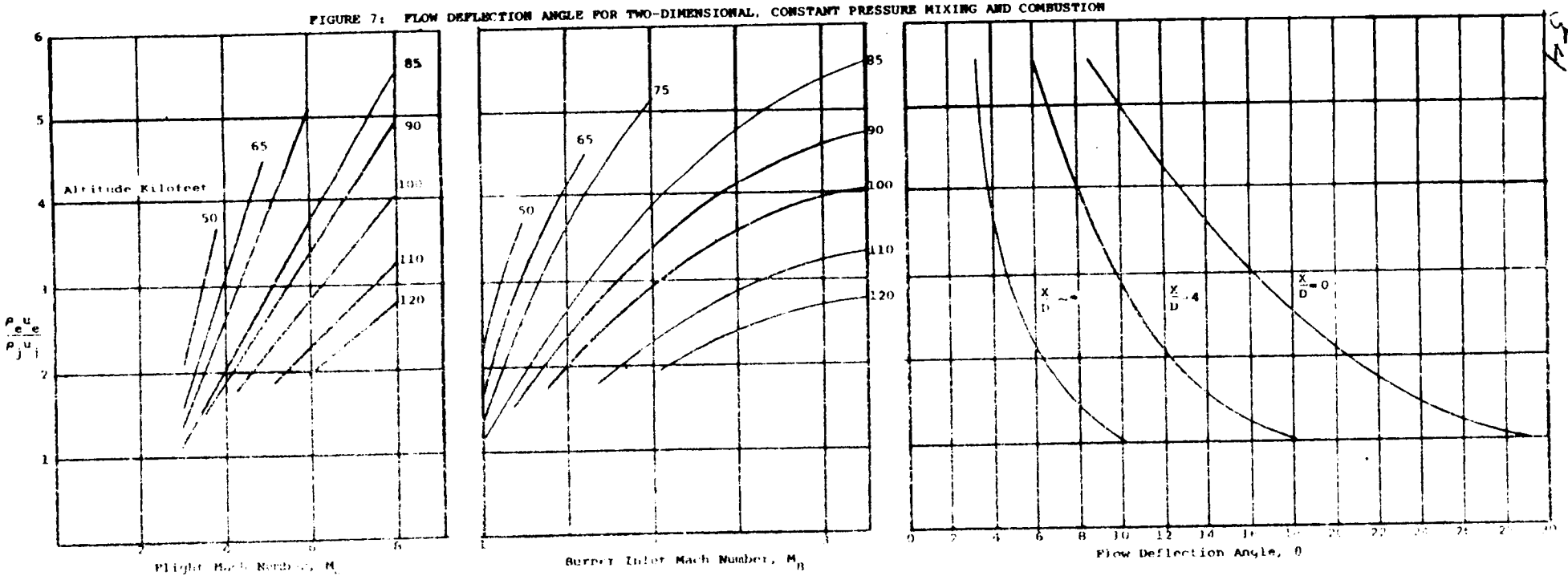

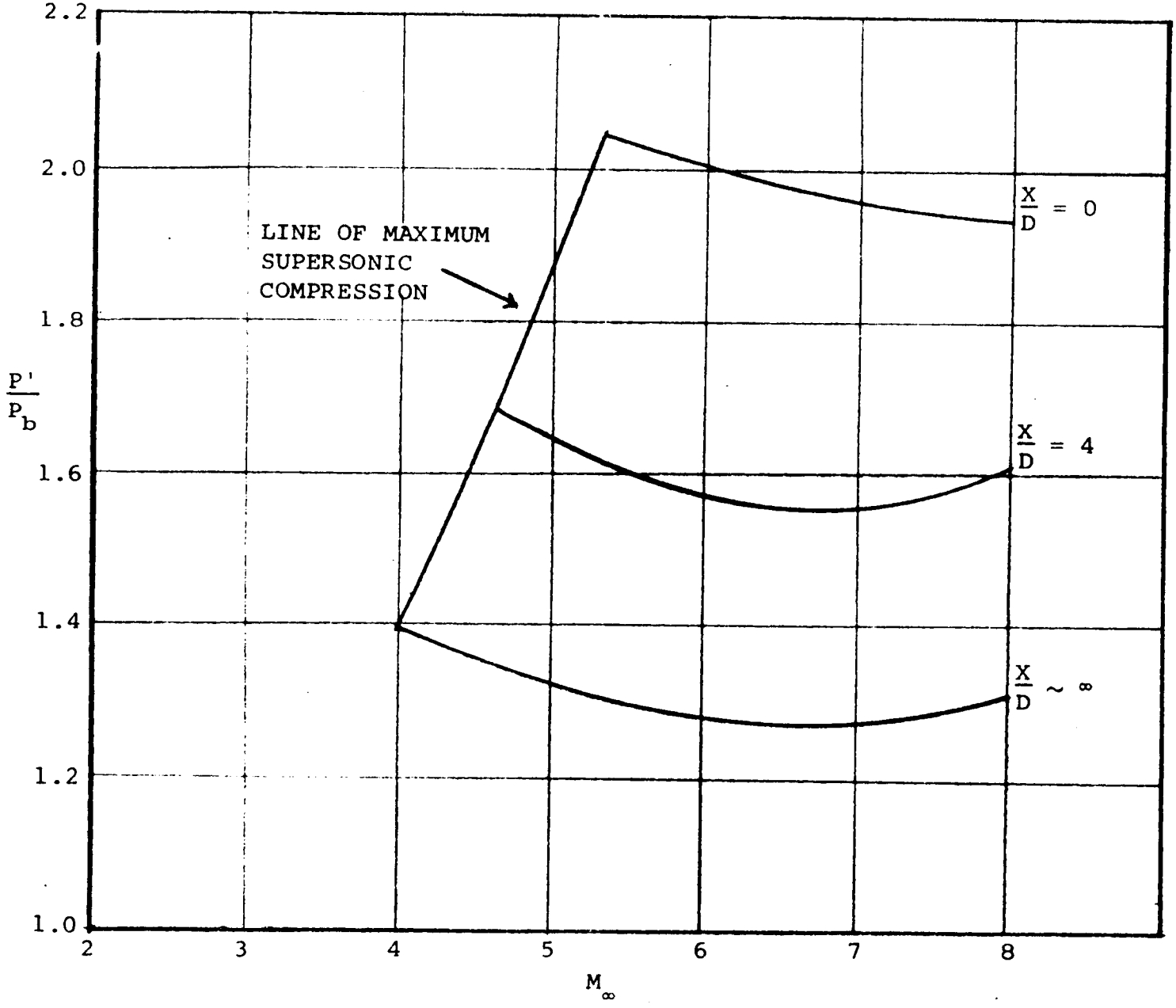

FIGURE 8: THERMAL COMPRESSION IN TWO-DIMENSIONAL DIFFUSION CONTROLLED COMBUSTION FOR AN ALTITUDE OF 85,000 FEET

FIG. 9a. MIXING AND COMBUSTION REGION

TWO DIMENSIONAL, PRESSURE DROP, $P/P_0 = 1 - 0.0125\ X/D$

$M_\infty = 6$, $M_B = 2$., ALTITUDE = 90,000 FEET

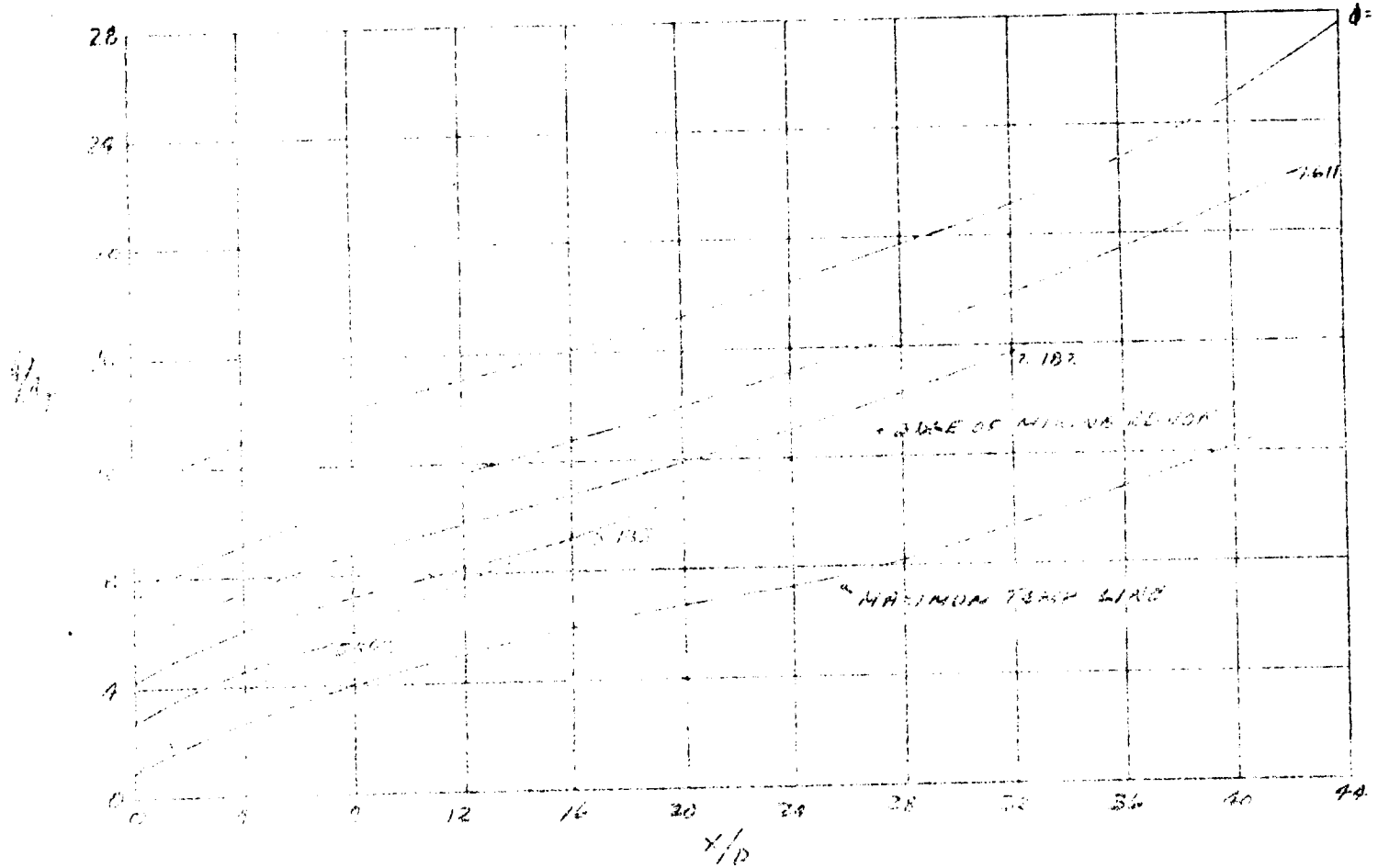

Page 174 of 175

FIG 9a' RADIAL PROFILE OF VELOCITY, TEMPERATURE, AND SOUND SPEED AT X/D=20.
TWO DIMENSIONAL, PRESSURE DROP
$M_\infty = 6.$, $M_B = 2.$, ALTITUDE = 90,000 FEET

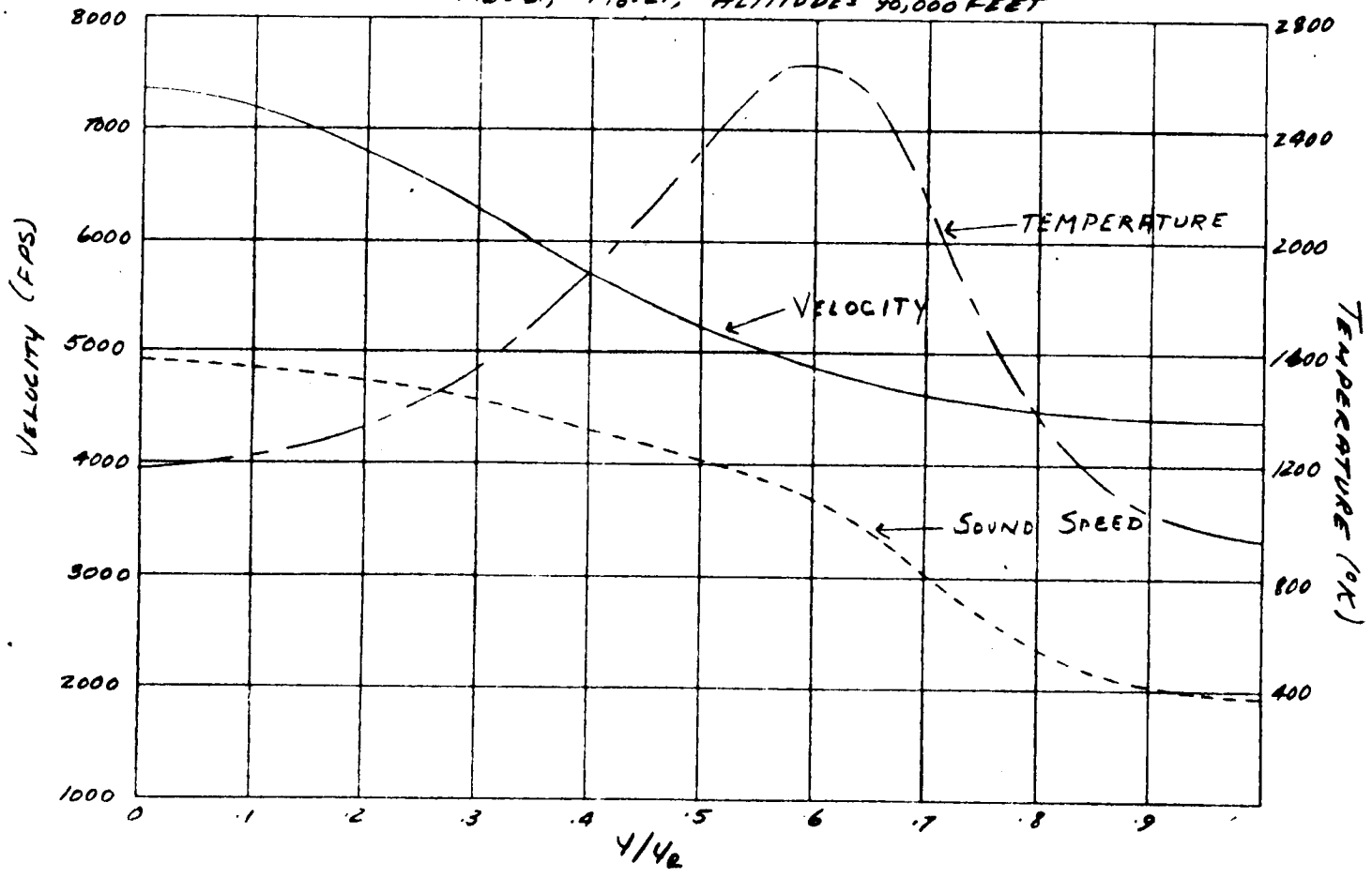

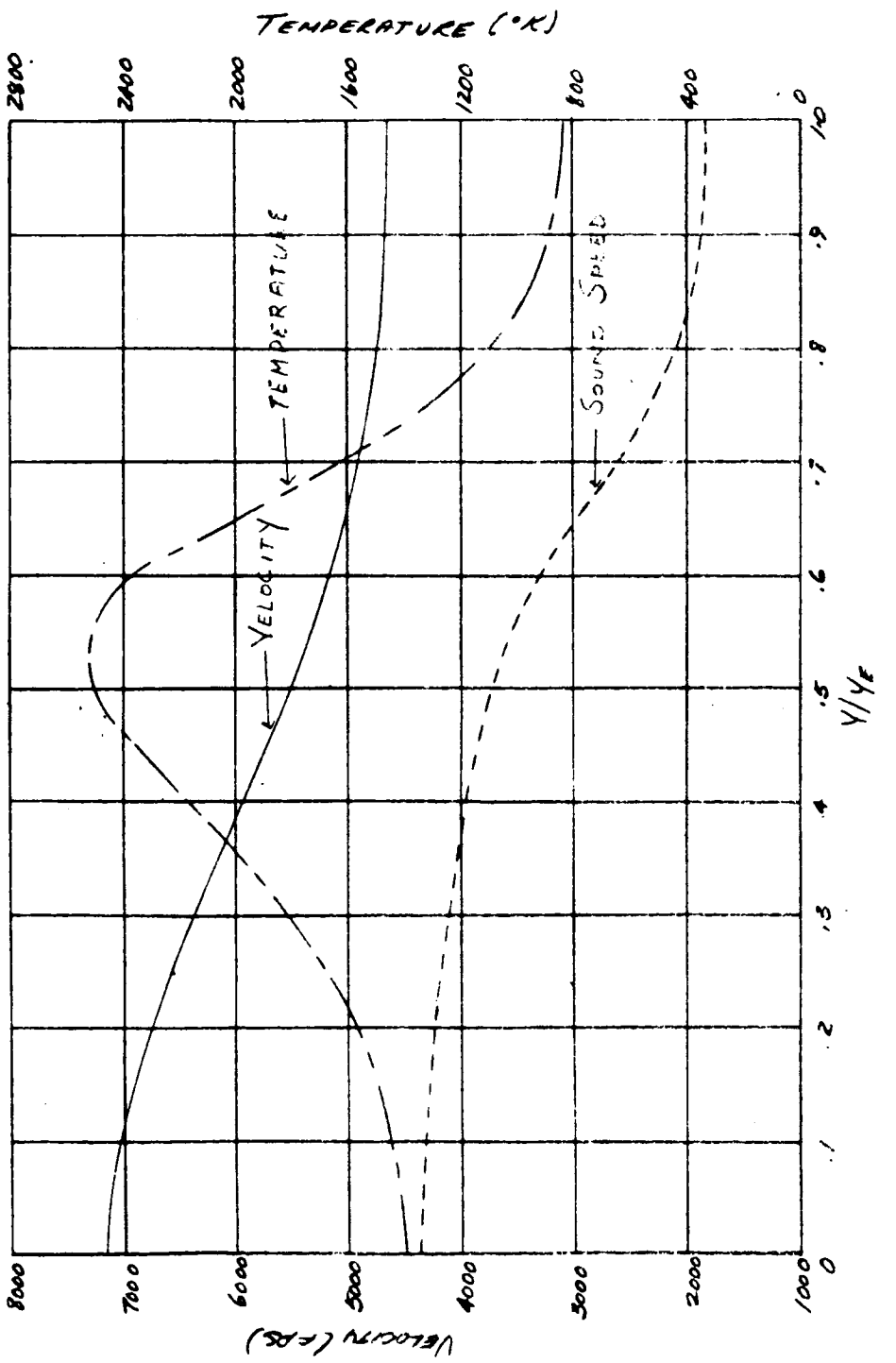

FIG 9a" RADIAL PROFILES OF VELOCITY, TEMPERATURE, AND SOUND SPEED AT X/D = 40.
TWO DIMENSIONAL, PRESSURE DROP
$M_\infty = 6.$, $M_B = 2.$, ALTITUDE- 90,000 FEET

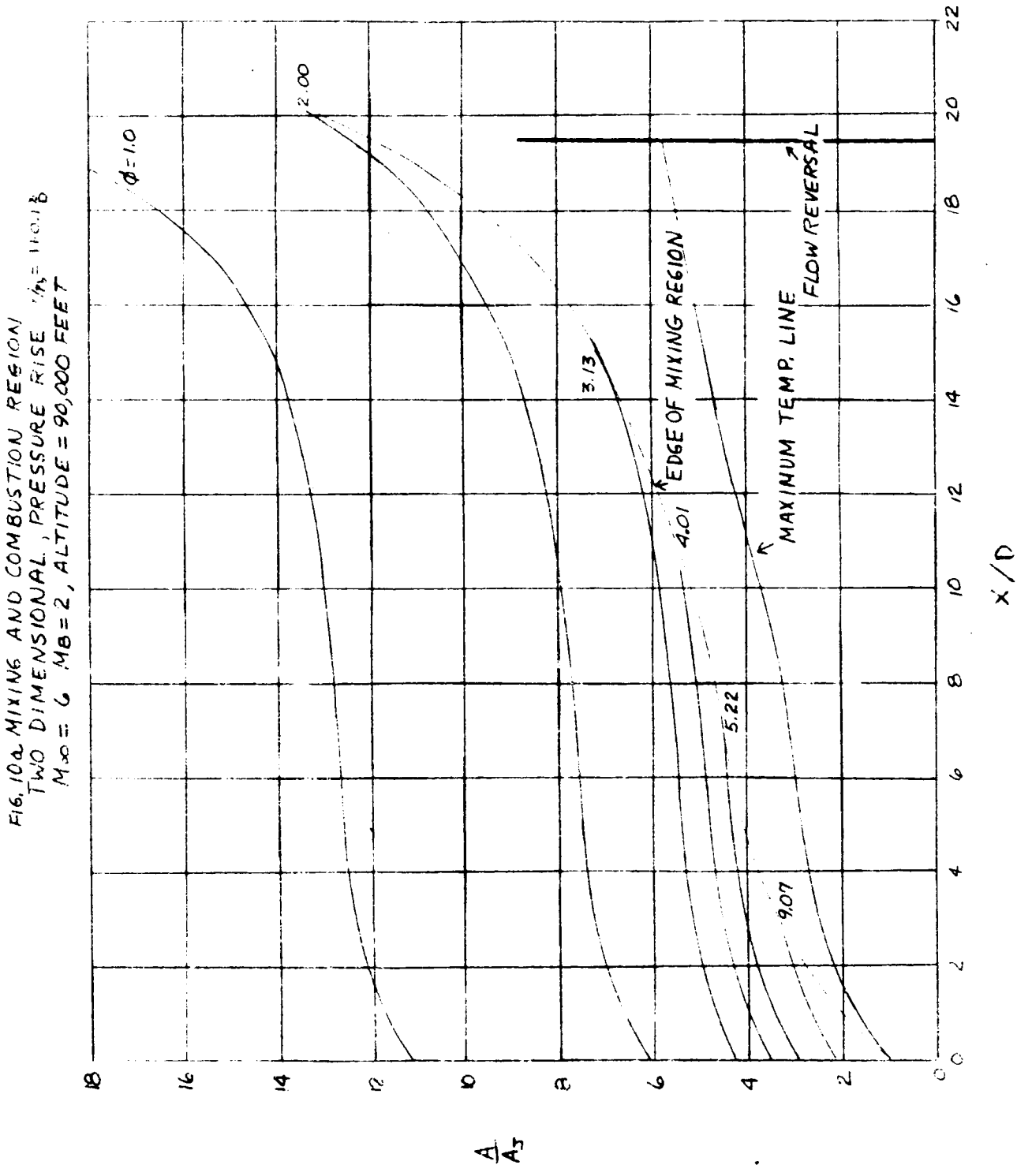
FIG. 10a MIXING AND COMBUSTION REGION
TWO DIMENSIONAL, PRESSURE RISE
M∞ = 6, MB = 2, ALTITUDE = 90,000 FEET
Φ = 1.0
2.00
3.13
4.01
5.22
9.07
EDGE OF MIXING REGION
MAXIMUM TEMP. LINE
FLOW REVERSAL
A/A*
X/D
0
2
4
6
8
10
12
14
16
18
20
22

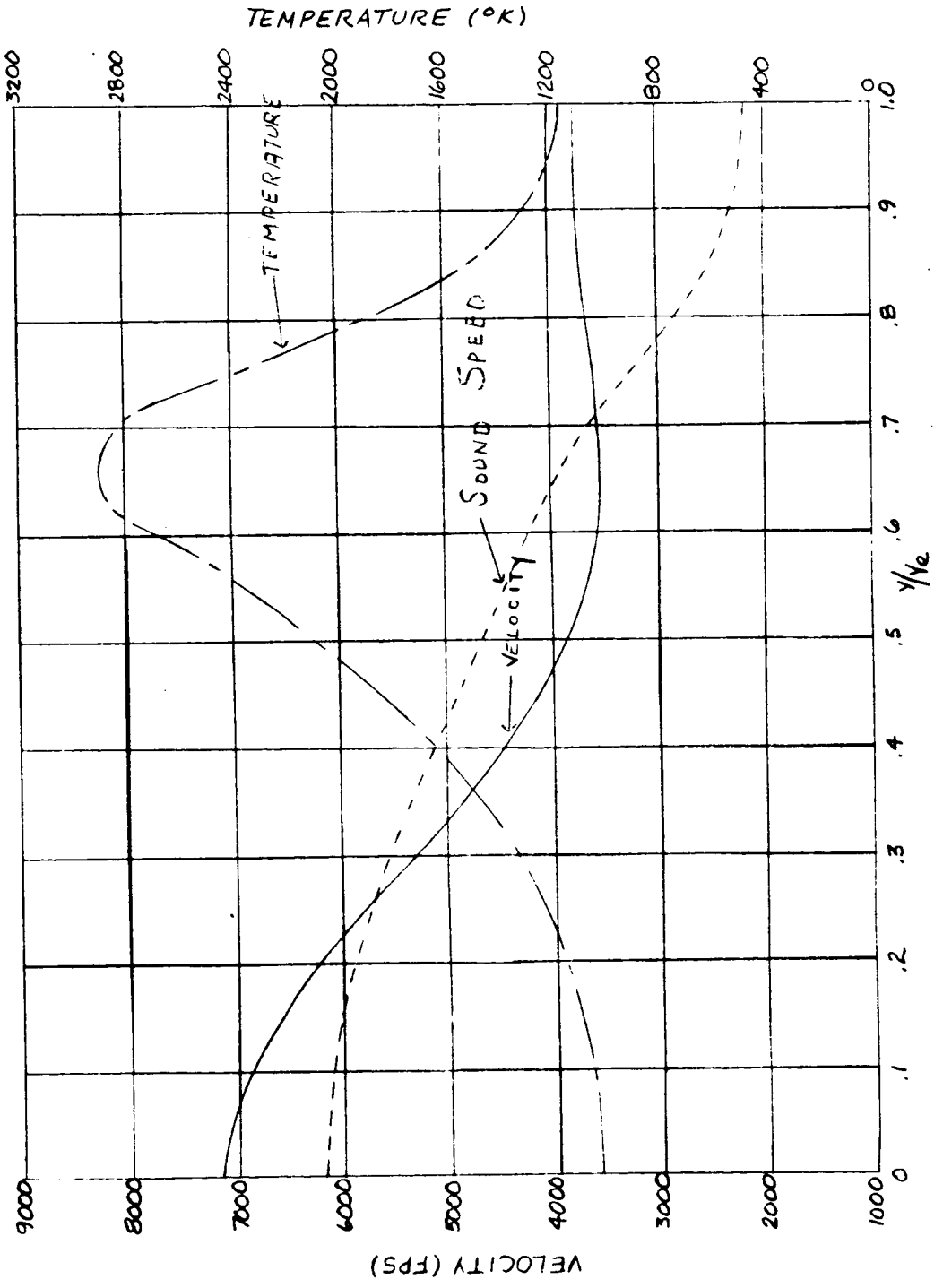

FIG. 10a' RADIAL PROFILES OF VELOCITY, TEMPERATURE, AND SOUND SPEED AT $\frac{X}{D} = 7$
TWO DIMENSIONAL, PRESSURE RISE
$M_\infty = 6$ $M_B = 2$, ALTITUDE = 90,000 FEET

FIG. 10a" RADIAL PROFILES OF VELOCITY, TEMPERATURE, AND SOUND SPEED AT $\frac{X}{b} = 15$
TWO DIMENSIONAL, PRESSURE RISE
$M_\infty = 6$ $M_B = 2$, ALTITUDE = 90,000 FEET

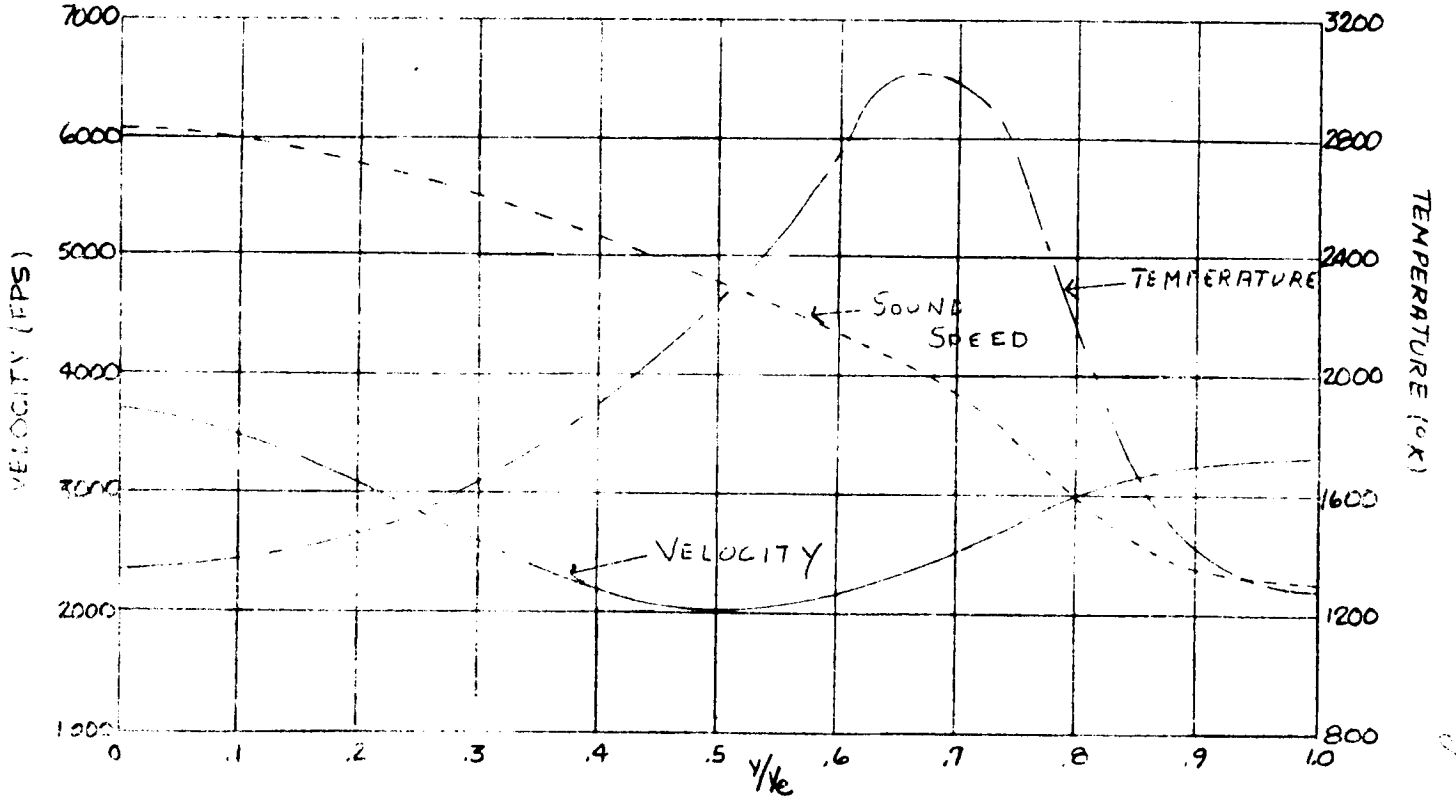

TR 569
Page 21

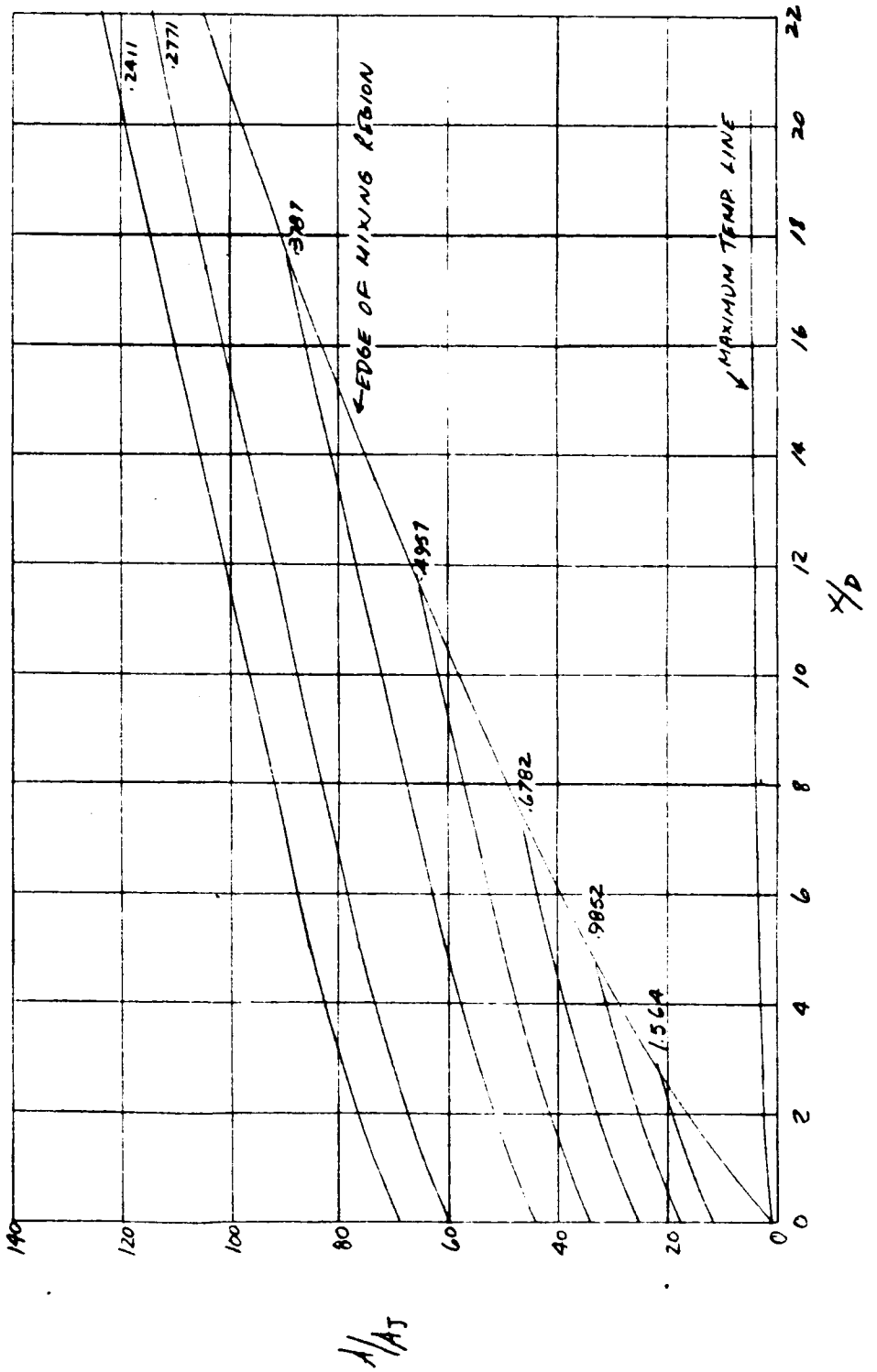

FIG. 11a MIXING AND COMBUSTION REGION
AXISYMMETRIC, CONSTANT PRESSURE
$M_o = 3.$, $M_B = 1.$, ALTITUDE = 50,000 FEET

FIG 11a' RADIAL PROFILES OF VELOCITY, TEMPERATURE, AND SOUND SPEED AT $x/D = 20$

AXISYMMETRIC, CONSTANT PRESSURE

$M_\infty = 3$ $M_B = 1$ ALTITUDE = 50,000 FEET

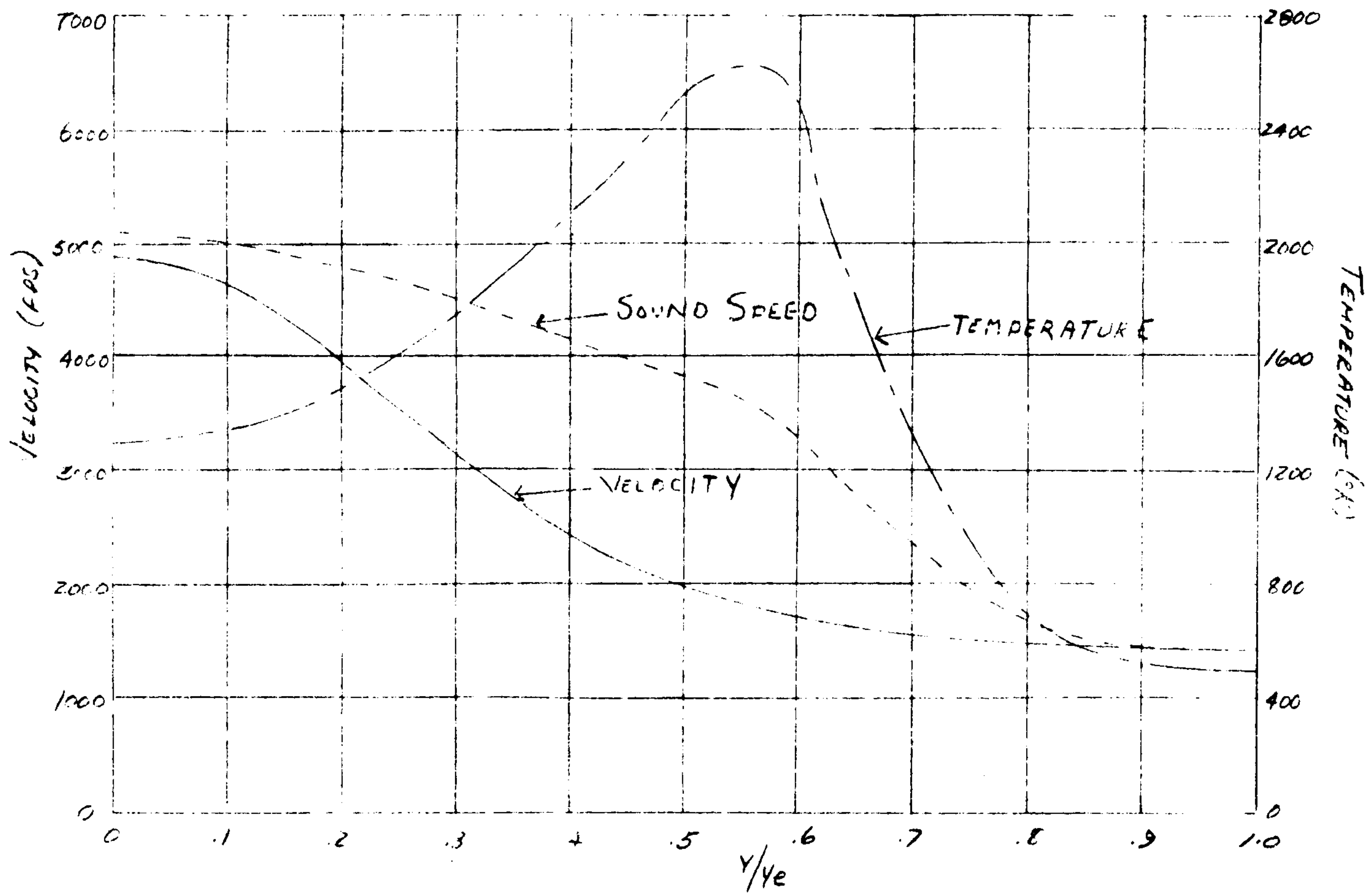

FIG. 11a" RADIAL PROFILES OF VELOCITY, TEMPERATURE, AND SOUND SPEED AT X/D = 40.
AXISYMMETRIC, CONSTANT PRESSURE
$M_\infty = 3$, $M_B = 1$, ALTITUDE: 50,000 FEET

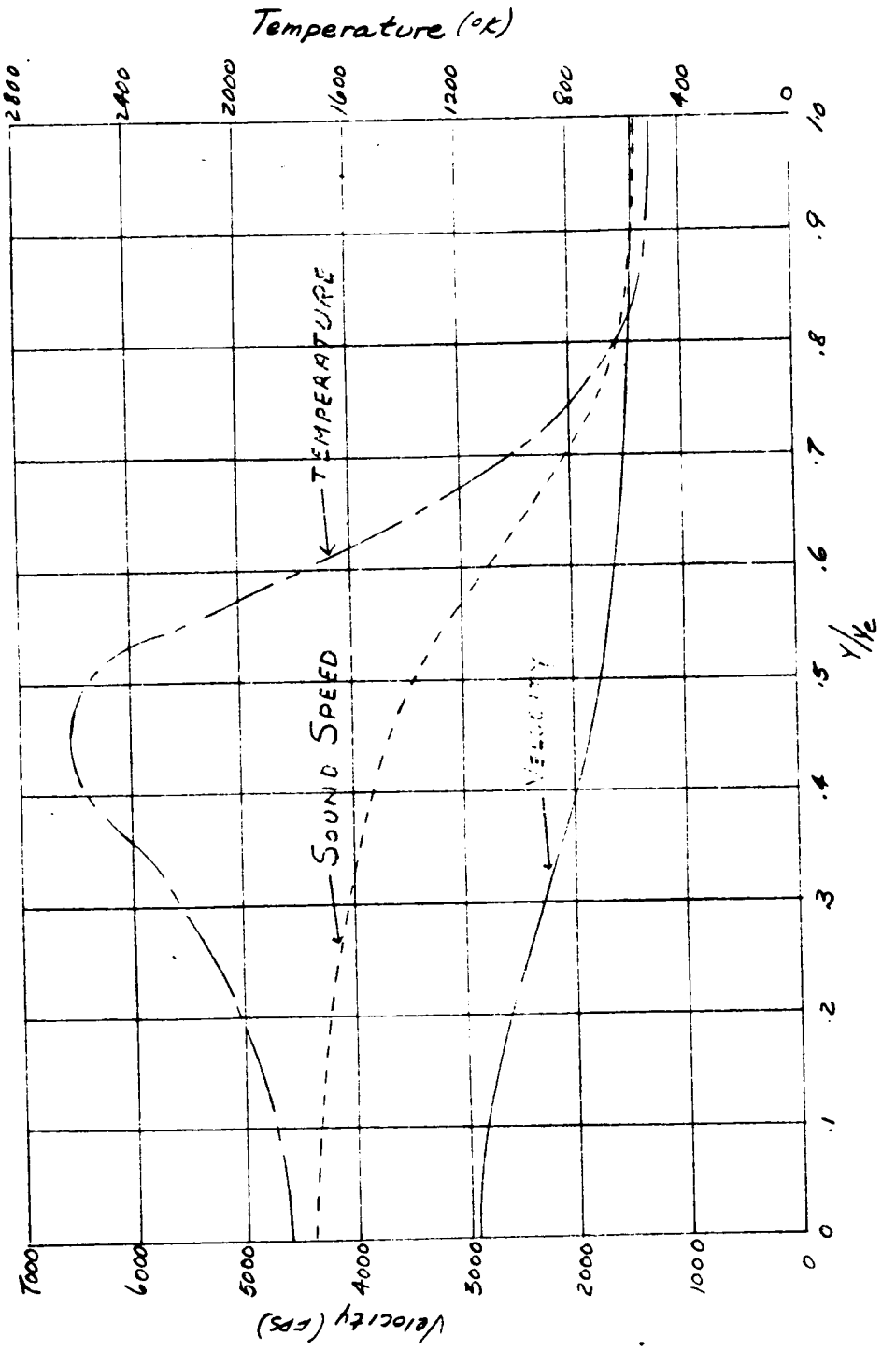

FIG II.6 MIXING AND COMBUSTION REGION

AXISYMMETRIC, CONSTANT PRESSURE

$M_\infty = 3$, $M_B = 1$ ALTITUDE = 65,000 FEET

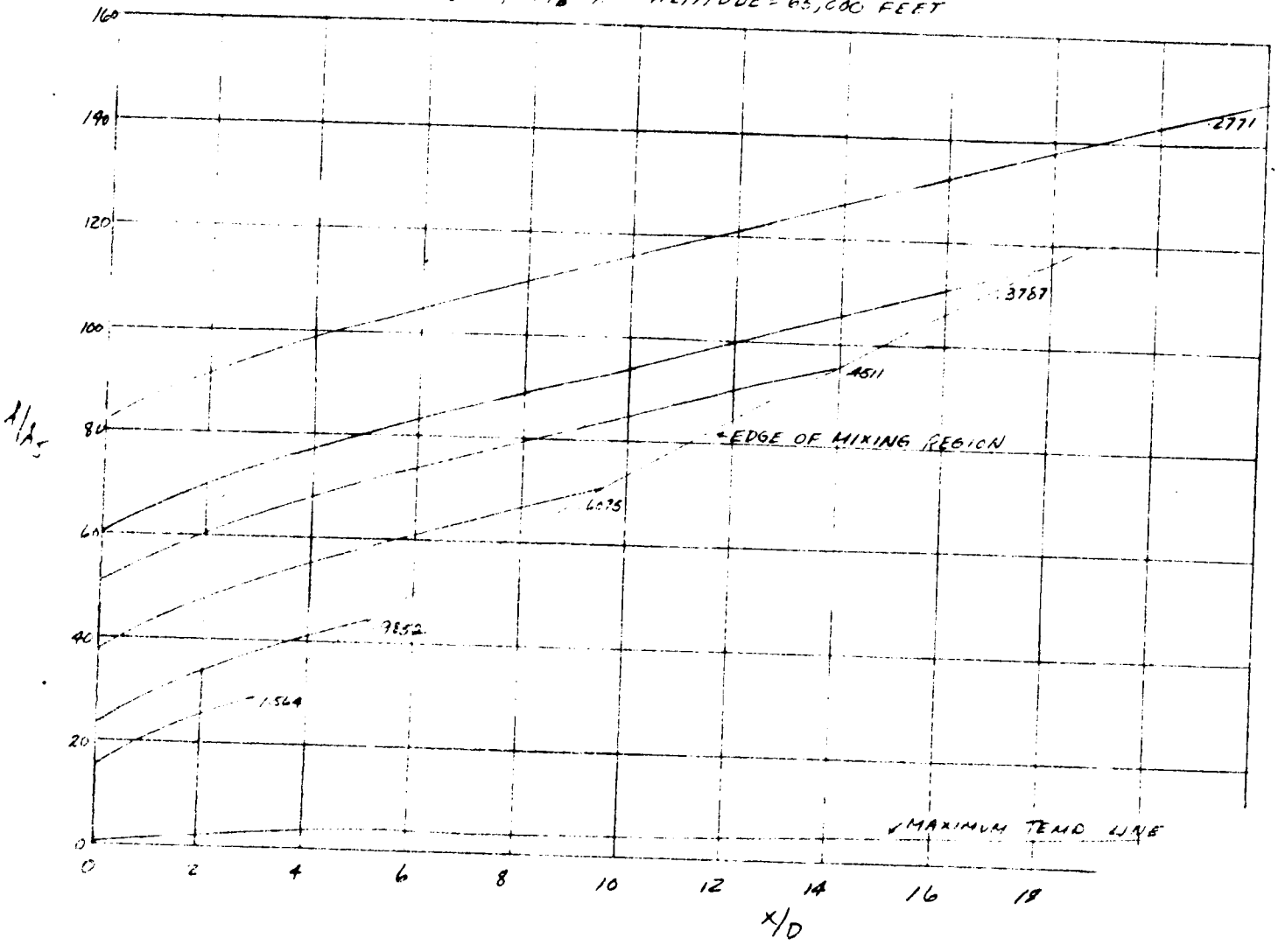

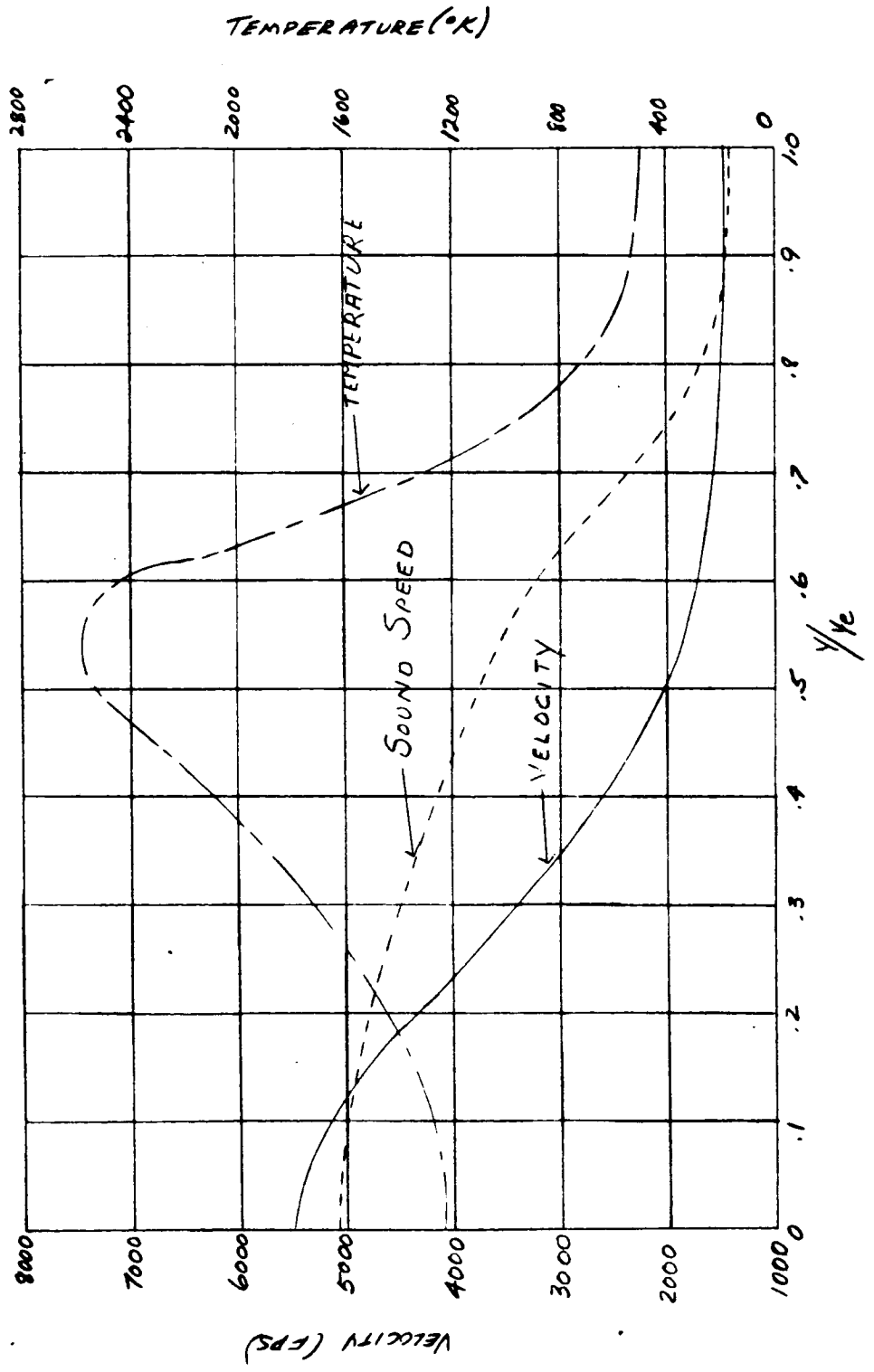

FIG. 116' RADIAL PROFILES OF VELOCITY, TEMPERATURE, AND SOUND SPEED AT X/D = 20.
AXISYMMETRIC, CONSTANT PRESSURE
$M_0 = 3.$, $M_0 = 1.$, ALTITUDE = 65,000 FEET

FIG 11 6" RADIAL PROFILES OF VELOCITY, TEMPERATURE, AND SOUND SPEED AT $x/D = 40$.

AXISYMMETRIC, CONSTANT PRESSURE

$M_\infty = 3.$, $M_\theta = 1.$, ALTITUDE = 65,000 FEET

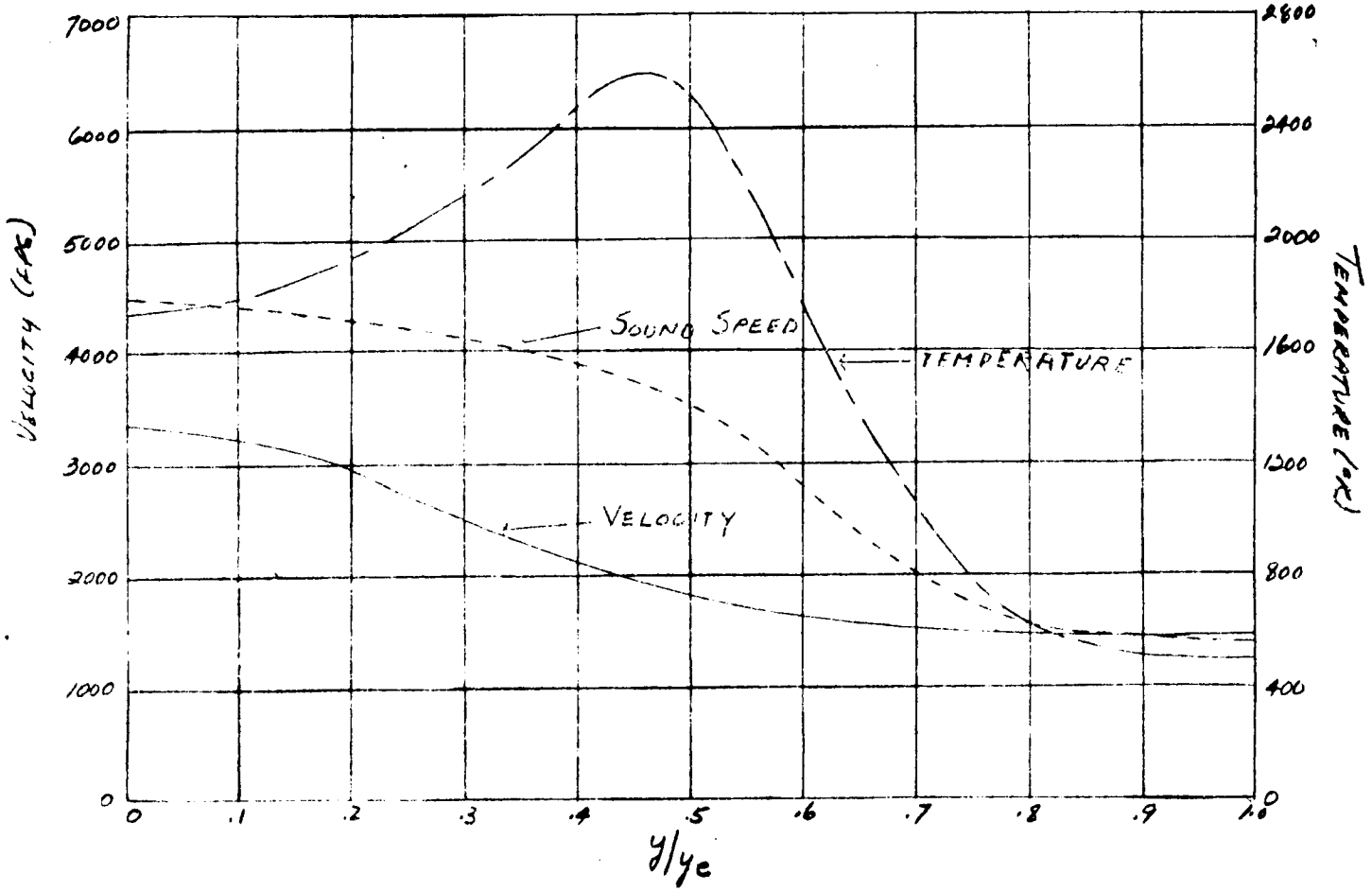

TR 562
Page 27

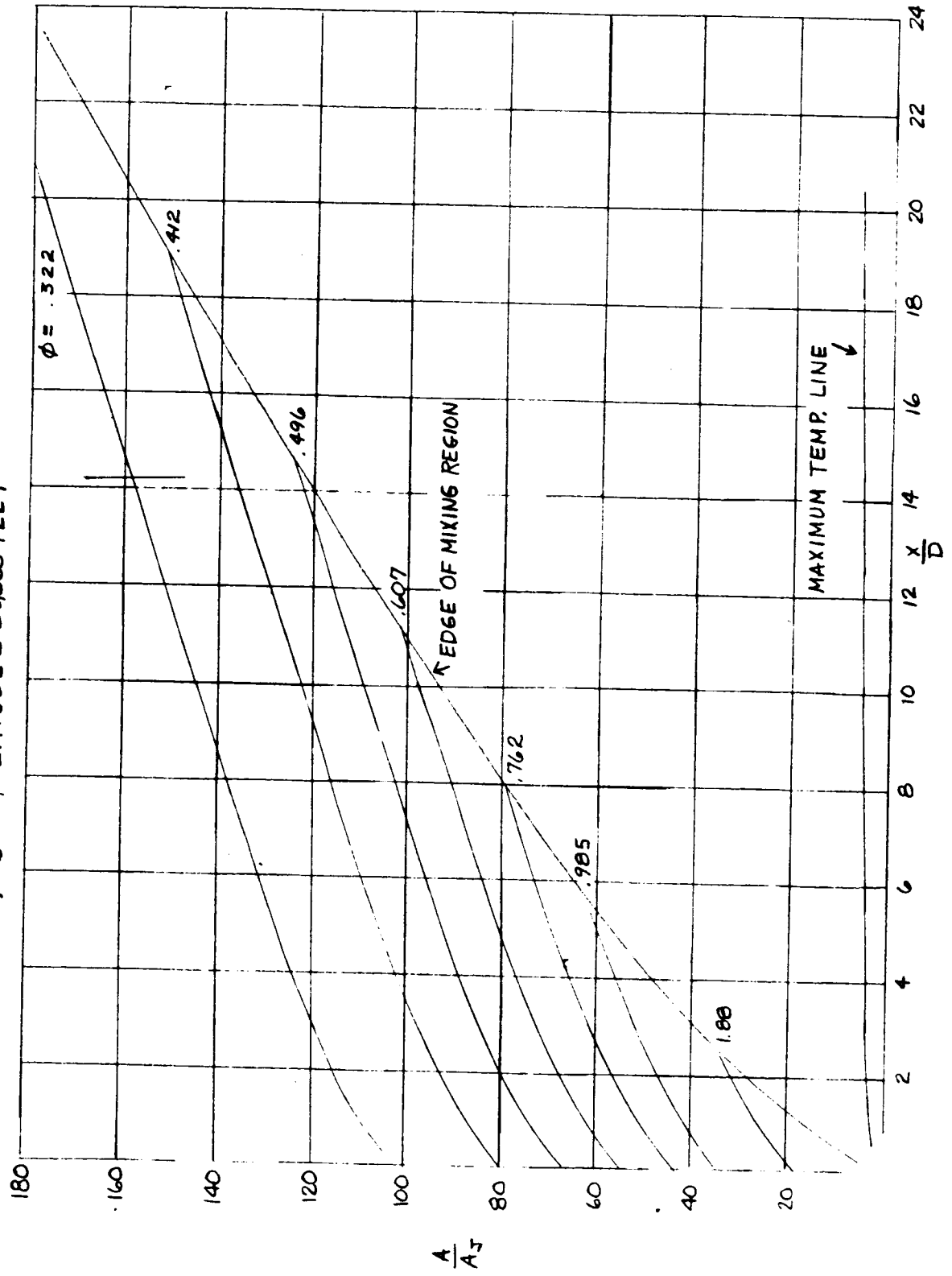

FIG. 11c MIXING AND COMBUSTION REGION
AXISYMMETRIC, CONSTANT PRESSURE
$M_0 = 3$, $M_B = 1$, ALTITUDE = 85,000 FEET

FIG. 11c' RADIAL PROFILES OF VELOCITY, TEMPERATURE, AND SOUND SPEED AT $\frac{X}{D} = 10$
AXISYMMETRIC, CONSTANT PRESSURE
$M_\infty = 3$, $M_B = 1$, ALTITUDE = 85,000 FEET

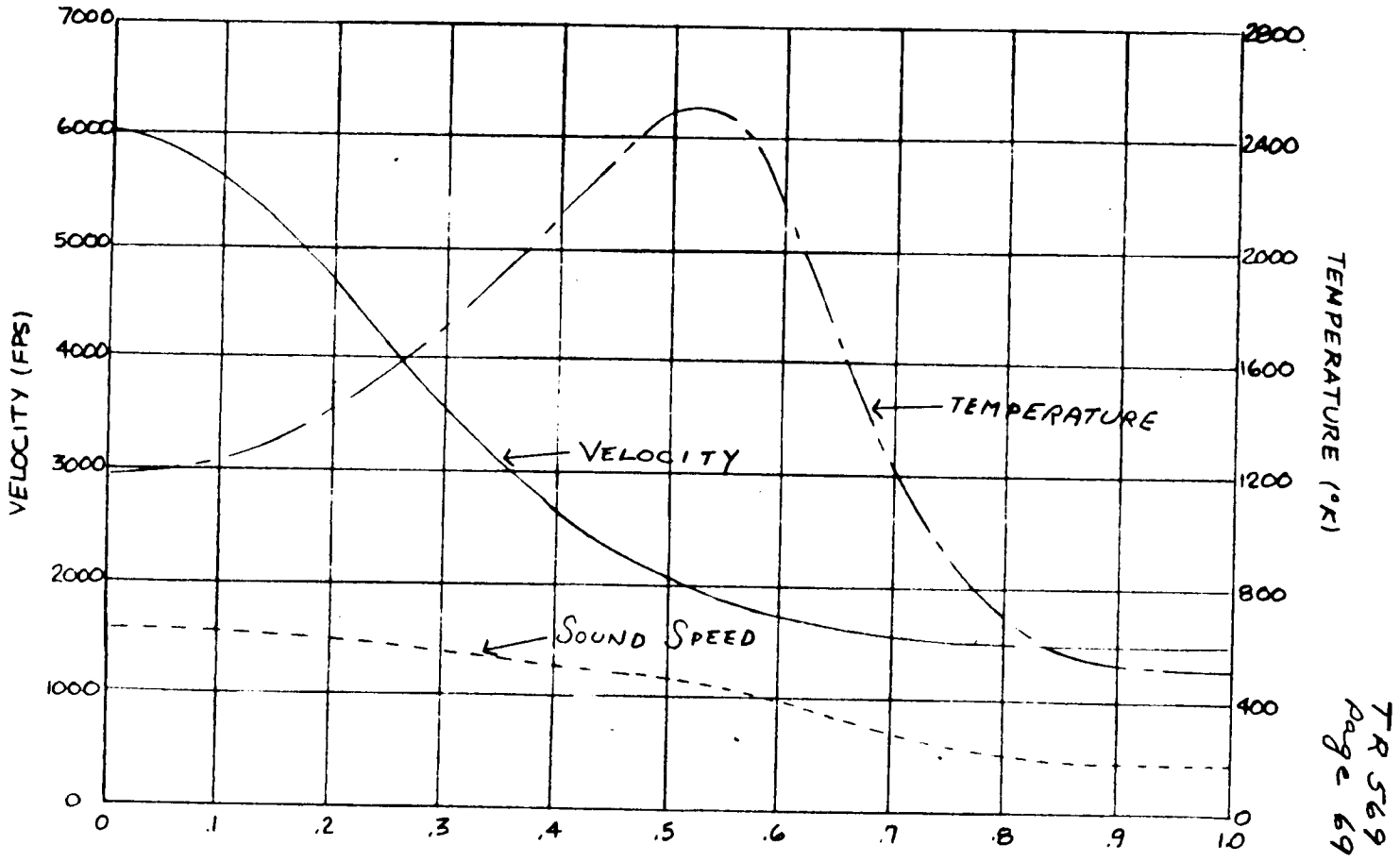

TR 569
Page 69

FIG. 11c" RADIAL PROFILES OF VELOCITY, TEMPERATURE, AND SOUND SPEED AT $\frac{x}{D} = 20$
AXISYMMETRIC, CONSTANT PRESSURE
$M_\infty = 3$, $M_B = 1$, ALTITUDE = 85,000 FEET

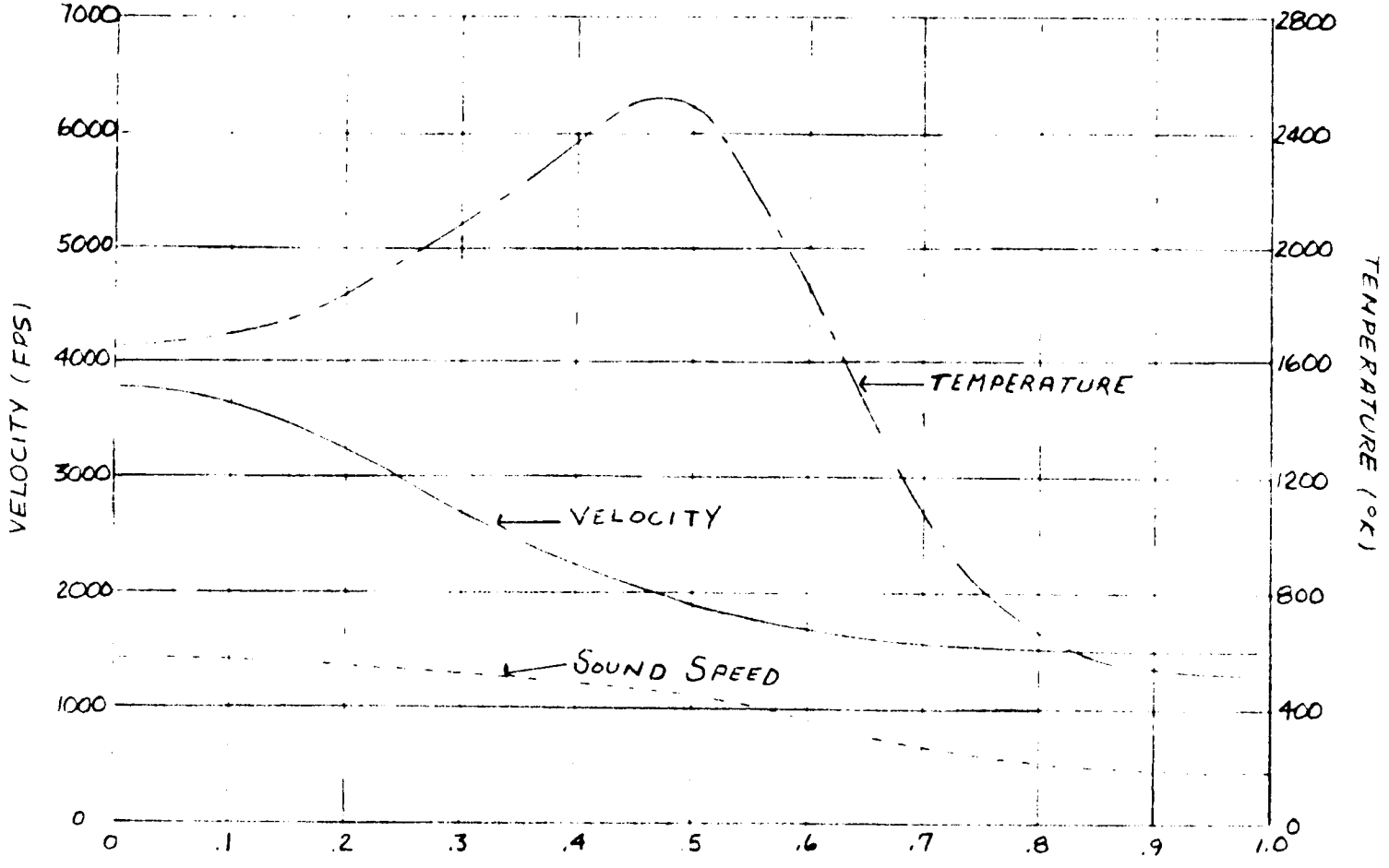

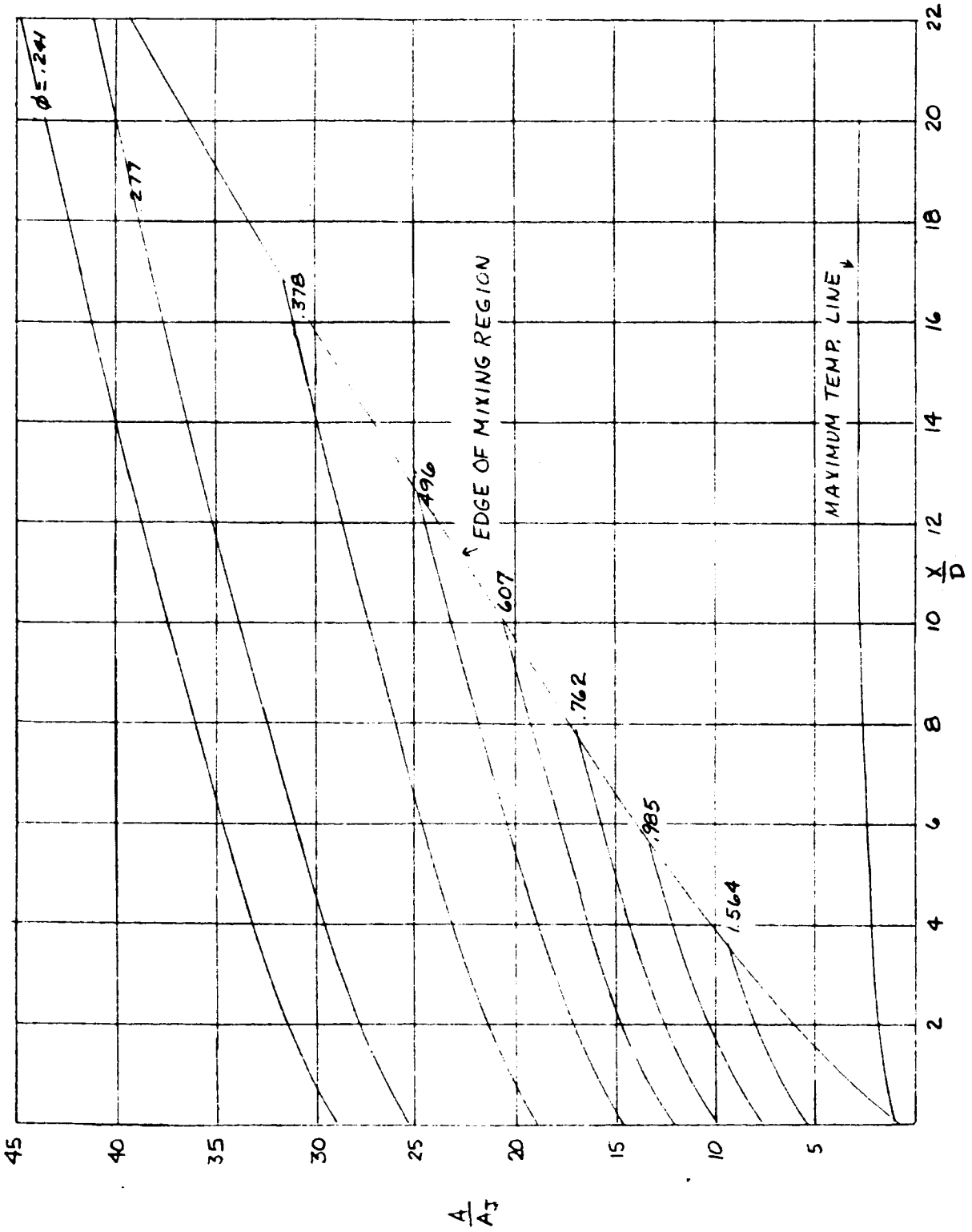

FIG. IId MIXING AND COMBUSTION REGION
AXISYMMETRIC, CONSTANT PRESSURE
$M_\infty = 6$, $M_B = 2$, ALTITUDE = 75,000 FEET

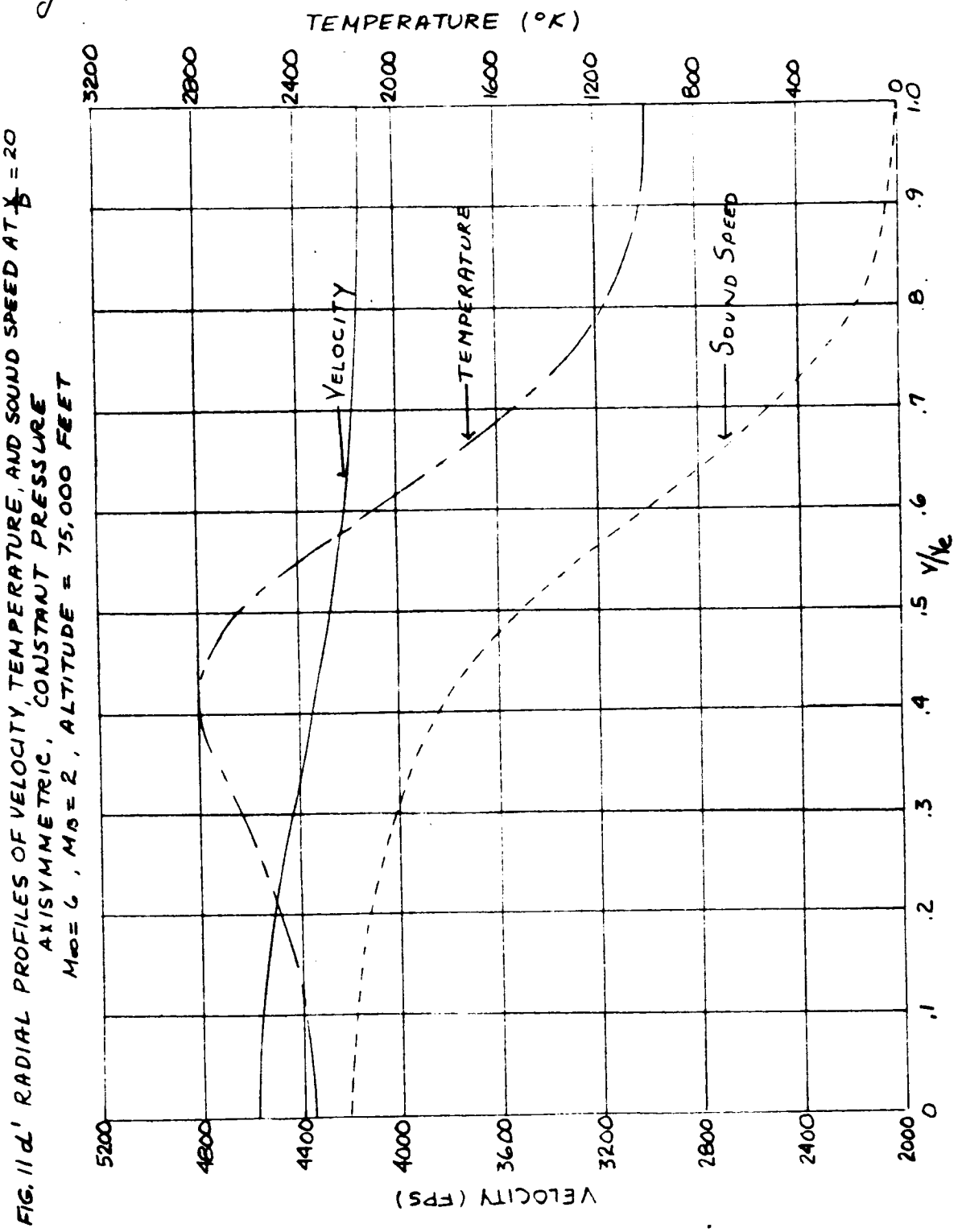

FIG. 11 d' RADIAL PROFILES OF VELOCITY, TEMPERATURE, AND SOUND SPEED AT $\frac{X}{D} = 20$
AXISYMMETRIC, CONSTANT PRESSURE
$M_{\infty} = 6$, $M_S = 2$, ALTITUDE = 75,000 FEET

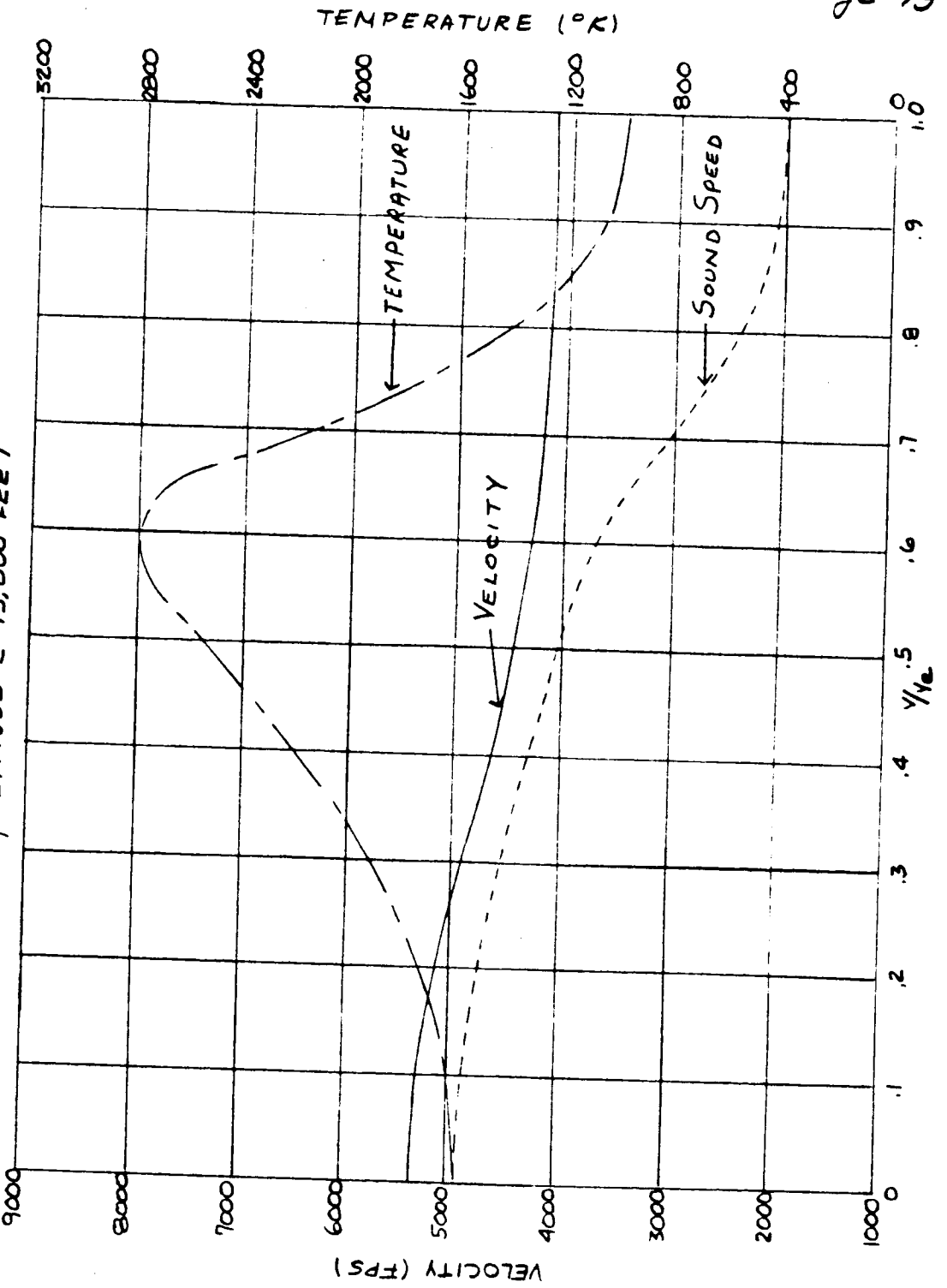

FIG. 11d" RADIAL PROFILES OF VELOCITY, TEMPERATURE, AND SOUND SPEED AT $\frac{X}{D} = 10$
AXISYMMETRIC, CONSTANT PRESSURE
$M_\infty = 6$ $M_a = 2$, ALTITUDE = 75,000 FEET

Fig. 11e Mixing and Combustion Region

Axisymmetric, Constant Pressure

$M_\infty = 6.$, $M_B = 2$, Altitude = 90 000 feet

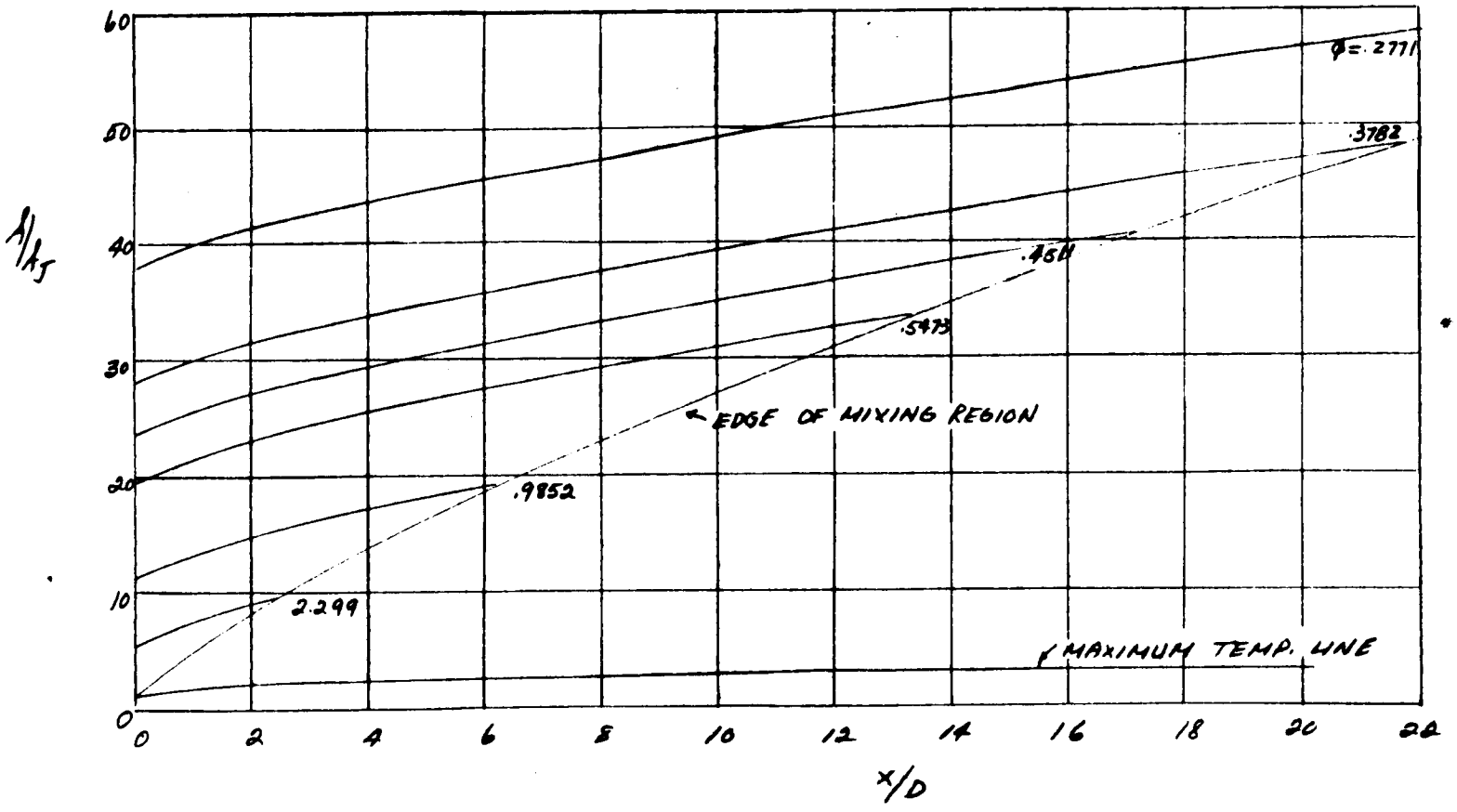

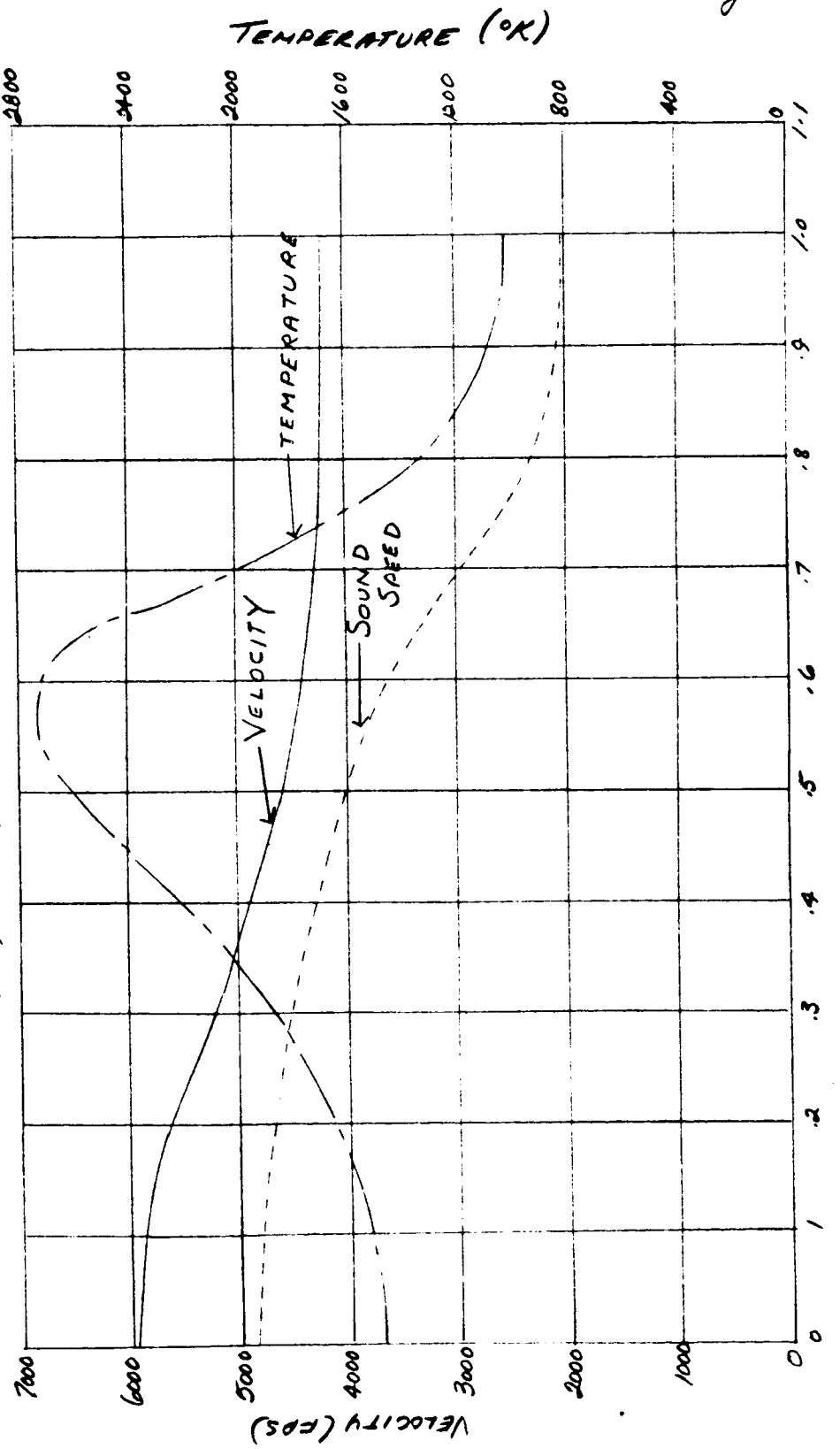

FIG 11e' RADIAL PROFILES OF VELOCITY, TEMPERATURE, AND SOUND SPEED AT X/D = 10.
AXISYMMETRIC, CONSTANT PRESSURE
$M_\infty = 6.$, $M_B = 2.$, ALTITUDE = 90,000 FEET

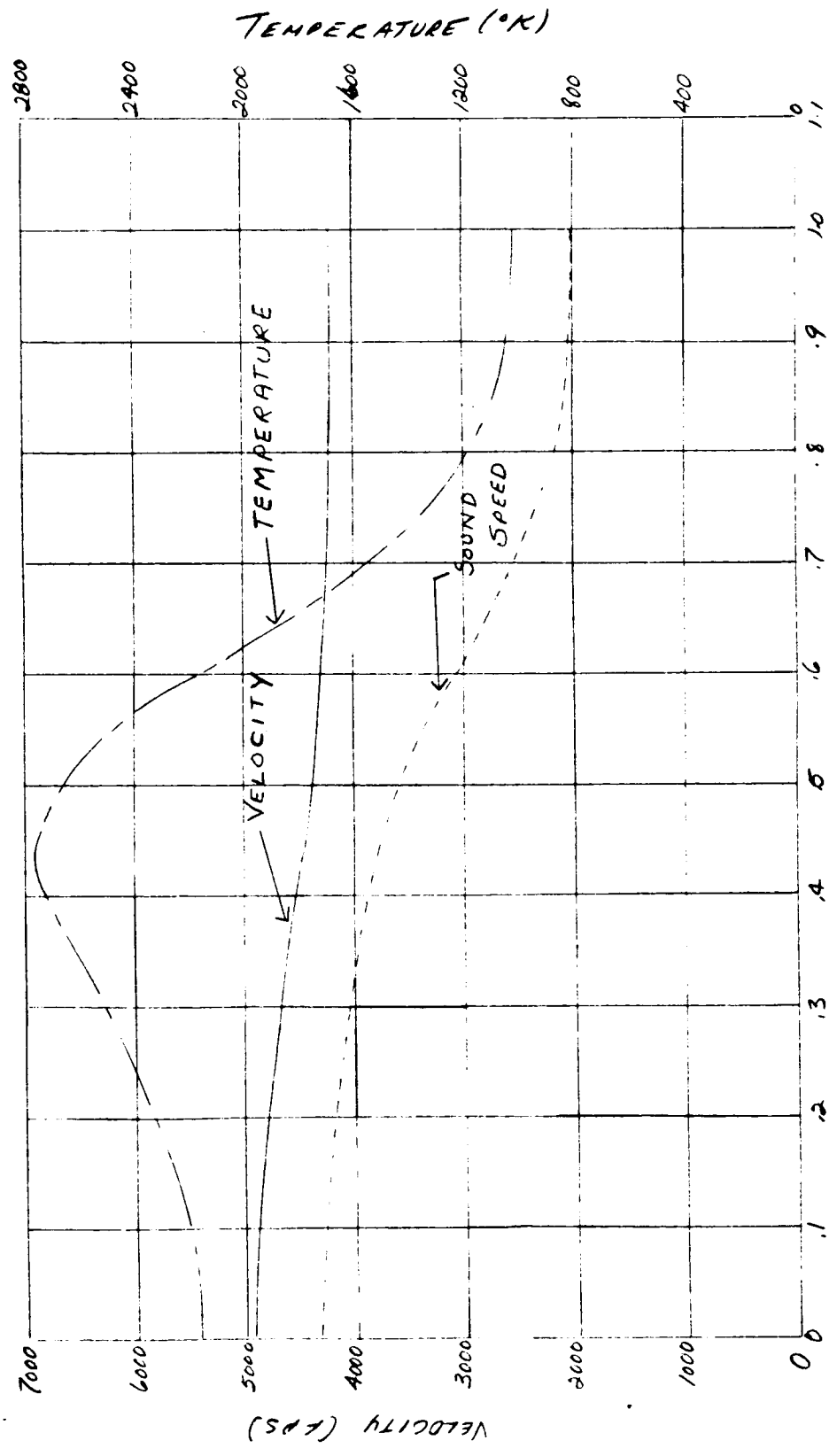

FIG. 11a" RADIAL PROFILES OF VELOCITY, TEMPERATURE, AND SOUND SPEED AT x/D=20. AXISYMMETRIC, CONSTANT PRESSURE $M_\infty = 6.$, $M_B = 2.$ ALTITUDE= 90000 FEET

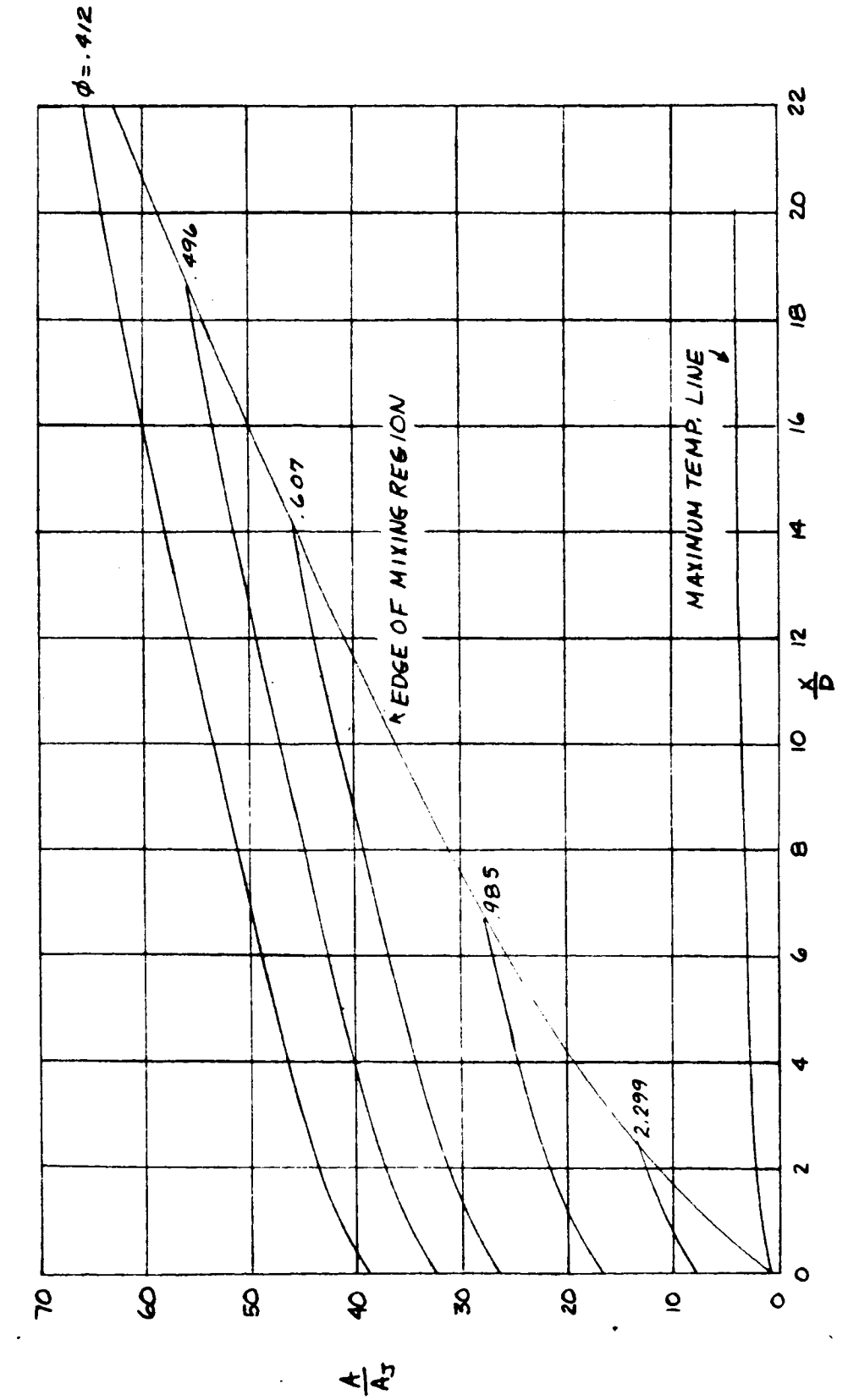

FIG. 11f MIXING AND COMBUSTION REGION
AXISYMMETRIC, COUSTANT PRESSURE
$M_\infty = 6$ $M_B = 2$, ALTITUDE = 110,000 FEET

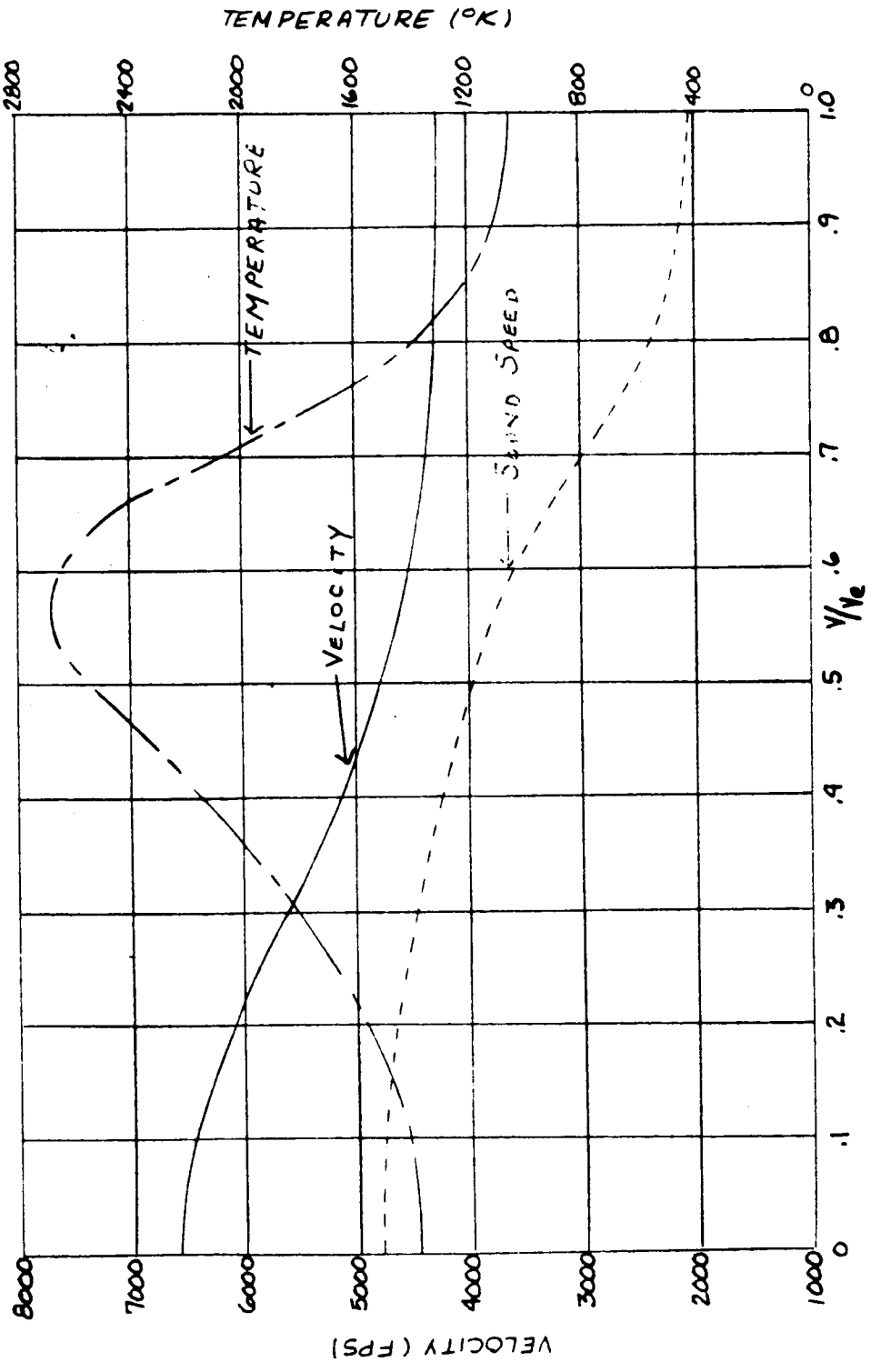

FIG. 114' RADIAL PROFILES OF VELOCITY, TEMPERATURE, AND SOUND SPEED AT $\frac{X}{D} = 10$
AXISYMMETRIC, CONSTANT PRESSURE
$M_\infty = 6$ $M_B = 2$, ALTITUDE = 110,000 FEET

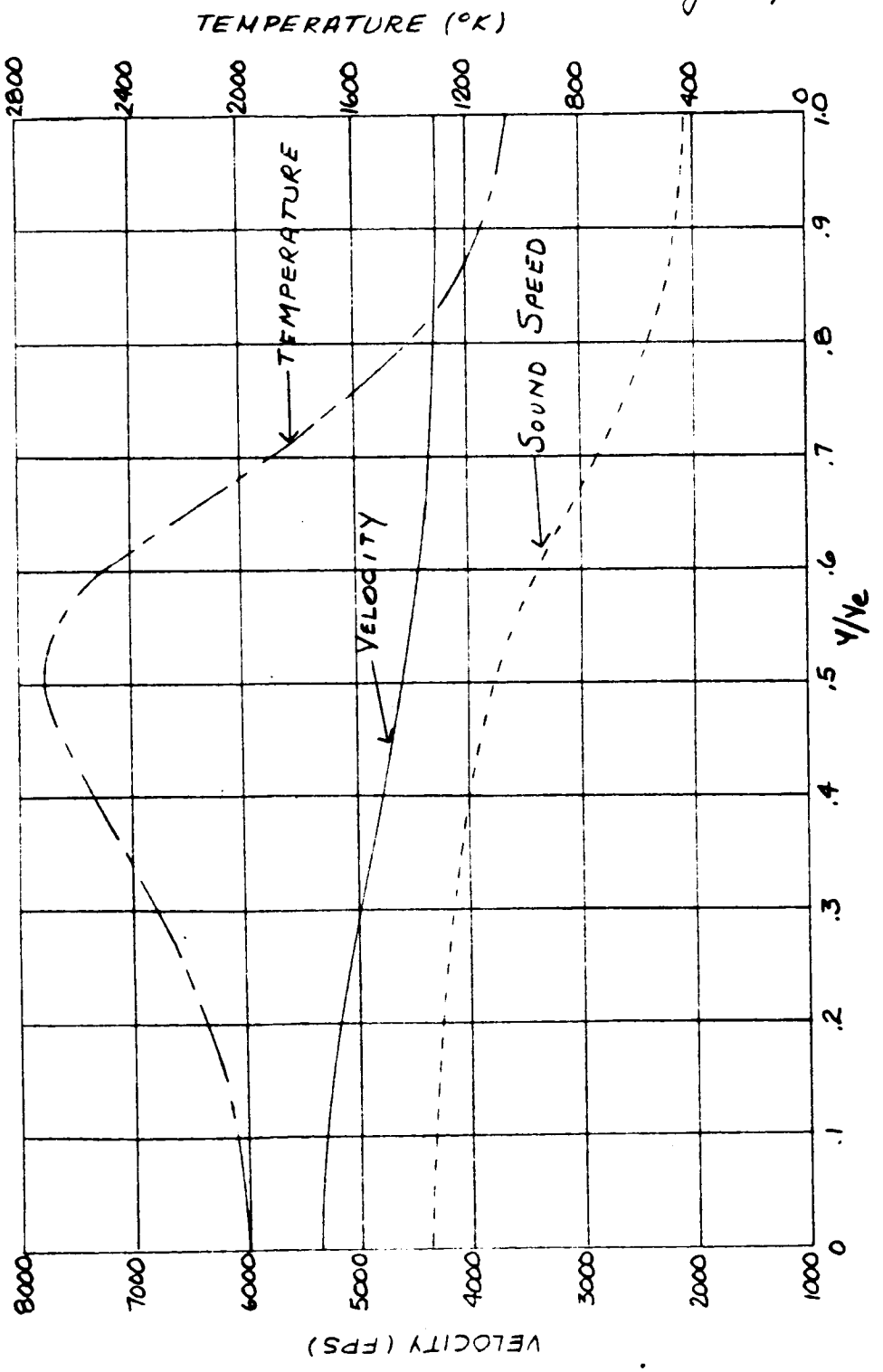

FIG. 114" RADIAL PROFILES OF VELOCITY, TEMPERATURE, AND SOUND SPEED AT $\frac{X}{D} = 20$
AXISYMMETRIC, CONSTANT PRESSURE
$M_\infty = 6$, $M_0 = 2$, ALTITUDE = 110,000 FEET

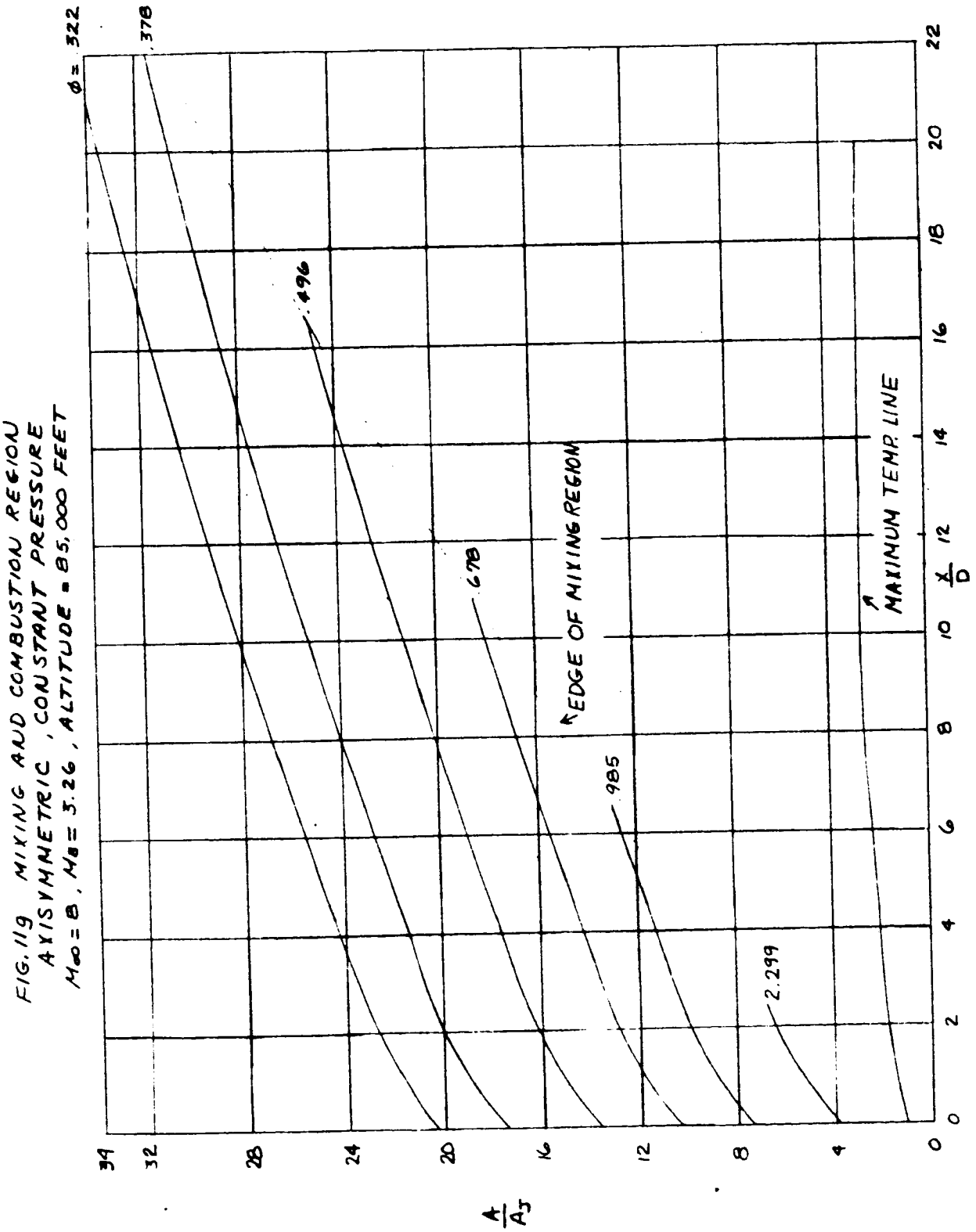

FIG. 119 MIXING AND COMBUSTION REGION
AXISYMMETRIC, CONSTANT PRESSURE
$M_\infty = 8$, $M_B = 3.26$, ALTITUDE = 85,000 FEET

Fig. 11g' RADIAL PROFILES OF VELOCITY, TEMPERATURE, AND SOUND SPEED AT $\frac{X}{D} = 10$
AXISYMMETRIC, CONSTANT PRESSURE
$M_\infty = 8$, $M_B = 3.26$, ALTITUDE = 85,000 FEET

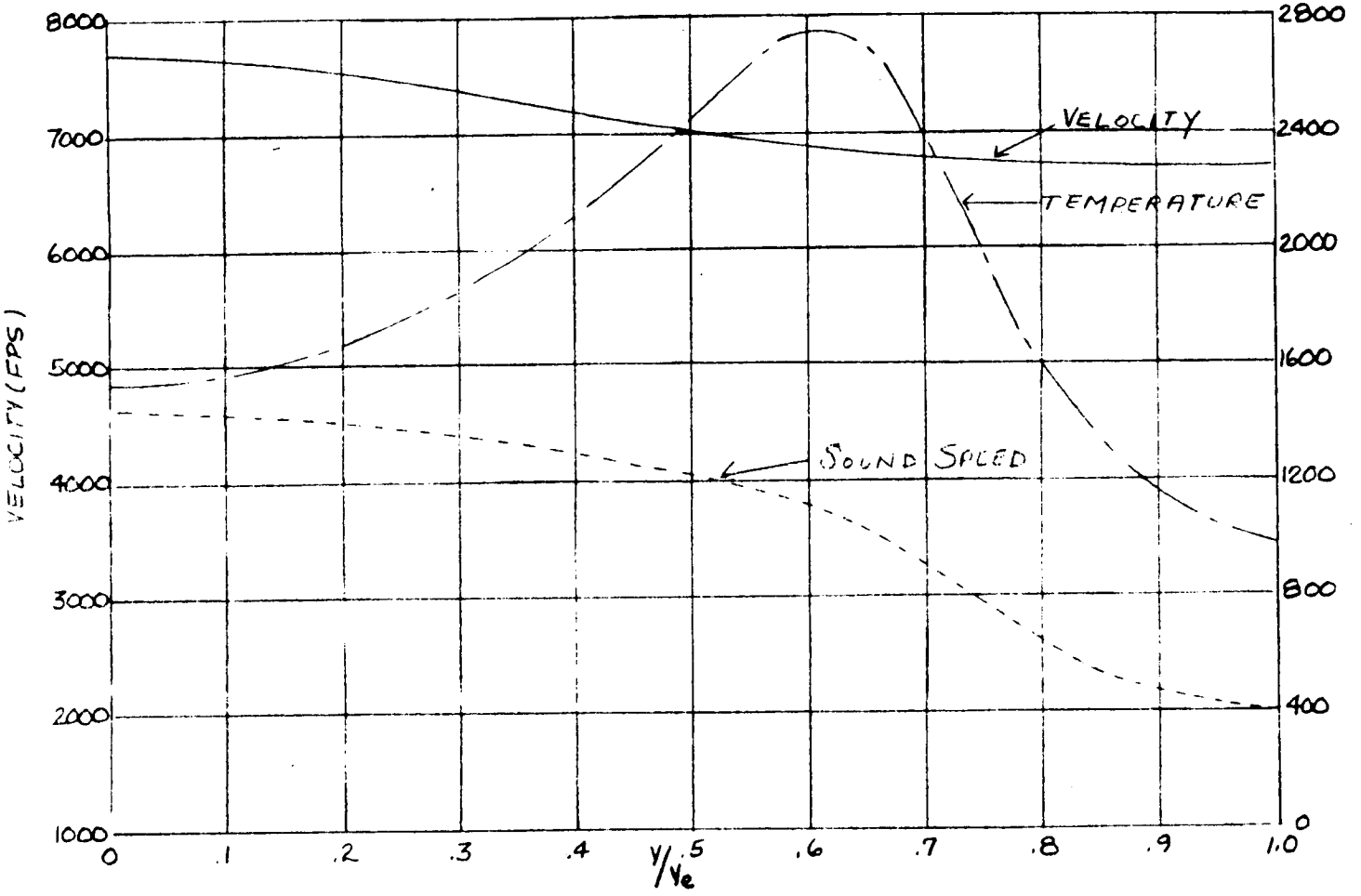

TR 569
Page 81

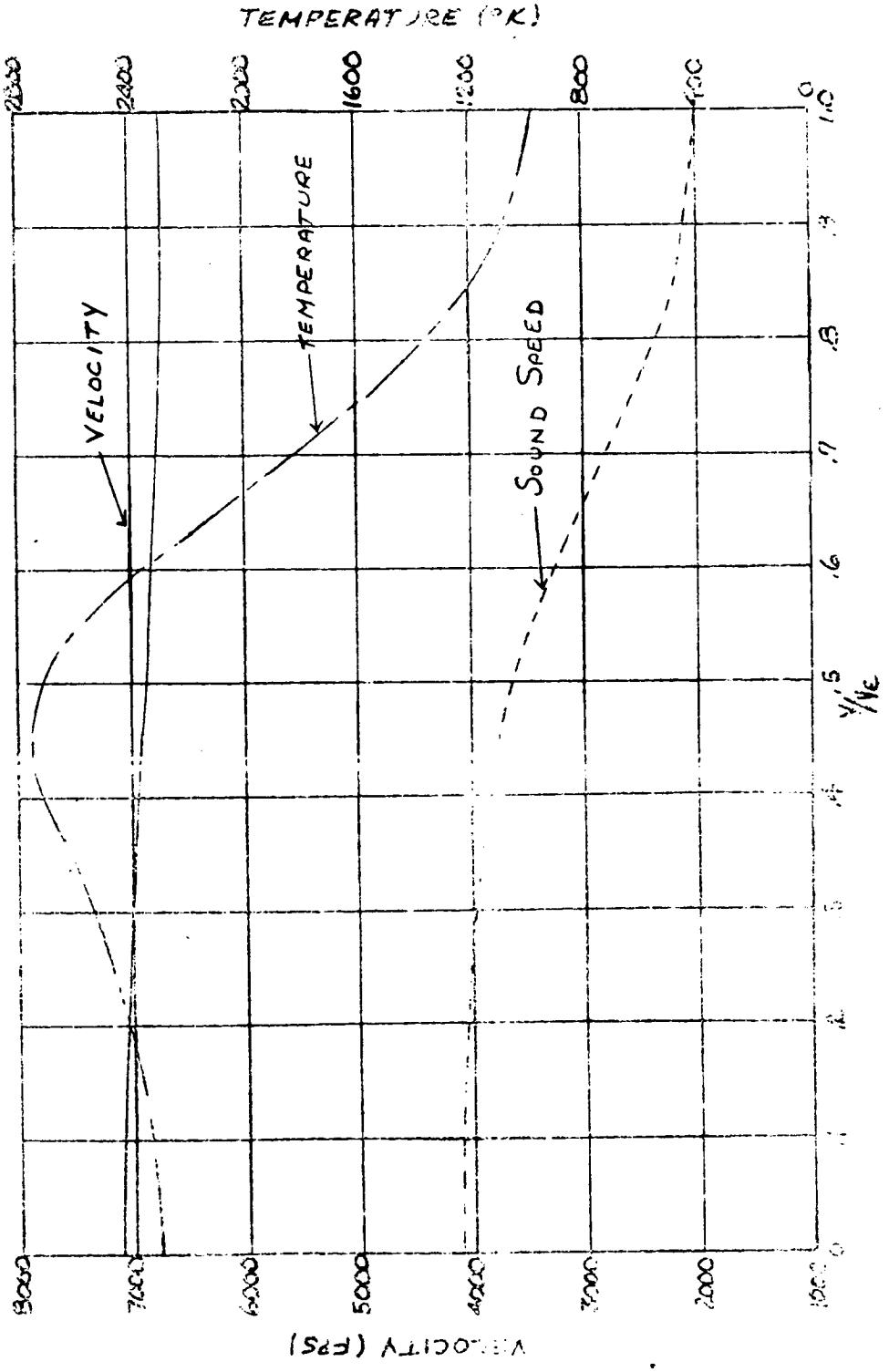

FIG. II-6 RADIAL PROFILES OF VELOCITY, TEMPERATURE, AND SOUND SPEED AT $\frac{x}{D} = 20$
AXISYMMETRIC, CONSTANT PRESSURE
$M_{\infty} = 8$, $N_{Re} = 3.26$, ALTITUDE = 86,000 FEET

Fig. 11h MIXING AND COMBUSTION REGION
AXISYMMETRIC, CONSTANT PRESSURE
$M_\infty = 8.$, $M_B = 3.26$, ALTITUDE = 100,000 FT

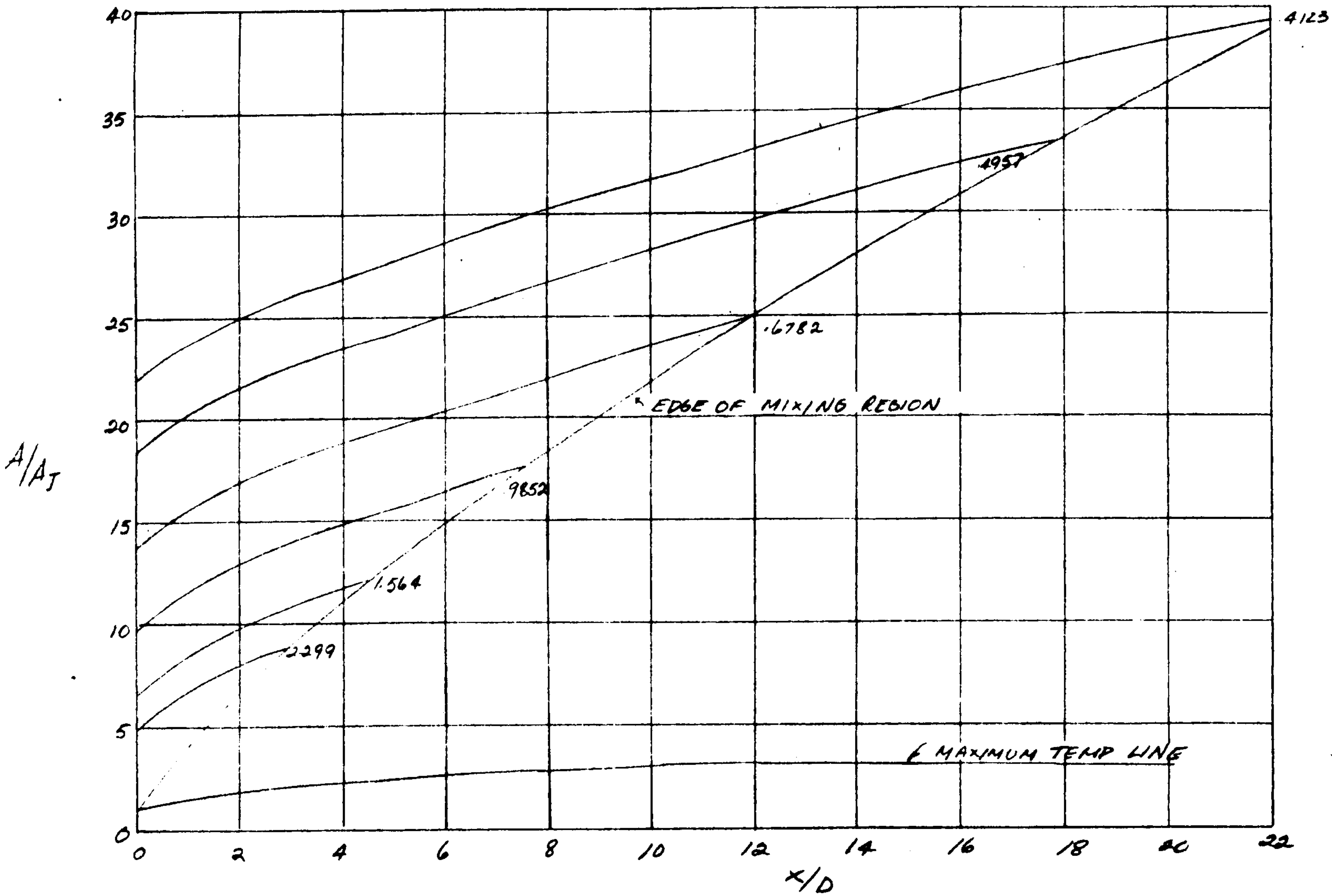

FIG. 11b' RADIAL PROFILES OF VELOCITY, TEMPERATURE, AND SOUND SPEED AT X/D=10.

AXISYMMETRIC, CONSTANT PRESSURE

$M_\infty = 8.$, $M_e = 3.26$, ALTITUDE = 100000 FEET

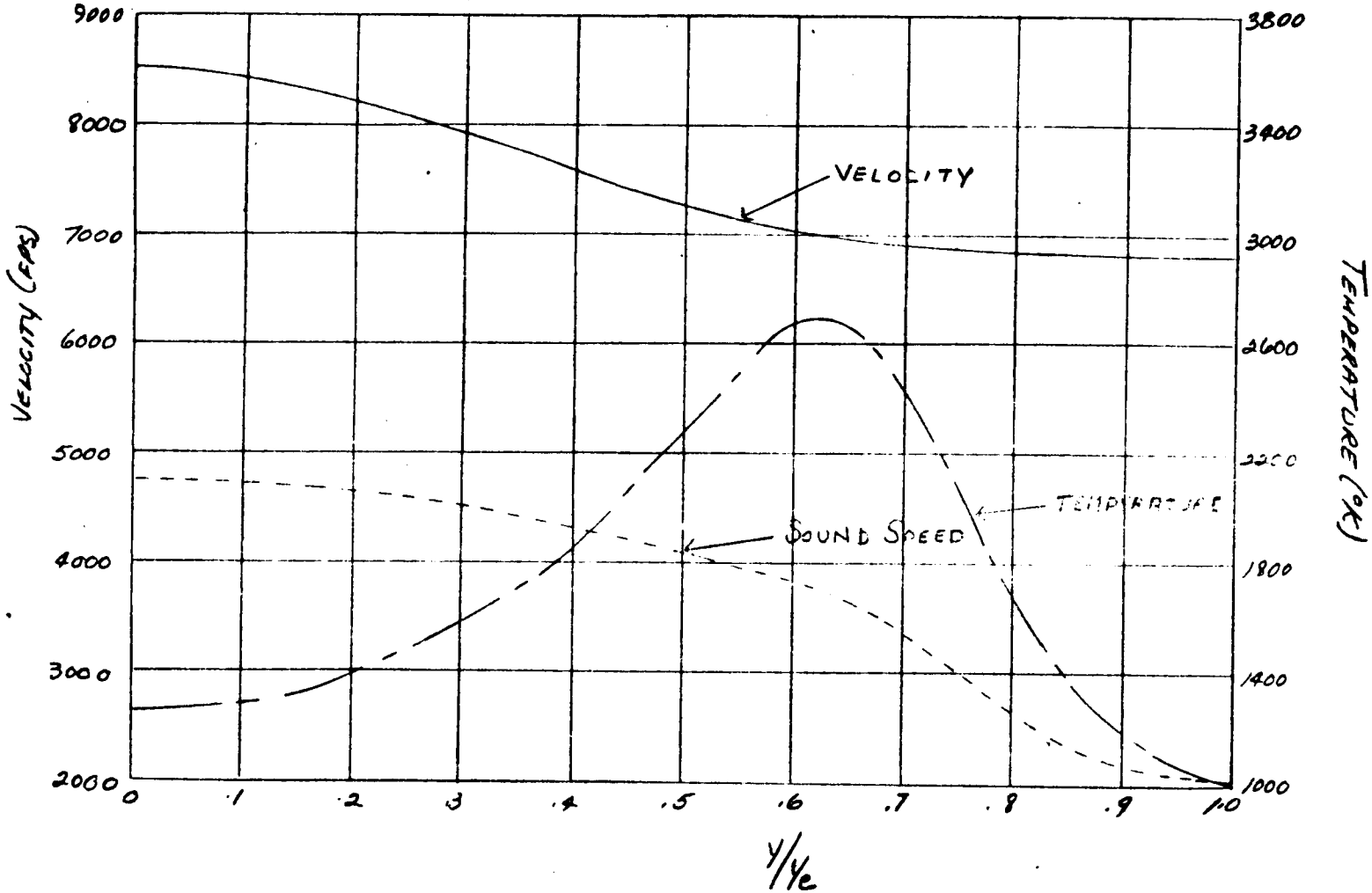

FIG. 11h" RADIAL PROFILES OF VELOCITY, TEMPERATURE, AND SOUND SPEED AT x/D=20.

AXISYMMETRIC, CONSTANT PRESSURE

$M_\infty = 8$, $M_b = 2.36$, ALTITUDE = 100000 FEET

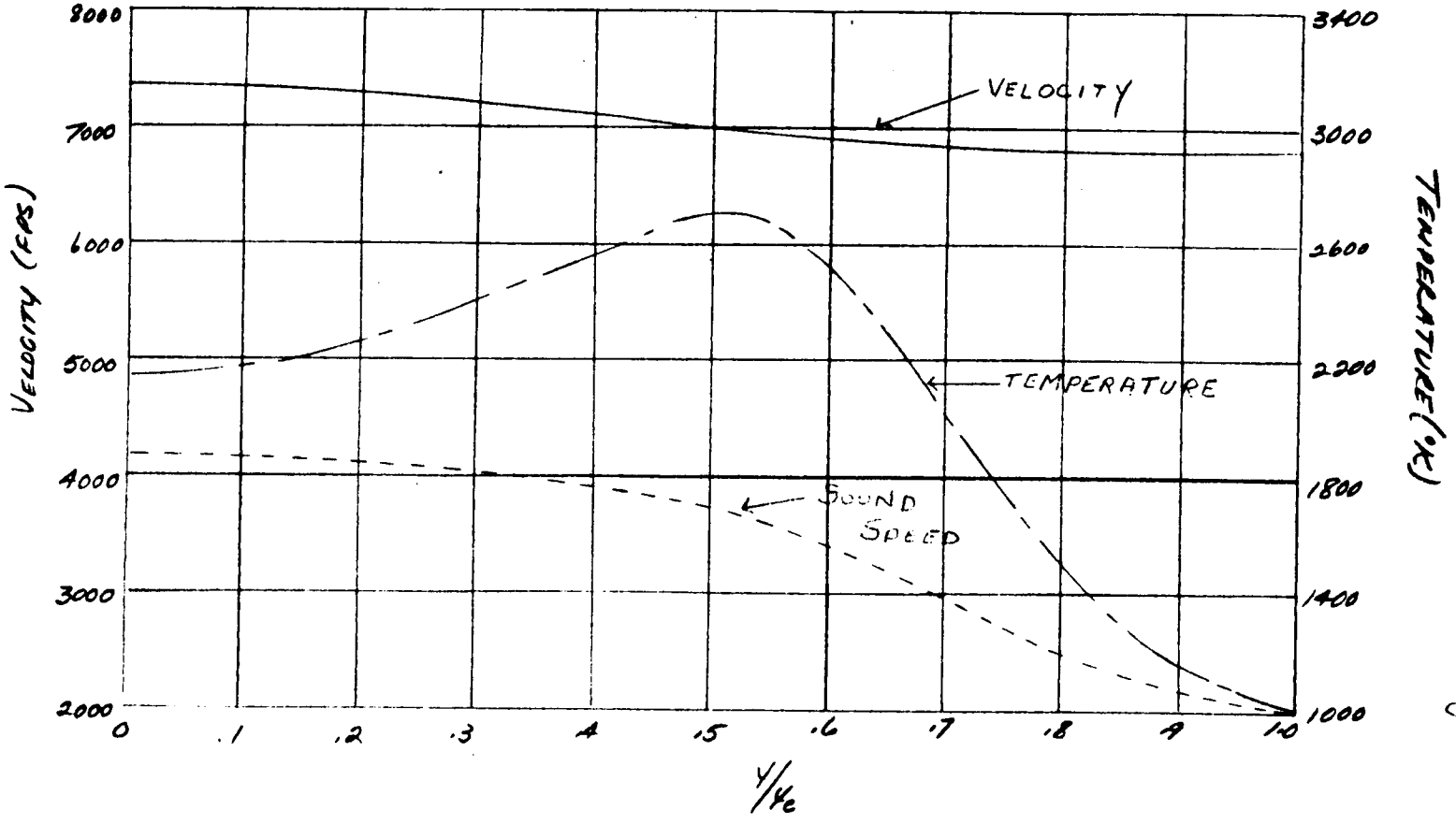

TR 569
Page 65

Fig 11i MIXING AND COMBUSTION REGION

AXISYMMETRIC, CONSTANT PRESSURE

$M_0 = .8$, $M_B = 3.26$, ALTITUDE = 120,000 FEET

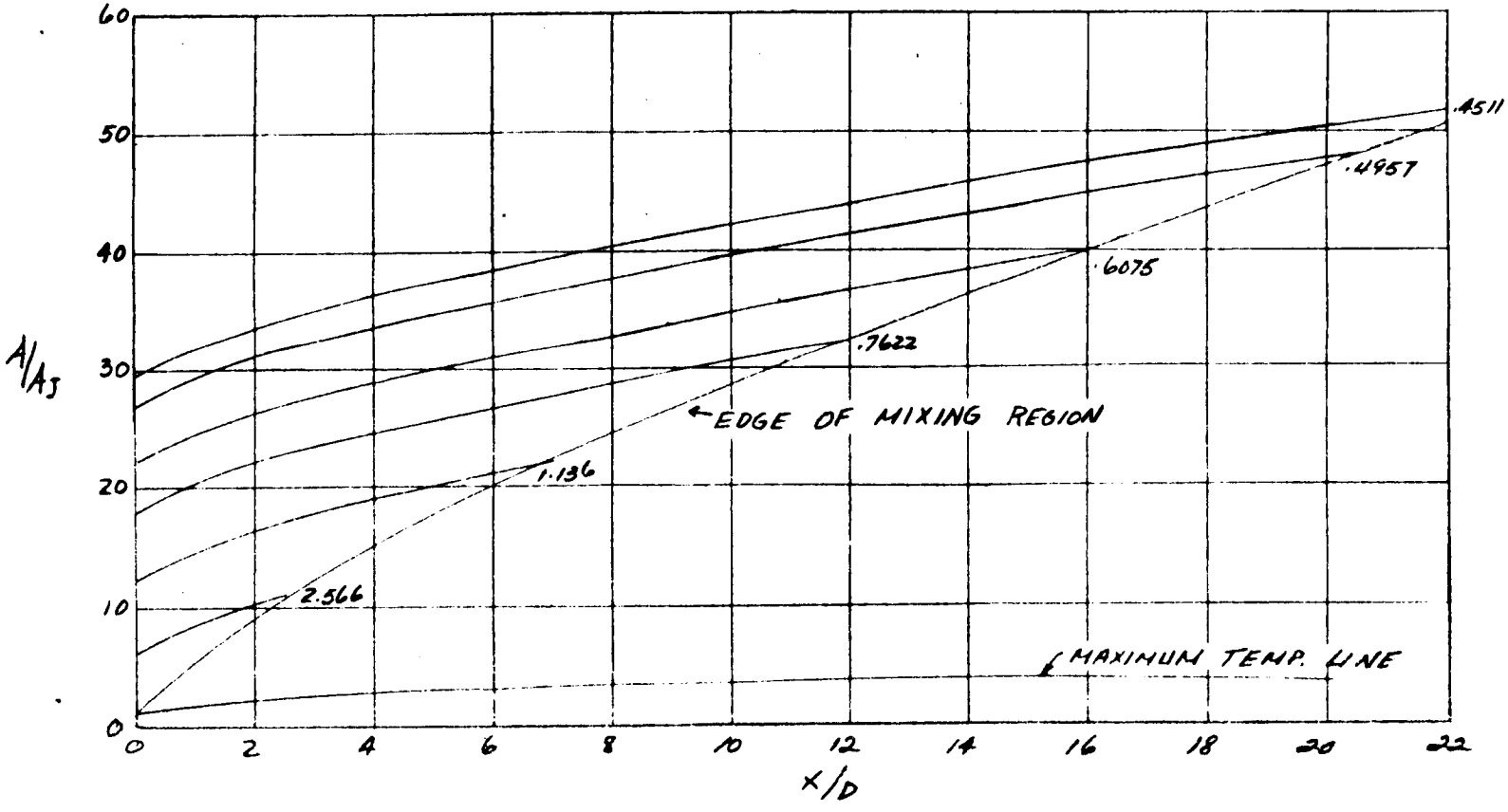

FIG. 11i' RADIAL PROFILES OF VELOCITY, TEMPERATURE, AND SOUND SPEED AT $x/D = 10$.
AXISYMMETRIC, CONSTANT PRESSURE
$M_\infty = 8.$, $M_B = 3.26$, ALTITUDE = 120,000 FEET

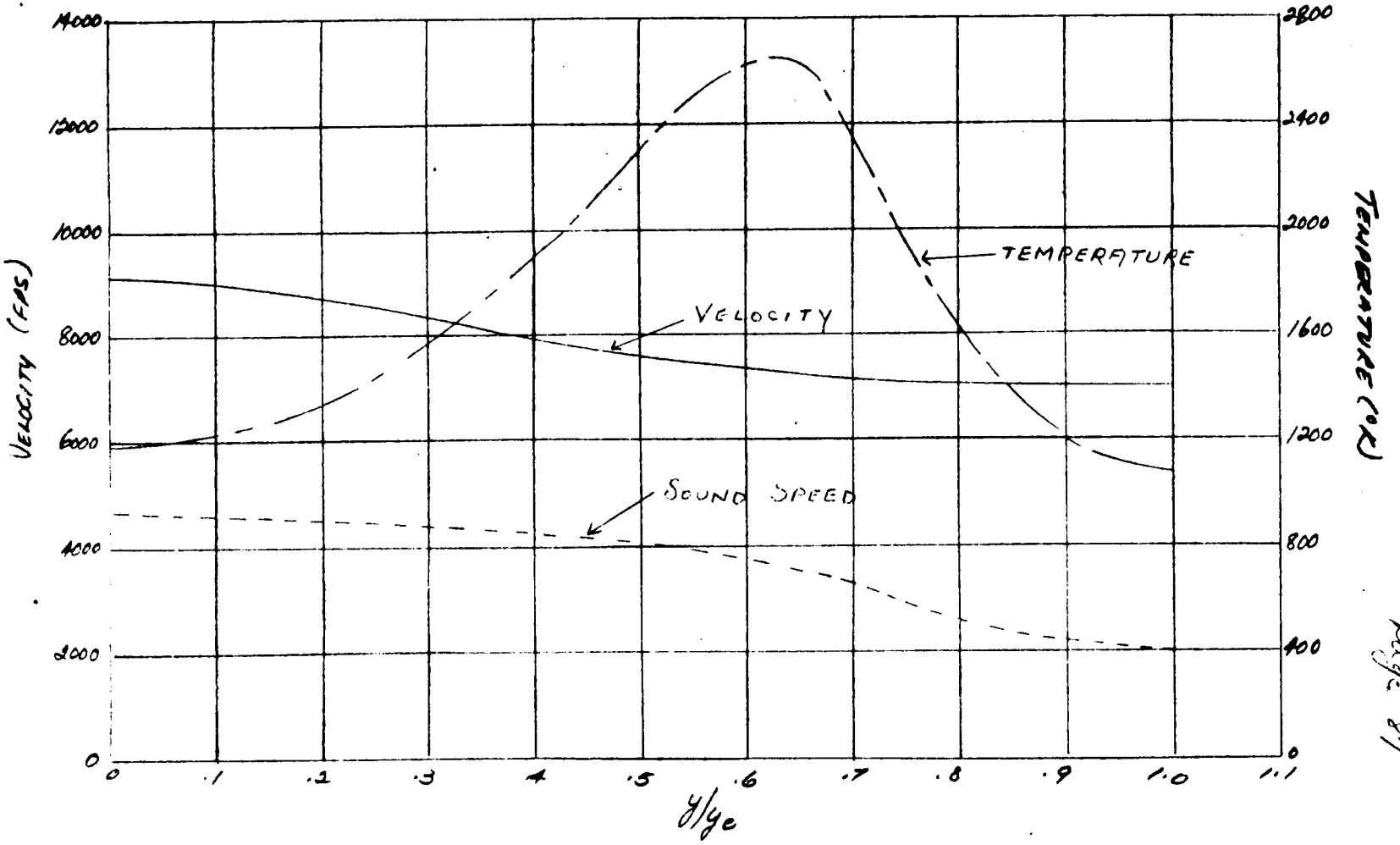

TR 564
Page 87

FIG. 11i" RADIAL PROFILES OF VELOCITY, TEMPERATURE, AND SOUND SPEED AT X/D = 20.
AXISYMMETRIC, CONSTANT PRESSURE
$M_0 = 8.$, $M_B = 3.26$, ALTITUDE = 120,000 FEET

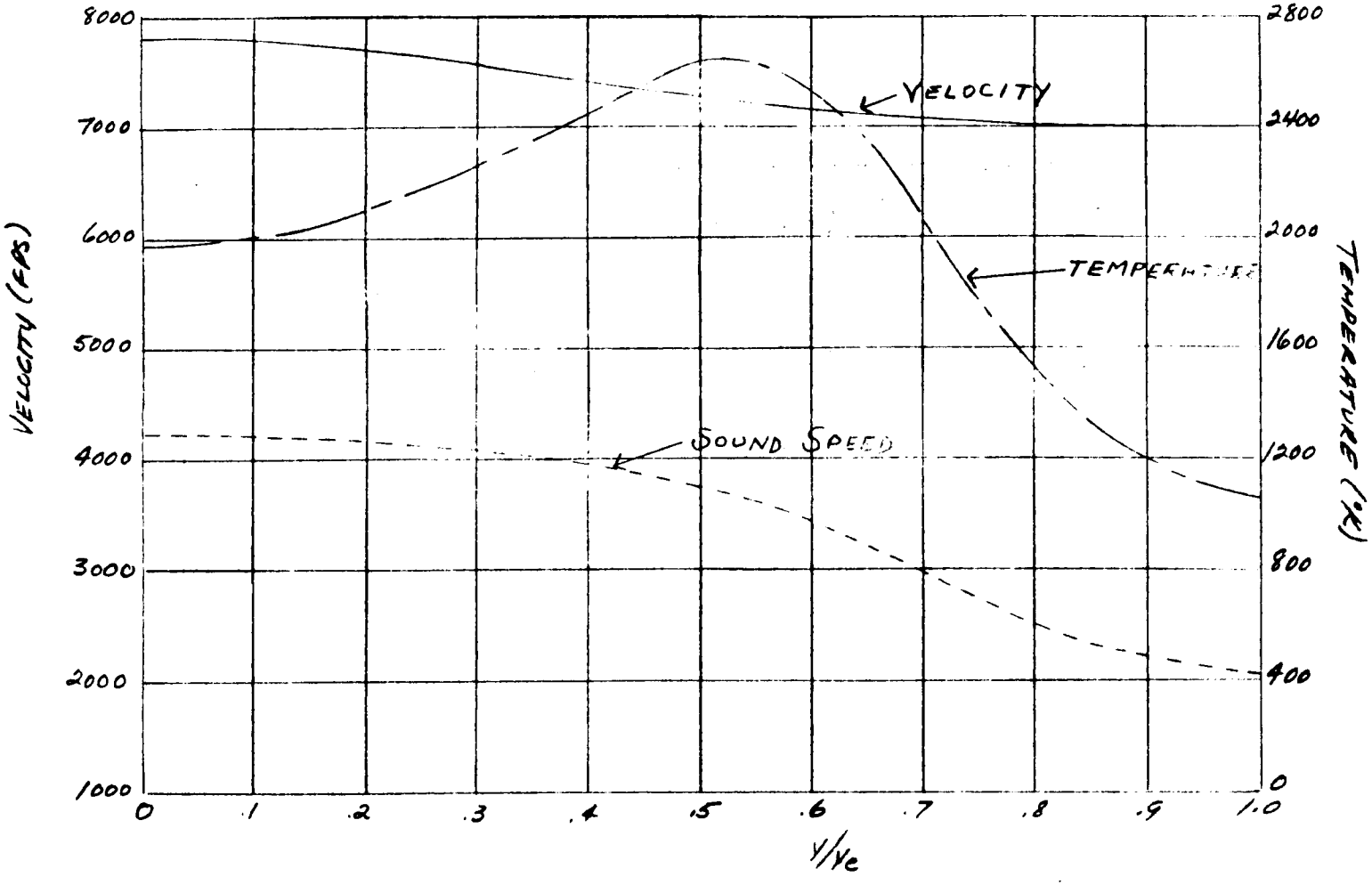

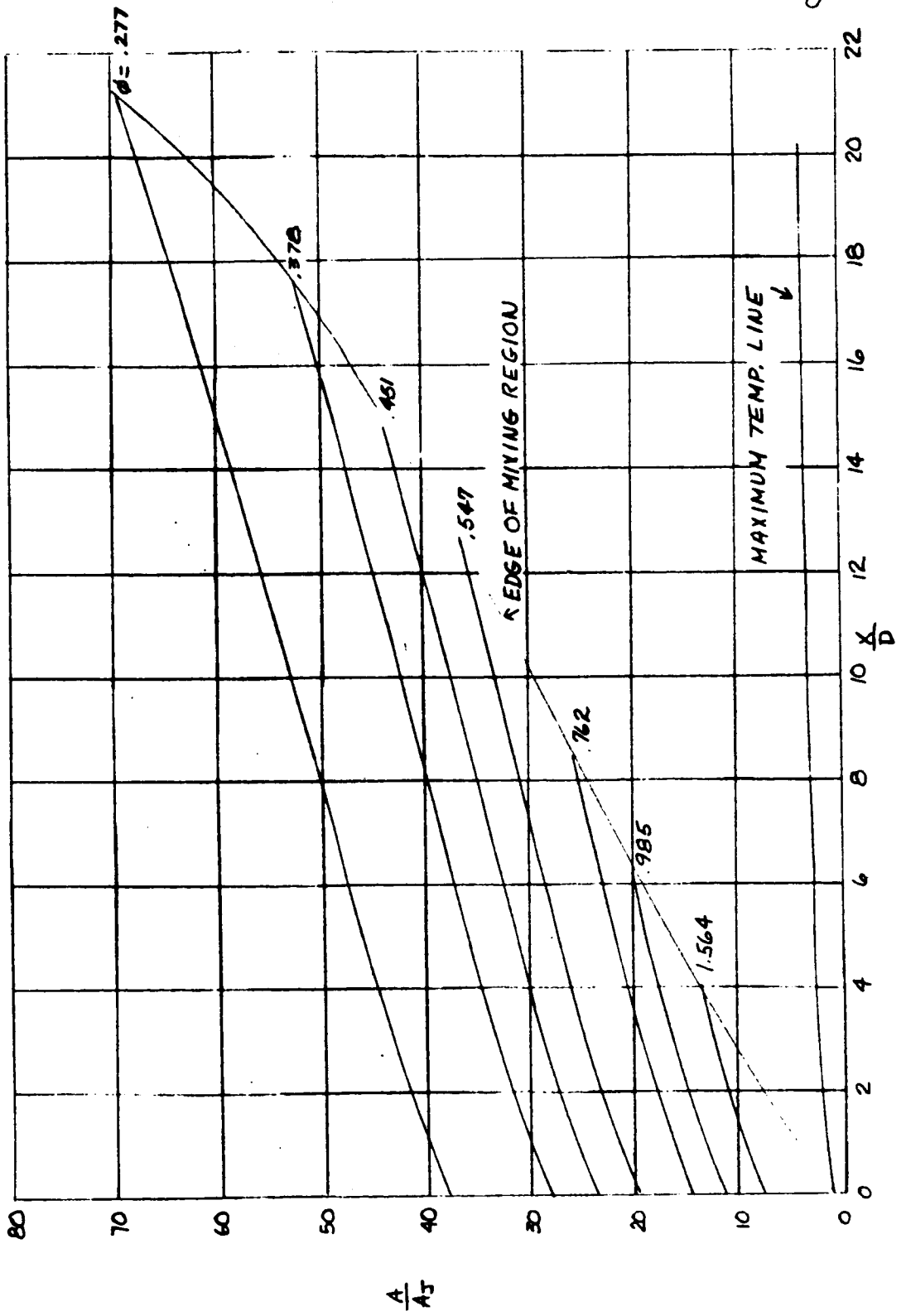

FIG. 113 MIXING AND COMBUSTION REGION
AXISYMMETRIC, PRESSURE DROP, $P/P_0 = 1 - 0.0125 \frac{x}{D}$
$M_\infty = 6$ $M_s = 2$, ALTITUDE = 90,000 FEET

FIG 113 RADIAL PROFILES OF VELOCITY, TEMPERATURE, AND SOUND SPEED AT X/D = 10.
AXISYMMETRIC, PRESSURE DROP
$M_\infty = 6.$, $M_s = 2.$, ALTITUDE = 90,000 FEET

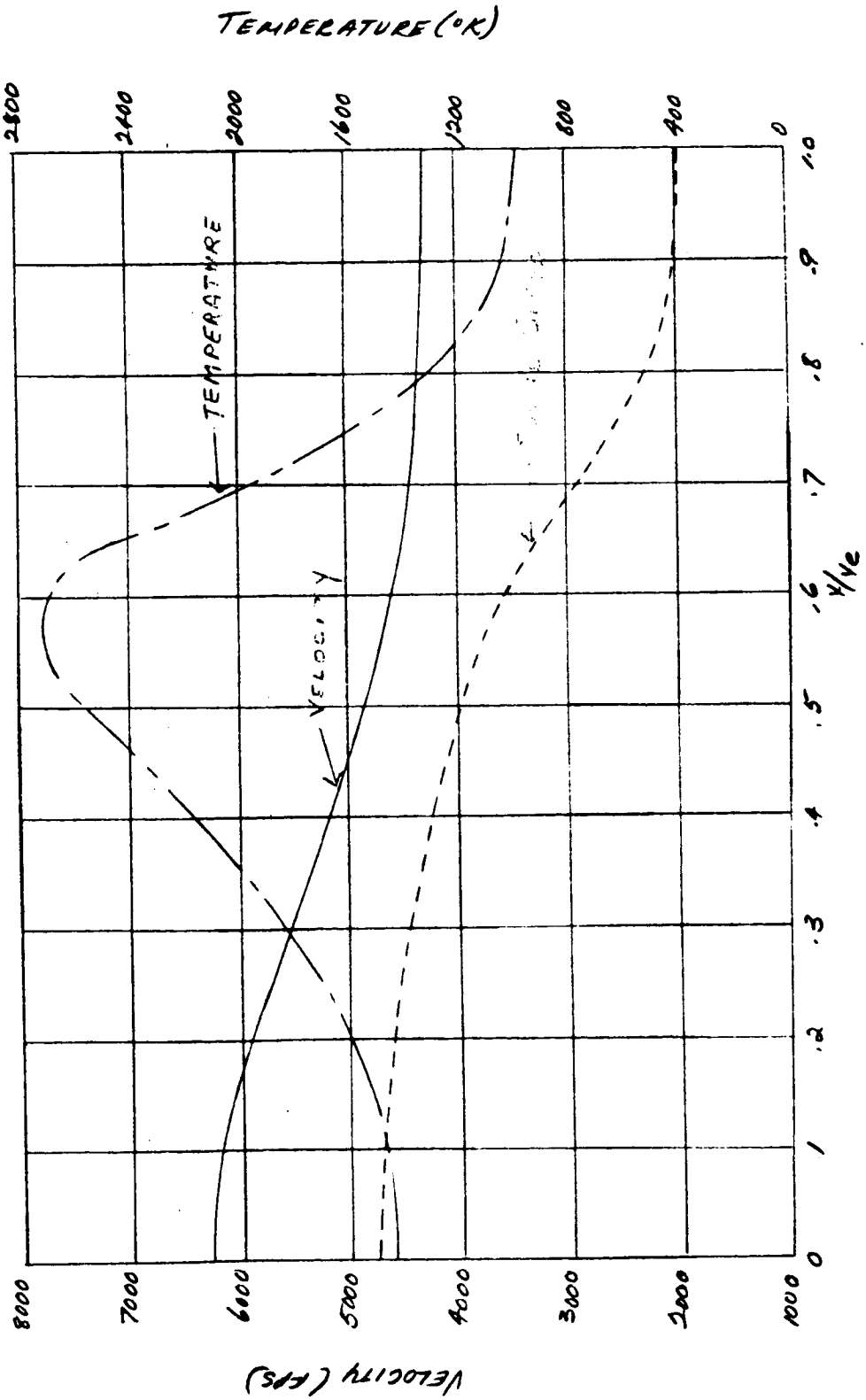

FIG. 11J" RADIAL PROFILES OF VELOCITY, TEMPERATURE, AND SOUND SPEED AT x/D = 20.

AXISYMMETRIC, PRESSURE DROP

$M_\infty = 6$, $M_B = 2.$, ALTITUDE = 90,000 FEET

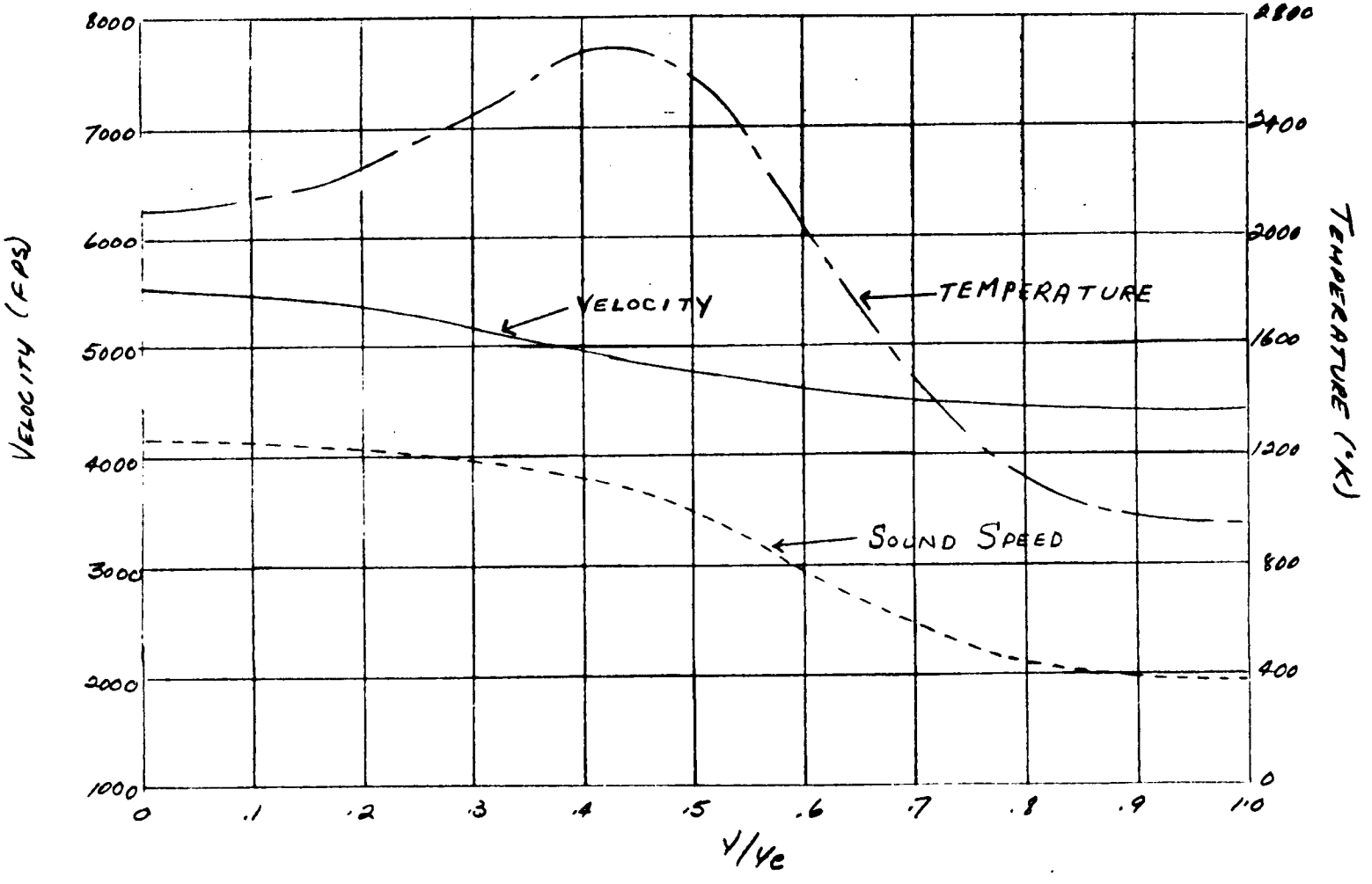

TR 569
Page 91

FIG 11 K MIXING AND COMBUSTION REGION

AXISYMMETRIC, PRESSURE RISE, $\frac{P}{P_b} = 1 + 0.1 \frac{x}{D}$

$M_\infty = 6.$, $M_B = 2.$, ALTITUDE = 90,000 FEET

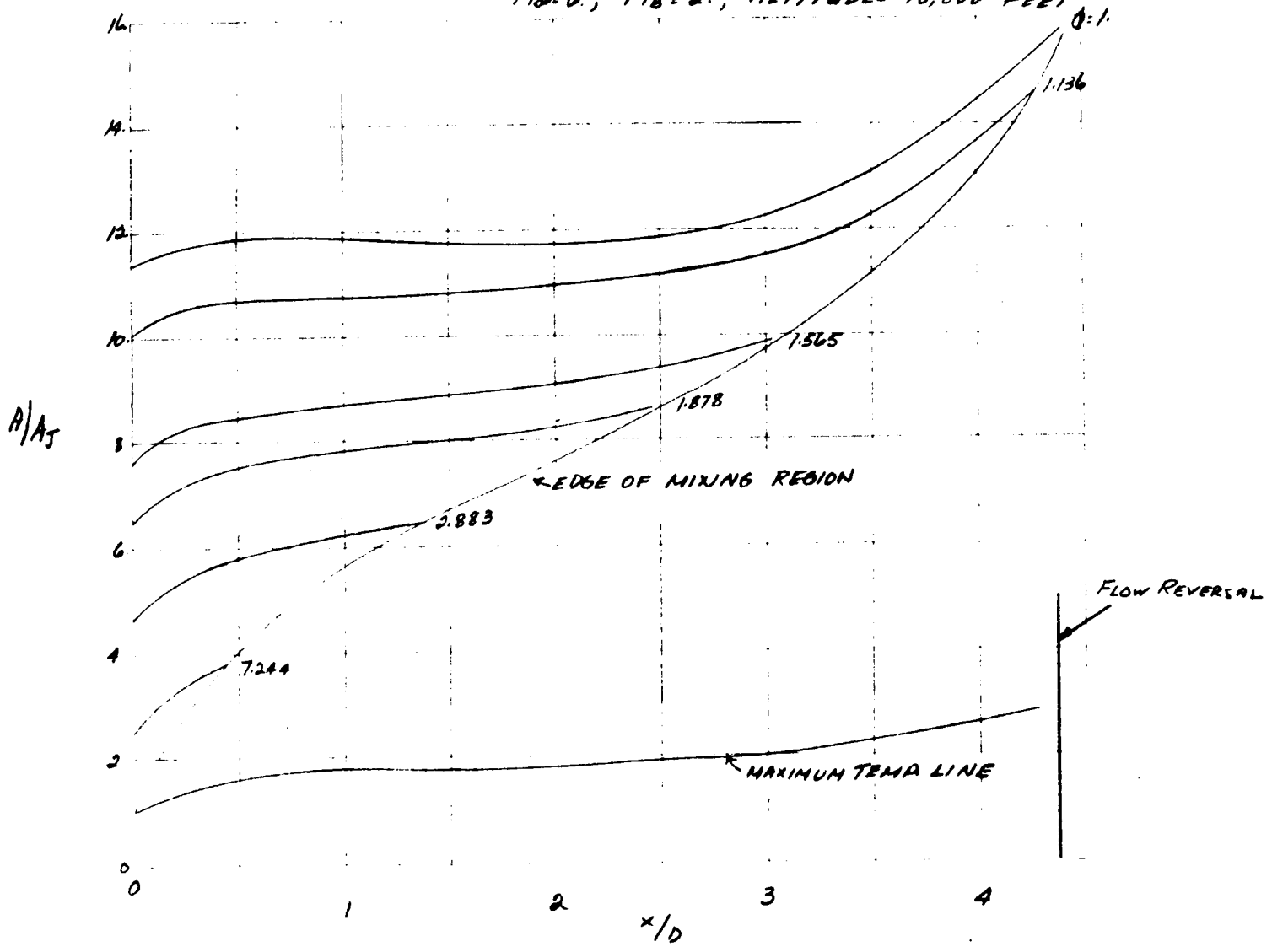

FIG 11K' RADIAL PROFILES OF VELOCITY, TEMPERATURE, AND SOUND SPEED AT X/D = 10.
AXISYMMETRIC, PRESSURE RISE
$M_\infty = 6.$, $M_B = 2.$, ALTITUDE = 90,000 FEET

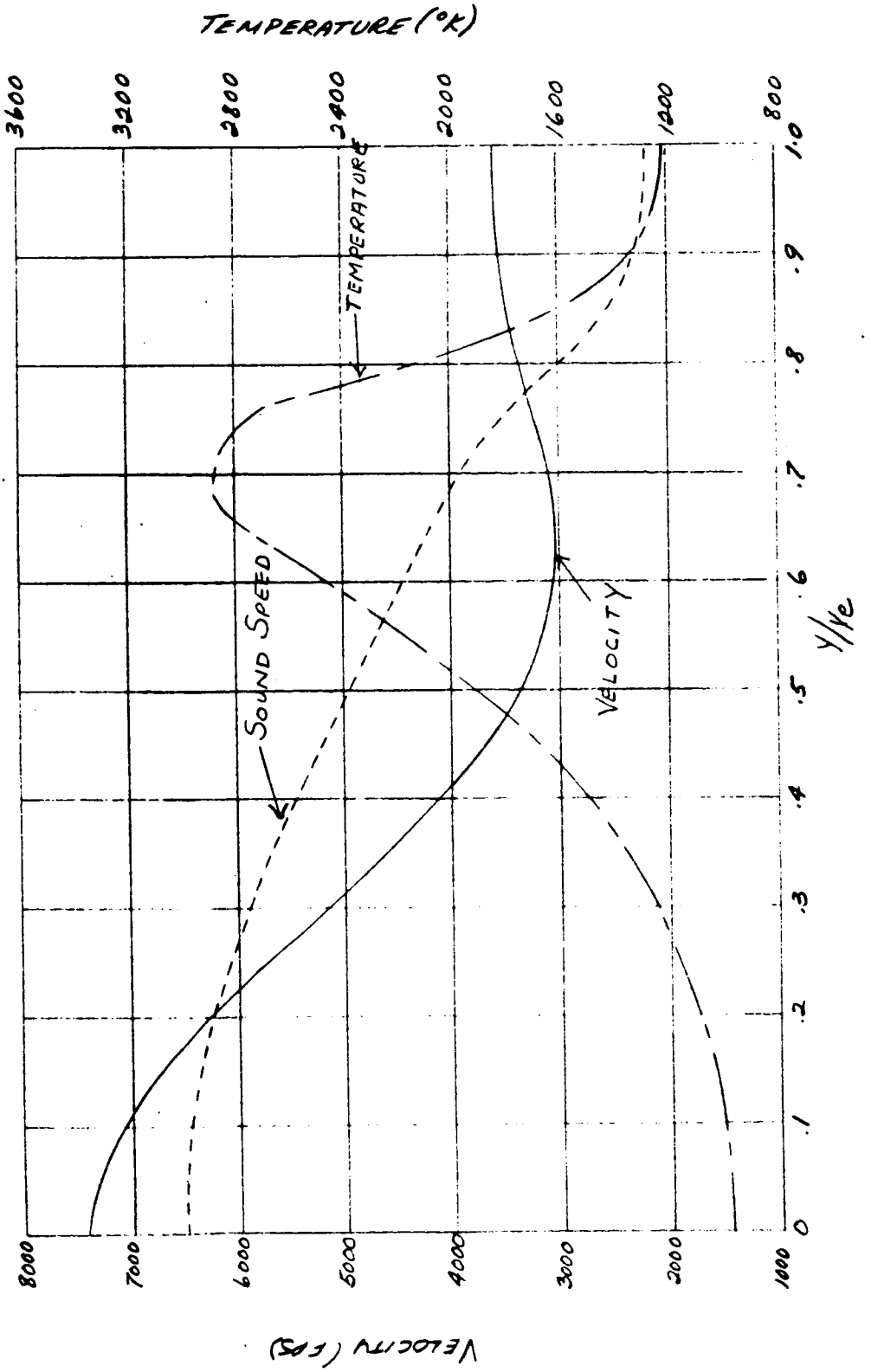

FIG. 11K" RADIAL PROFILES OF VELOCITY, TEMPERATURE, AND SOUND SPEED AT X/D = 17.2
AXISYMMETRIC, PRESSURE RISE
$M_0 = 6.$, $M_B = 2.$, ALTITUDE = 90,000 FEET

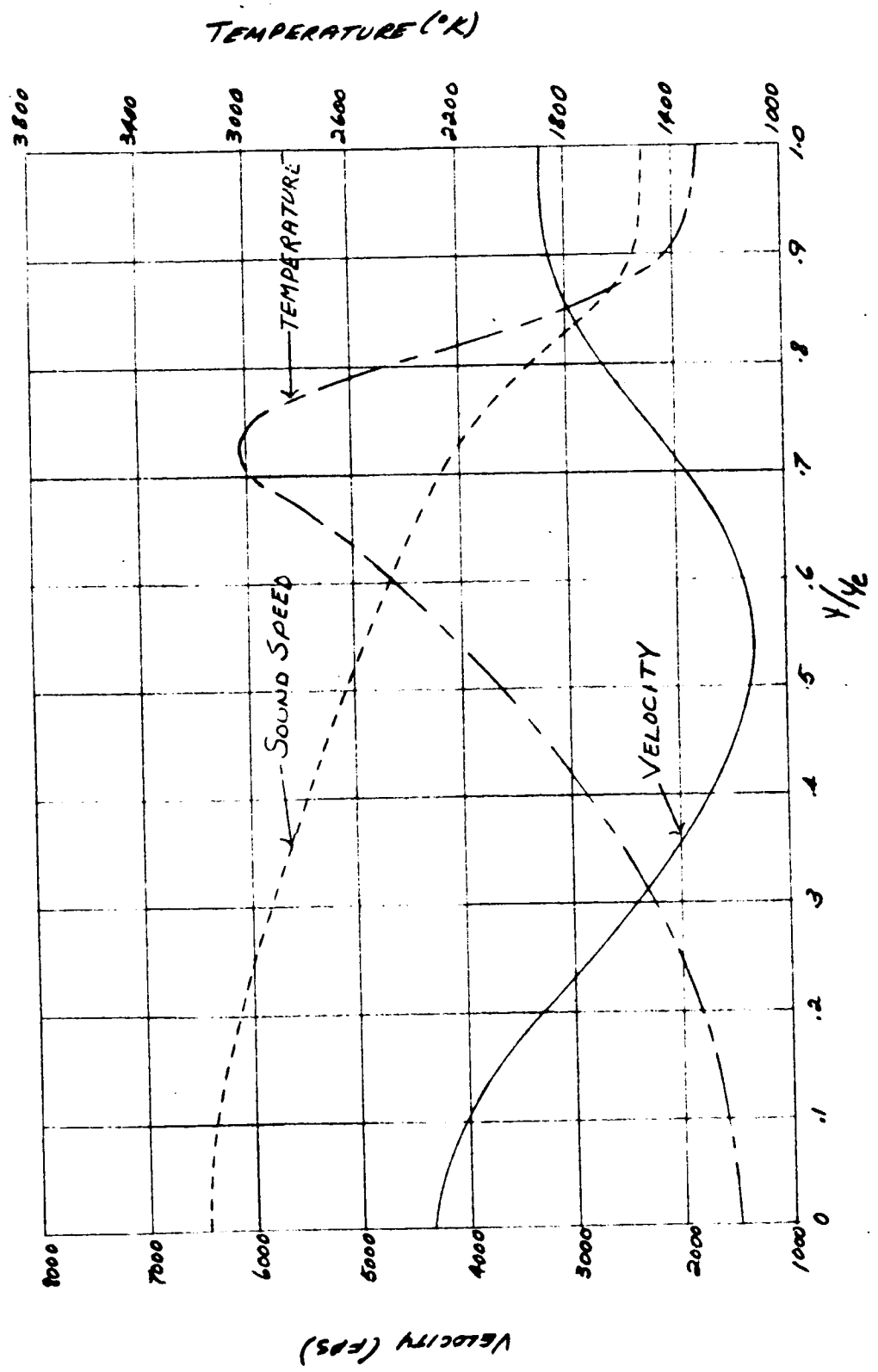

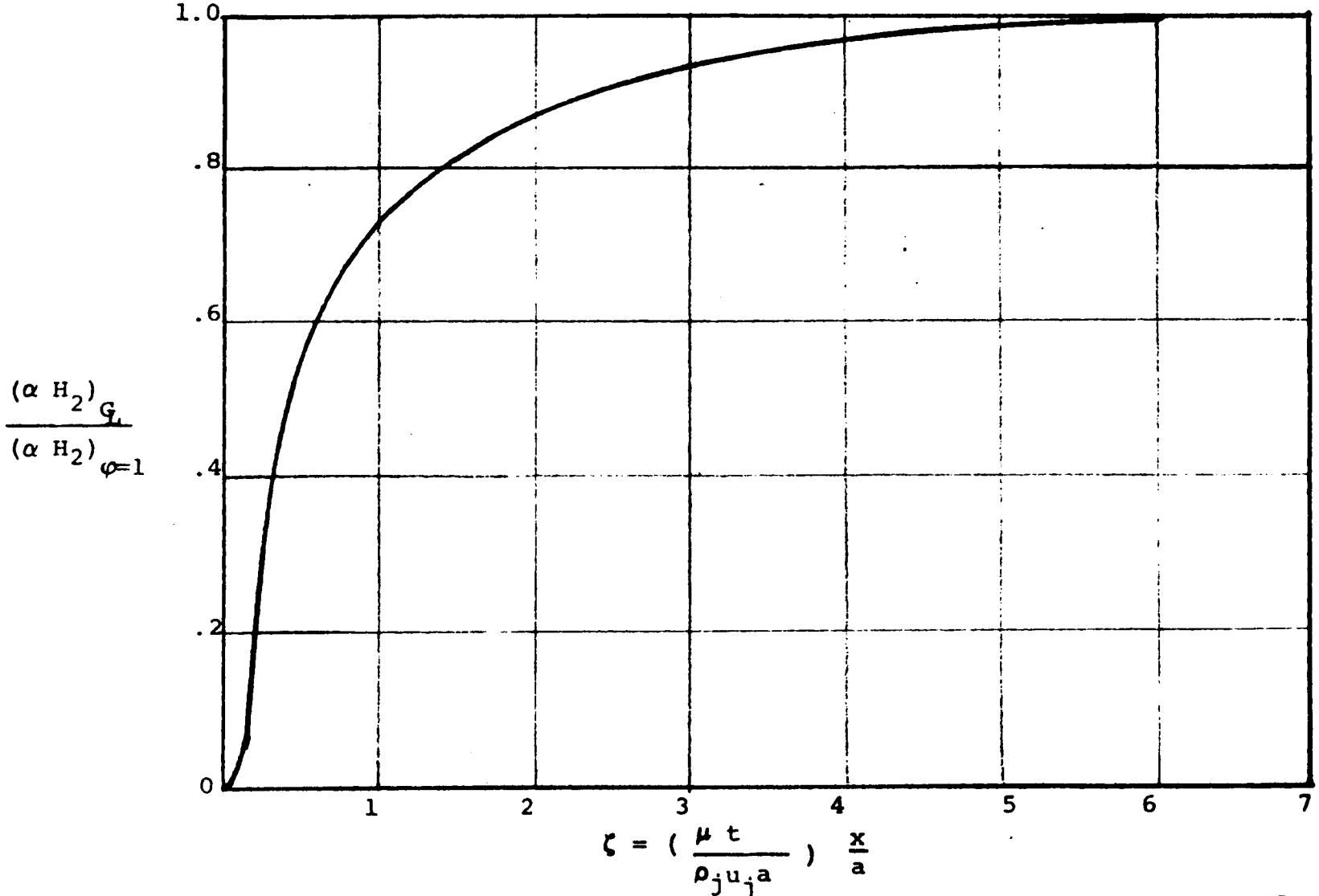

FIGURE 12 - NORMALIZED MASS FRACTION OF WATER AT THE CENTERLINE FOR AXISYMMETRIC

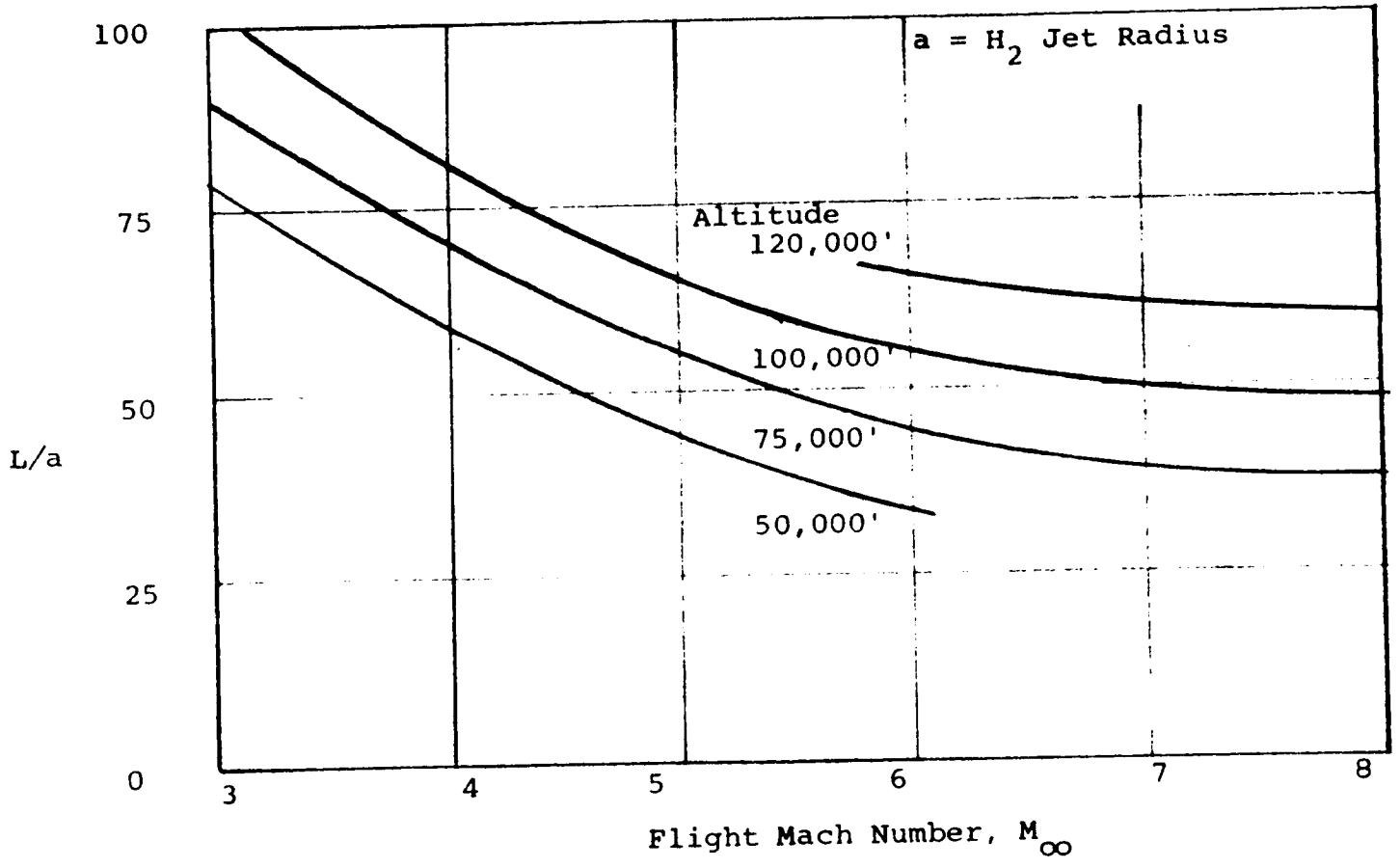

FIGURE 13 - BURNER LENGTH FOR COMPLETE COMBUSTION, AXISYMETRIC HYDROGEN-AIR SYSTEM, CONSTANT PRESSURE

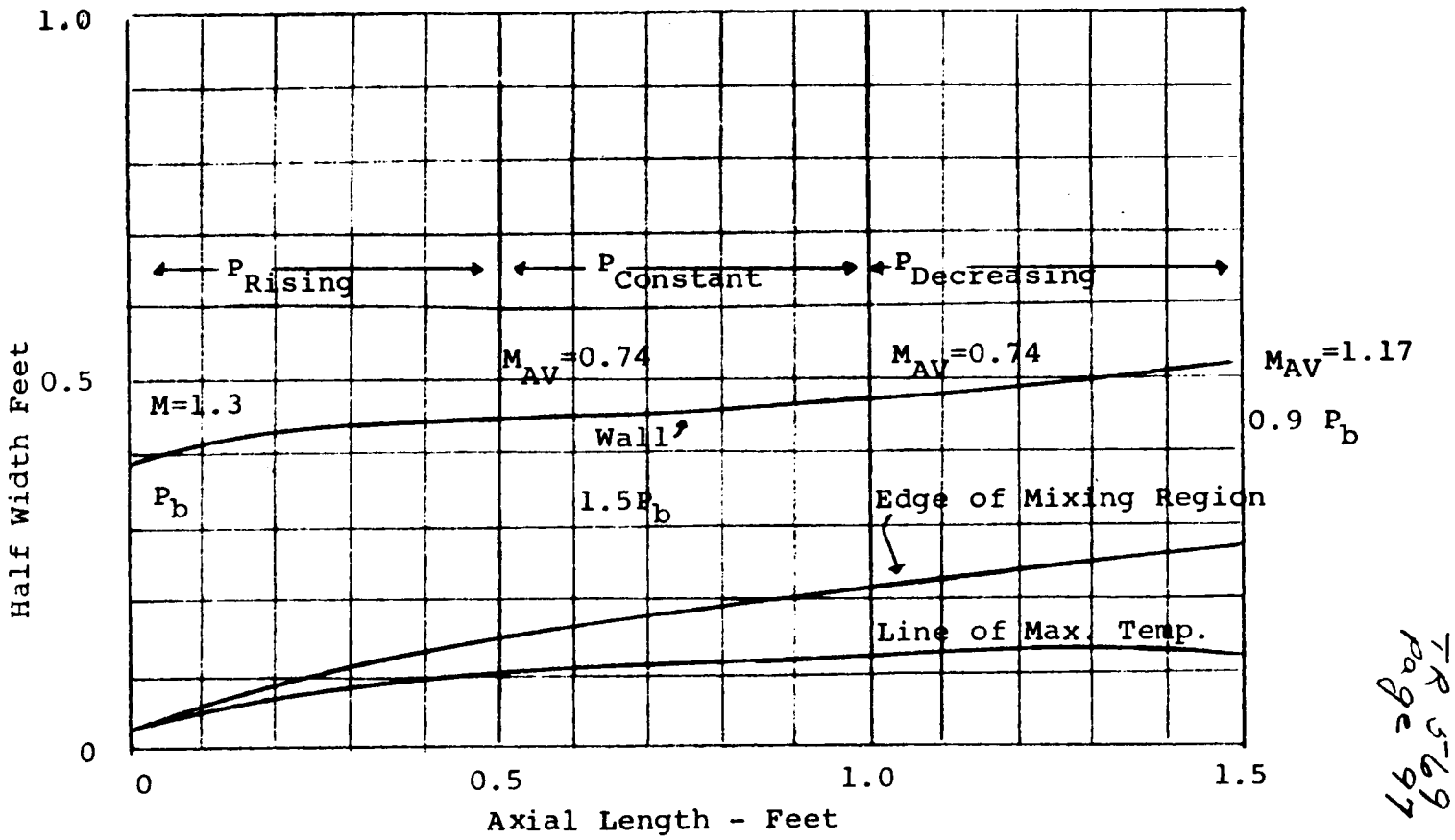

FIGURE 14 - MIXING AND COMBUSTION REGION

TR 5-69
Page 97

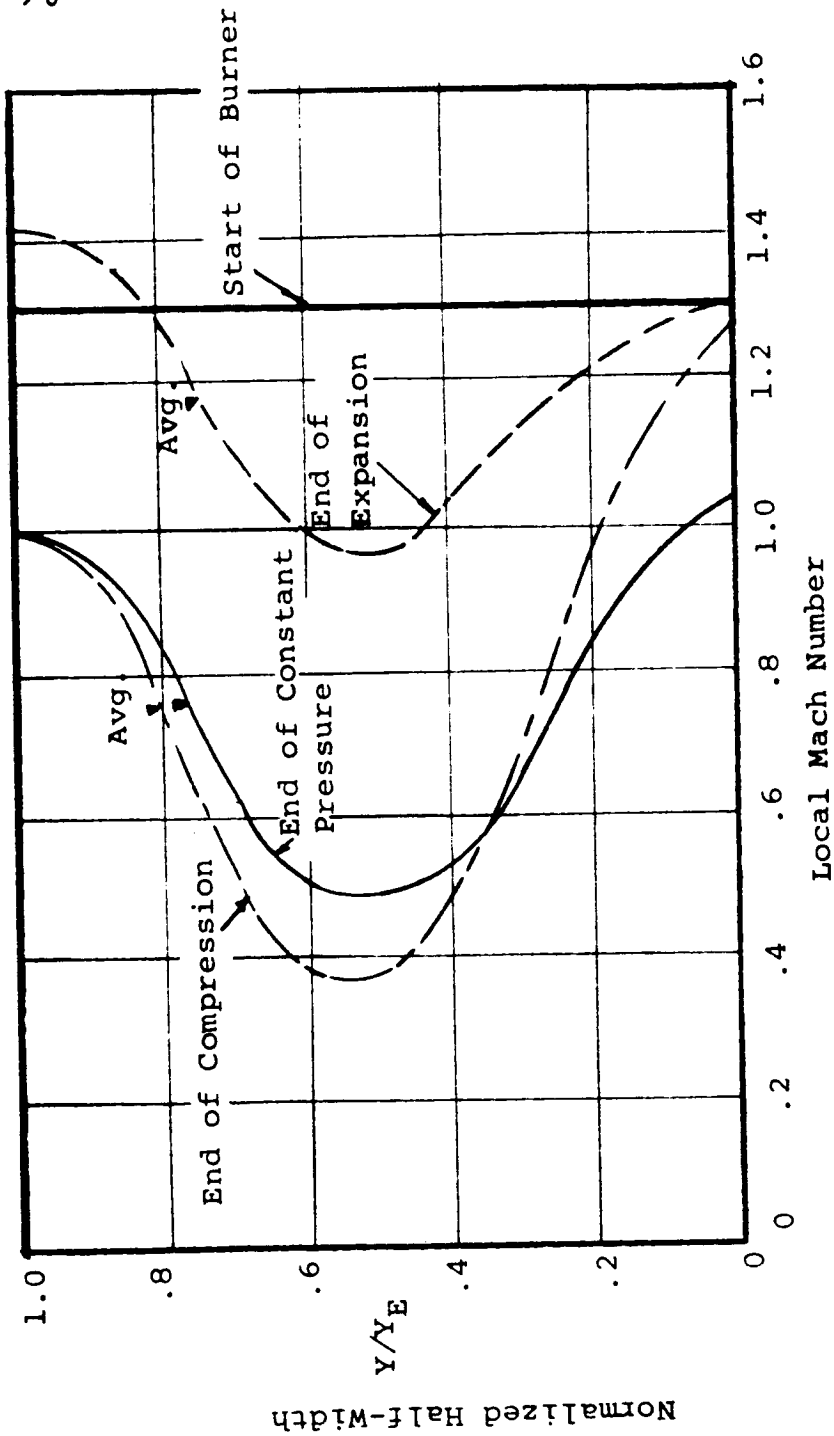

FIGURE 15 - MACH NUMBER PROFILES THROUGH COMBUSTOR

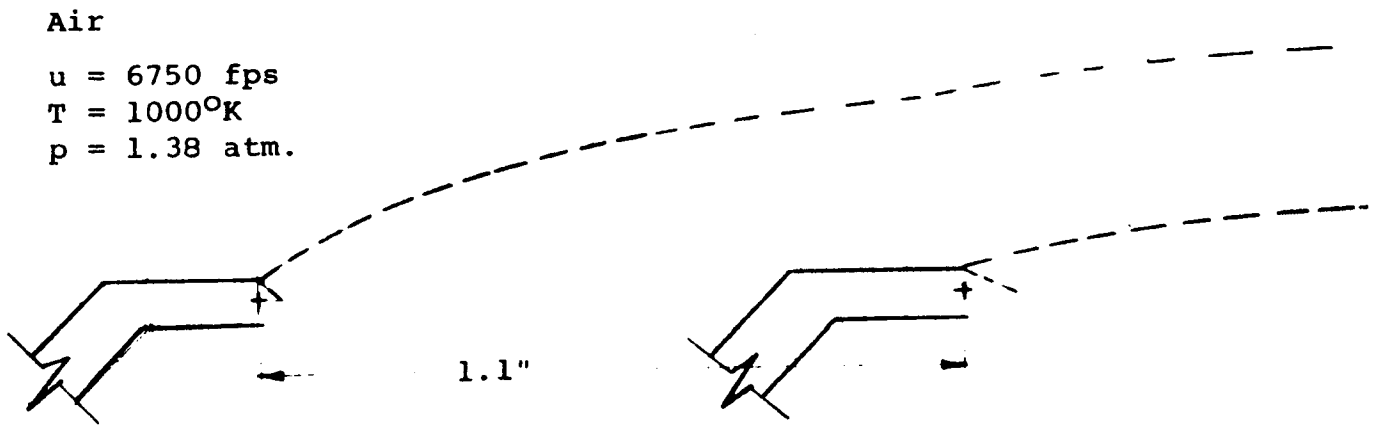

TR 5969
Page 99

FIGURE 16 - SCHEMATIC OF MULTIPLE INJECTION SYSTEM FOR TWO-DIMENSIONAL CONSTANT PRESSURE COMBUSTION

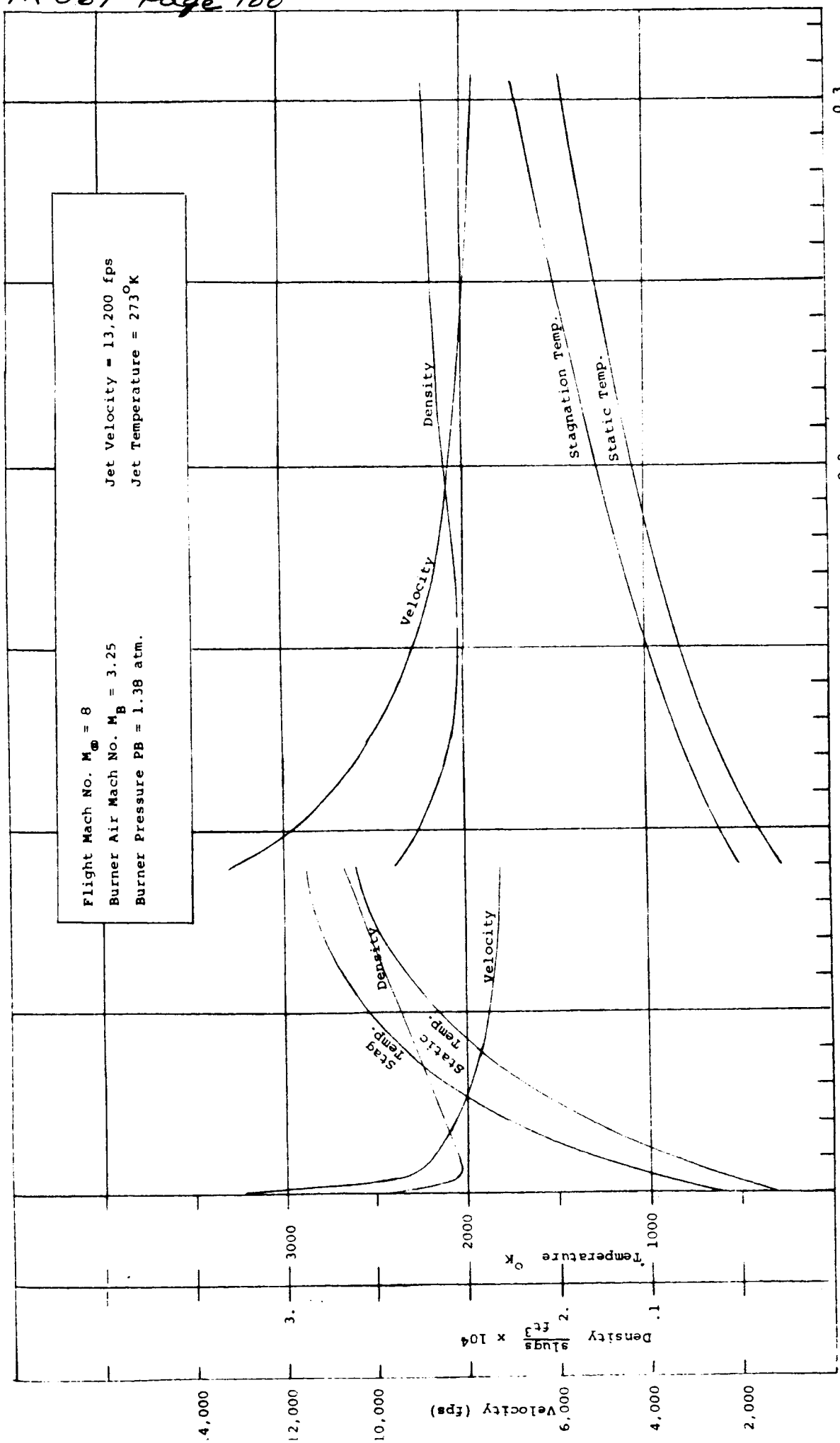

FIGURE 17 - Axial Property Profiles for Two-Dimensional Jet Mixing - Two Slots in Series

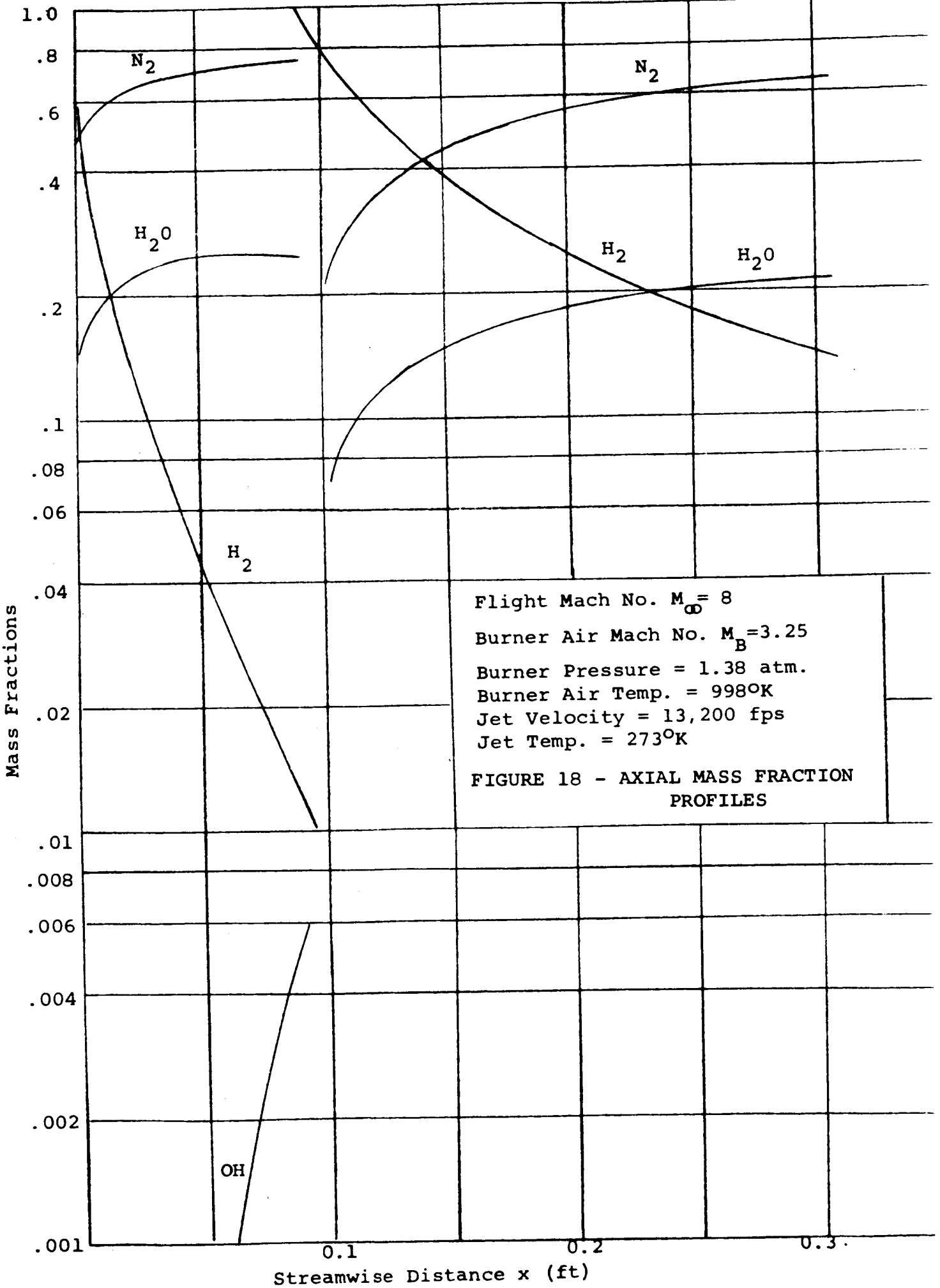

Flight Mach No. $M_\infty = 8$

Burner Air Mach No. $M_B = 3.25$

Burner Pressure = 1.38 atm.

Burner Air Temp. = 998°K

Jet Velocity = 13,200 fps

Jet Temp. = 273°K

FIGURE 18 - AXIAL MASS FRACTION PROFILES

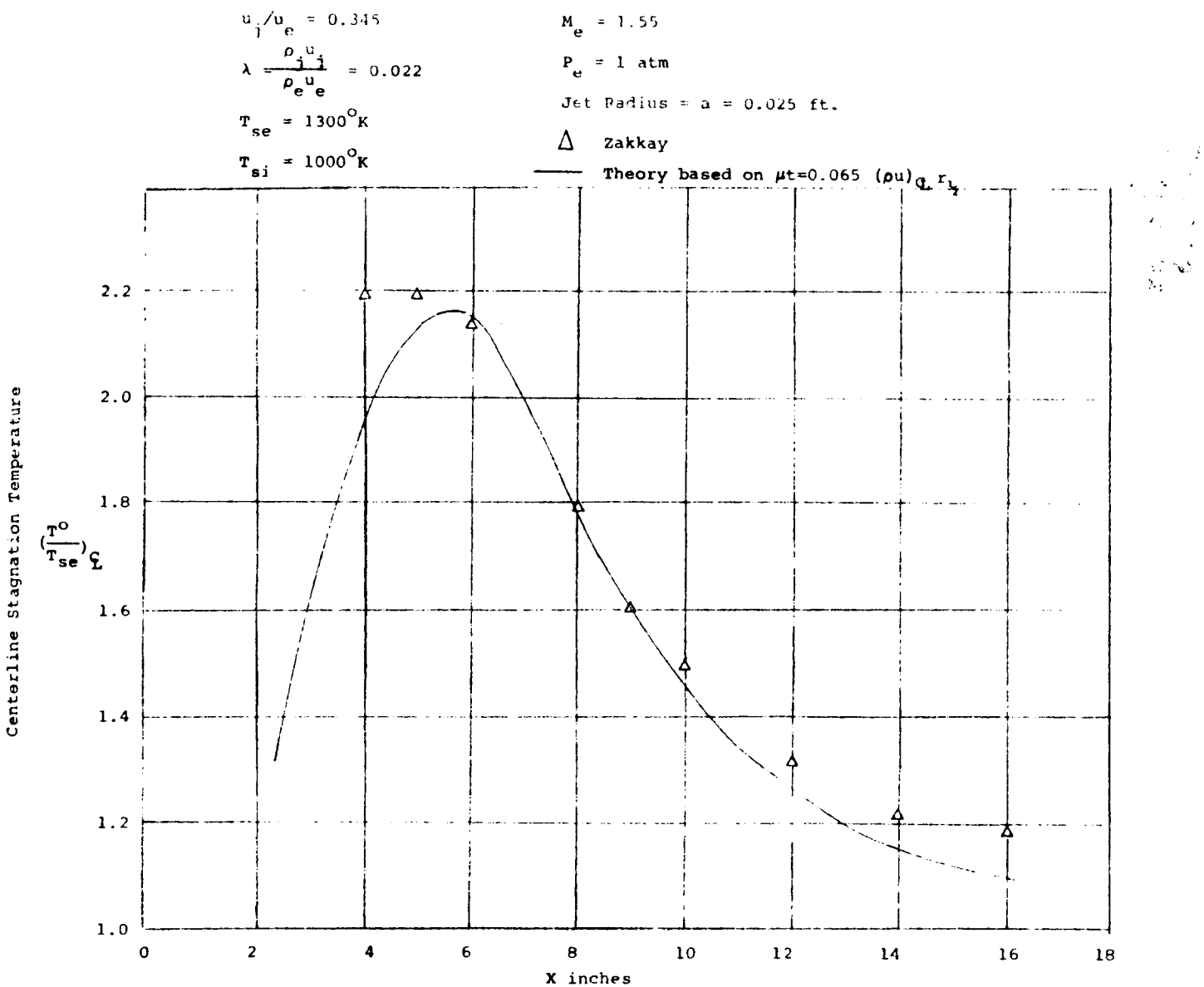

FIGURE 19 - AXISYMMETRIC, ZAKKAY EXPERIMENT #1

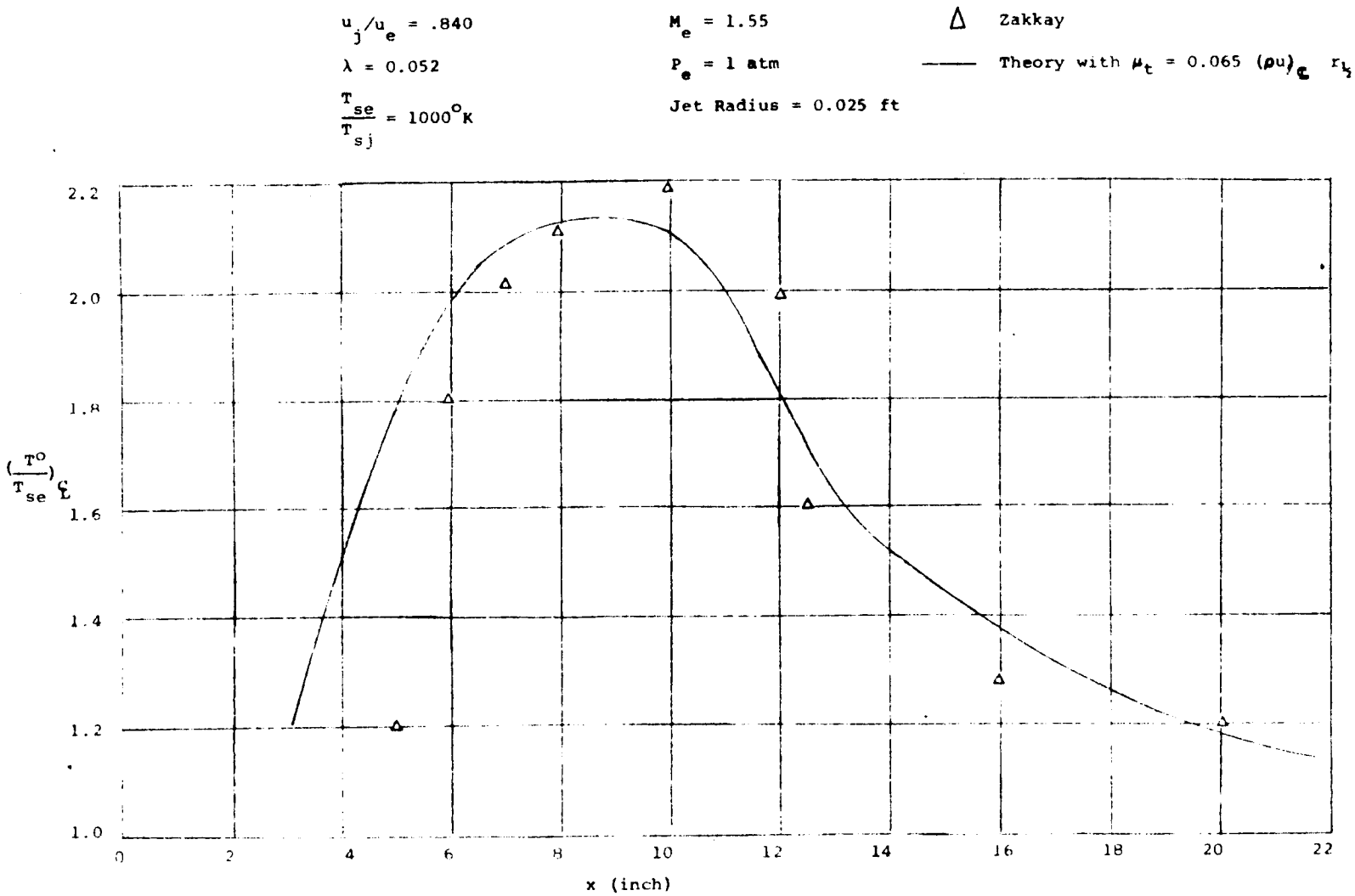

FIGURE 20 - AXISYMMETRIC ZAKKAY EXPERIMENT #2

TP 5716
Page 103

$u_j/u_e = .850$

$\lambda = \frac{\rho_j u_j}{\rho_e u_e} = .06$

$T_{se} = 1460^{\circ}K$

$T_{sj} = 1000^{\circ}K$

$M_e = 1.55$

$P_e = 1$ atm.

Jet Radius = a = 0.025ft

Δ Zakkay and Krause "Mixing Problems With Chemical Reactions" Preprinted from Supersonic Flow, Chemical Processes and Radiative Transfer - Pergamon Press, 1964

—— Theory based on $\mu_t = 0.065 (\rho u)_{\ell} r_j$

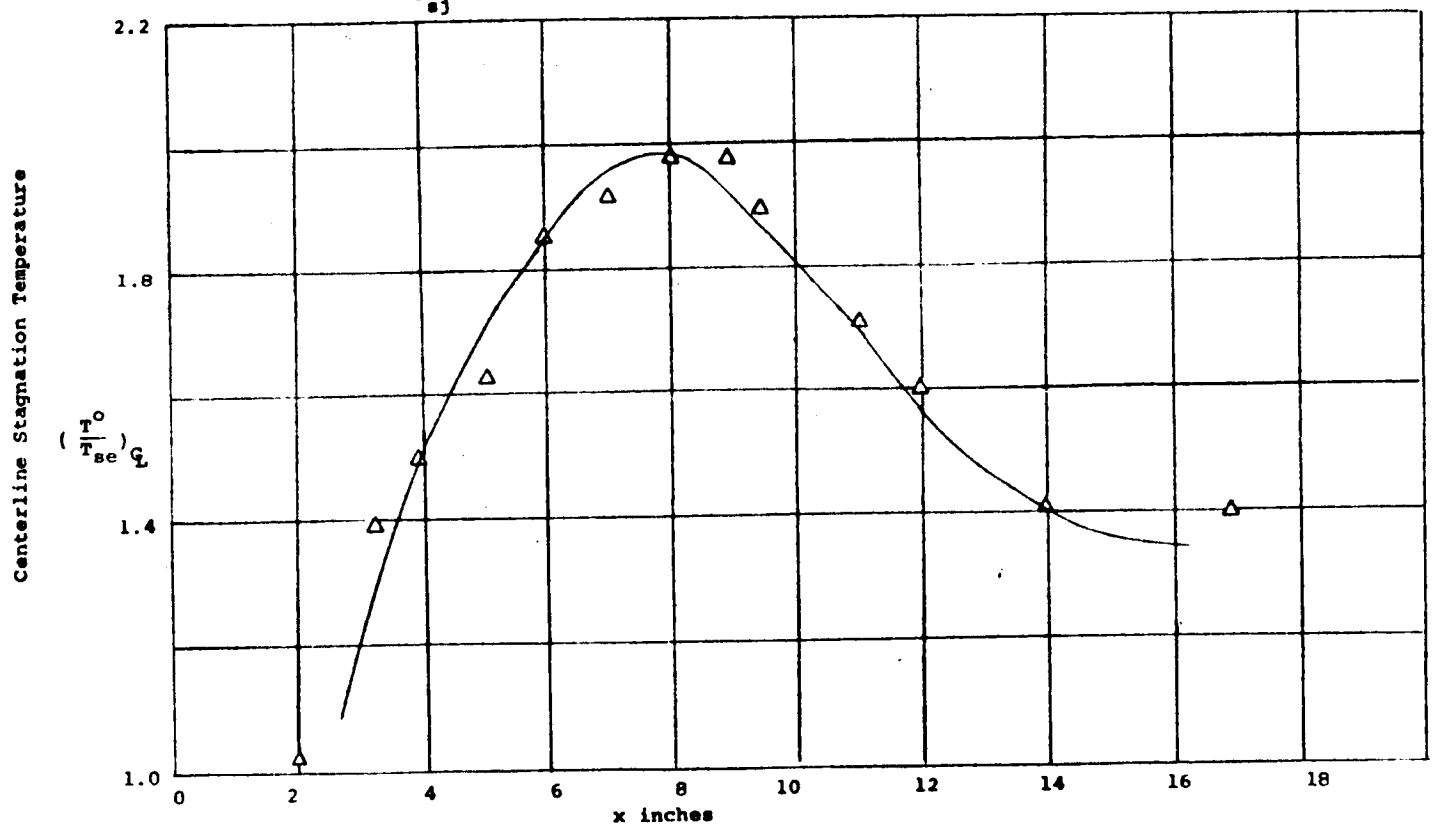

FIGURE 21 - ZAKKAY EXPERIMENT #3

TR 569
Page 104